COMPUTATIONAL MODELING AND EXPERIMENTAL VALIDATION OF SINGLE PHASE AND BOILING FLOWS IN MICROGAP COOLING LAYERS

A Dissertation
Presented to
The Academic Faculty

by

Daniel Lorenzini

In Partial Fulfillment
of the Requirements for the Degree
Doctor of Philosophy in the
George W. Woodruff School of Mechanical Engineering

Georgia Institute of Technology
May 2019

COMPUTATIONAL MODELING AND EXPERIMENTAL VALIDATION OF SINGLE PHASE AND BOILING FLOWS IN MICROGAP COOLING LAYERS

Approved by:

Dr. Yogendra Joshi, Advisor
School of Mechanical Engineering
Georgia Institute of Technology

Dr. Muhannad Bakir
School of Electrical and Computer Engineering
Georgia Institute of Technology

Dr. Mostafa Ghiaasiaan
School of Mechanical Engineering
Georgia Institute of Technology

Dr. Satish Kumar
School of Mechanical Engineering
Georgia Institute of Technology

Dr. Suresh Sitaraman
School of Mechanical Engineering
Georgia Institute of Technology

Date Approved:[December 11, 2018]

ACKNOWLEDGEMENTS

The completion of this journey has been possible due to the fortunate interaction with many individuals. So many experiences, challenges, decisions and life-changing events led me to reinvent myself over these last 4 years; I am content with the outcome and I feel lucky for multiple reasons.

First, I would like to thank my advisor, Professor Yogendra Joshi, for giving me the opportunity to join his research group and for all of the countless help and support I got through my doctoral studies. I certainly could not have asked for a better mentor and thanks to his trust on my projects and ideas, empowered by his vast experience and vision, today I am excited about the future.

I am also grateful to the Mexican government for providing me with a fellowship through the National Council of Science and Technology (CONACYT), as well as for the different awards I had the honor to receive; such investment in my career will not be in vain, I will keep working toward a brighter future in collaboration with Mexico and their talented people.

I wish to thank all of the team at Cooling Tree Systems, where I spent two summers at the expense of not having certainty what would happen with a startup company. I declined other internship opportunities at major companies in the field, and I was also questioned by several individuals if it was worth the risk, but that did not stop the thrill; I can tell you now it was worth every second of my time.

I also would like to thank my thesis committee members, Prof. Mostafa Ghiaasiaan, Prof. Muhannad Bakir, Prof. Suresh Sitaraman, and Prof. Satish Kumar for their valuable time and insightful feedback through my proposal and defense processes; I had the honor of being in their classes or collaborating in research projects that were a key part in my formation.

I would like to acknowledge all of my colleagues at the Microelectronics and Emerging Technologies Thermal Laboratory (METTL) for all of their support through this journey. I wish to thank Pouya Asrar, Jayati Athavale, and Sangbeom Cho for their friendship and the many technical collaborations we had.

My personal gratitude goes to my parents, Jose and Maria, and my outstanding brothers, Pepe and Aldo, for all their continuous love, support, and understanding throughout not just this journey, but also my life.

TABLE OF CONTENTS

LIST OF TABLES

LIST OF FIGURES

LIST OF SYMBOLS AND ABBREVIATIONS

Symbol	*Definition*	*Units*
A	Area	m^2
c, c_p	Specific heat	$J\ kg^{-1}\ K^{-1}$
C	Mesh independence criterion	--
D	Diameter	m
E	Specific energy	$J\ kg^{-1}$
$\vec{F}$	Volumetric surface tension force	$N\ m^{-3}$
$\vec{g}$	Gravitational acceleration	$m\ s^{-2}$
G	Mass flux	$kg\ m^{-2}\ s^{-1}$
h_{lv}	Latent enthalpy of vaporization	$J\ kg^{-1}$
h	Heat transfer coefficient	$W\ m^{-2}\ K^{-1}$
H	Height	m
k	Thermal conductivity	$W\ m^{-1}\ K^{-1}$
L	Length	m
M	Molar mass	$kg\ kmol^{-1}$
$\hat{n}_w$	Wall surface normal vector	--
N	Field variable of comparison	--
P	Pressure	Pa
ΔP	Pressure drop	Pa
q''	Heat flux	$W\ m^{-2}$
R	Curvature radii	m

S	Pitch	m
$S_{l,v}$	Mass source term due to phase change	kg m^{-3} s^{-1}
S_{e}	Energy source term	J m^{-3} s^{-1}
t	Time	s
t_i	Thickness	m
$\hat{t}_{\mathrm{w}}$	Surface tangential vector	--
T	Temperature	K
u	Velocity component in the *x*-direction	m s^{-1}
v	Velocity component in the *y*-direction	m s^{-1}
w	Velocity component in the *z*-direction	m s^{-1}
W	Width	m
x,y,z	Cartesian coordinate components	

Greek letters

α	Volume fraction	--
κ	Interface curvature	m^{-1}
ρ	Density	kg m^{-3}
μ	Dynamic viscosity	kg m^{-1} s^{-1}
σ	Surface tension coefficient	N m^{-1}
λ_i	Relaxation factor for mass transfer between phases	s^{-1}

Subscripts/superscripts

a	Adiabatic

B	Background
f	Fluid
h	Heater
HP	Hotspot
i	i-Phase
in	Inlet
j	Mesh
l	Liquid phase
L	Longitudinal
mf	Main fins
sat	Saturation
si	Silicon
T	Transversal
v	Vapor phase
w	Wall
wz	Wall zone

SUMMARY

The microelectronics industry has been driven by the trends of miniaturization and increased functionality; however, the increased complexities and costs of processing due to reaching the physical limits of silicon have prompted the industry to find alternative solutions. The three-dimensional stacking of integrated circuits (3D ICs) represents a promising technology that has been intensively pursued in the last years due to a number of features such as increased performance and functionality by allowing the vertical integration of heterogeneous devices such as logic, memory, radio frequency, etc. One of the main advantages of such approach is the reduction of electrical delay by shortening the interconnection lengths; however, a tradeoff exists in the sense of reducing the available volume for heat dissipation due to the narrow gap that is created between device layers, where conventional cooling technologies such as heat sinks or cold-plates cannot be used. Microfluidic interlayer cooling is a feasible solution for the thermal management of such devices, but several challenges remain to achieve a comprehensive solution that is compatible with electrical and structural considerations.

In the present work, different thermal demonstration vehicles (TDVs) are numerically and experimentally studied in an effort to provide a practical cooling solution for 3D ICs and conciliate the multidisciplinary challenges of such. A contribution is made in the single and two-phase modeling by proposing an approach that is capable of accurately predicting the fully-resolved temperature and flow fields across the entire cooling layer and capturing non-trivial aspects such as hotspot cooling. The model is successfully validated by in-house experiments in the TDVs with variable pin fin

densities over a wide range of operating conditions, therefore proving the suitability of the modeling technique for designing virtually any type of cooling layer given a powermap layout.

On a more fundamental side of this work, the physics of two-phase flows, in specific flow boiling in such cooling layers, are extensively studied by means of proposing and adapting a mechanistic phase change model that can be used with commercial computational fluid dynamics and heat transfer (CFD-HT) codes. The model was tested and developed starting from flow boiling simulations in a single microchannel and compared with flow boiling correlations, until the point of simulating cooling layers with variable density of pin fins and hotspots, and validating with in-house experimental data generated for the purpose of studying the two-phase flow regimes, their thermal and hydraulic implications and how they can be predicted through detailed CFD-HT models for the ultimate goal of constituting a valuable tool in the design and analysis of heterogeneous microfluidic cooling devices.

CHAPTER 1. INTRODUCTION

Microelectronic devices are one the main pillars of modern technology and society; in fact, the Third Industrial Revolution, also known as Digital Revolution, was specifically defined by the transition from analog to digital devices and characterized by the ground-breaking introduction of personal computers (PCs) and the Internet. Similarly, the ongoing Fourth Industrial Revolution (or Industry 4.0), relies on the advancement of such microelectronics and their significant impact on industrial processes and consumer markets. Such technology has made possible remarkable progress in fields such as high-performance-computing (HPC), robotics, artificial intelligence (AI), autonomous vehicles, and the Internet of Things (IoT).

The evolution of microelectronics has been mainly characterized by the trend of decreasing the transistor sizes in order to perform increasingly complex computing instructions at higher speeds. The concept is easy to understand: the smaller the internal transistors, the shorter the distance that signals have to travel and therefore the faster the device will compute a given calculation. This trend has been closely captured in the evolution of semiconductor integrated circuits (ICs) during the past 50 years with the well-known Moore's law, which indicates that the number of components per integrated circuit would double approximately every two years [1]. In the original publication by Gordon E. Moore [1] in 1965, he forecasted that by the year of 1975, as many as 65,000 components could be crammed in only about one-fourth of a square inch. It is thrilling to read a number of statements looking ahead of their time, such as "*I believe that such a large circuit can be built on a single wafer*", and then realizing that current transistor counts in publicly disclosed processors are nearly at 20 billion components (a mind-blowing 300,000x increase); no other technology in the history of humankind has evolved and had such big impact on society as the microelectronics one.

1.1 Current challenges in the microelectronics industry

Despite such remarkable advances in this industry, recent reports [2, 3] have indicated a slowdown in the Moore's law as the commercial release by the industry leader Intel® of the 10 nm transistor technology for consumer chips has been delayed by more than 2 years now, as it was expected for mass production by the fourth quarter of 2015 [3]. On April 2018, the company indicated that due to the low yield rates with the 10 nm process, mass production would be pushed out to 2019.

The foundry business is a very competitive and expensive field, which has led to the reduction of competitors capable to invest billions for new node processes. According to the Samsung Foundry data [4], for the 130 nm process there were 22 companies capable of manufacturing microelectronic devices with such size features, but for new and smaller processes, the fab investments and process development costs skyrocketed, therefore leaving just 4 contenders after the 28 nm node process. At present, the most advanced microchips on which a large part of the global economy depends (PCs, high-end smartphones, servers, and other IT components) are currently manufactured by gigantic companies such as Intel, Taiwan Semiconductor Manufacturing Company (TSMC), Global Foundries, and Samsung. Figure 1.1 depicts the aforementioned trends, clearly indicating the reduction in competition as shrinking transistors is still possible, but not cheaper than it used to [4].

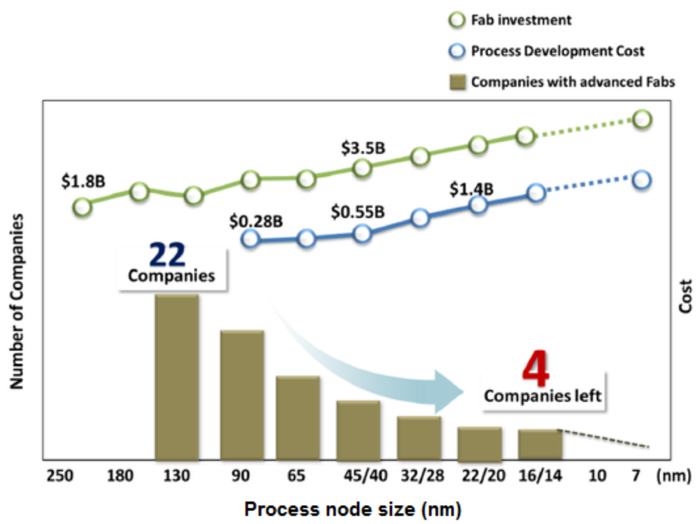

Figure 1.1 – Reduction in the number of foundry companies for different process nodes. (Source: Samsung Foundry data) [4].

Besides the aforementioned microfabrication challenges, the semiconductor industry will also eventually face fundamental limitations as the transistor sizes are reduced and approaching physical barriers. In the work by Muller et al. [5], it was demonstrated that the thinnest operational silicon dioxide (SiO_2) gate dielectric reaches a fundamental limit at 0.7 nm; such dimension is only 4 silicon atoms across and represents the boundary at which the electrical and optical properties depart from the required bulk values for operation.

Although performance gains and benefits between leaps in current lineups of products are still remarkable, it is clear that the increased complexities/costs in lithography and wafer processing techniques have begun to impact this industry, prompting the research of new solutions and fostering the pursue of new ideas and concepts for increasing computing performance and functionality; silicon-based microelectronics will remain as the most cost effective solution for a number of markets, and a lot of opportunities exist to push such technology forward.

1.2 Vertical stacking of microelectronics

The vertical stacking of integrated circuits (ICs) has been proposed and extensively pursued in the last years as an alternative to planar electronics, in which better signal transmission and reduced power consumption can be obtained by shrinking the interconnection lengths from millimeters (planar) to micrometers (vertical). As indicated by Meindl [6], interconnects play a limiting role in the latency of microelectronics; for example, the latency of a 10 nm process transistor is nearly 0.1 ps, corresponding to the same latency of value of an electromagnetic wave front traveling a distance of 30 μm. Hence, this indicates that even in an ideal scenario having a superconductor interconnect, as soon as its length surpasses 30 μm its latency will be exceeding that of the 10 nm transistor. Considering that such interconnection lengths are currently way longer than such discussed values, significant performance improvements can be obtained through a vertical integration approach. Figure 1.2 depicts a comparison between different approaches for microelectronics integration, including the concepts of vertical stacking and their implications regarding interconnection length. Conventionally, logic and memory packages are interconnected in a 2D planar fashion, as indicated in Figure 1.2a, where the interconnection lengths are in the order of centimeters; an example of the actual 2D layout and its dimensions is shown to the right, corresponding to the AMD® RADEON R9 290X graphics card, with a performance benchmark of 5.6 TFLOPS. In recent years, the concept of reducing interconnection lengths in memory packages by vertical stacking has been achieved by the so-called 2.5D integration; Figure 1.2b depicts such type of integration, in which an interposer is used to connect the logic die (xPU) with a stack of memory dies. A commercial example using such type of integration was introduced in the AMD® RADEON Fury X line of graphics cards, in which the logic die (graphics processing unit, GPU) is connected to a stack of memory dies in the same substrate. A significant increase in memory bandwidth and computing performance with a benchmark of 8.5 TFLOPS was measured, as a 52% increase compared with the planar R9 290X model, and a reduction of the footprint area with only 70 mm by 70 mm. In such type of integration, the interconnection length can be reduced to the order of micrometers for the memory and to millimeters to the logic die.

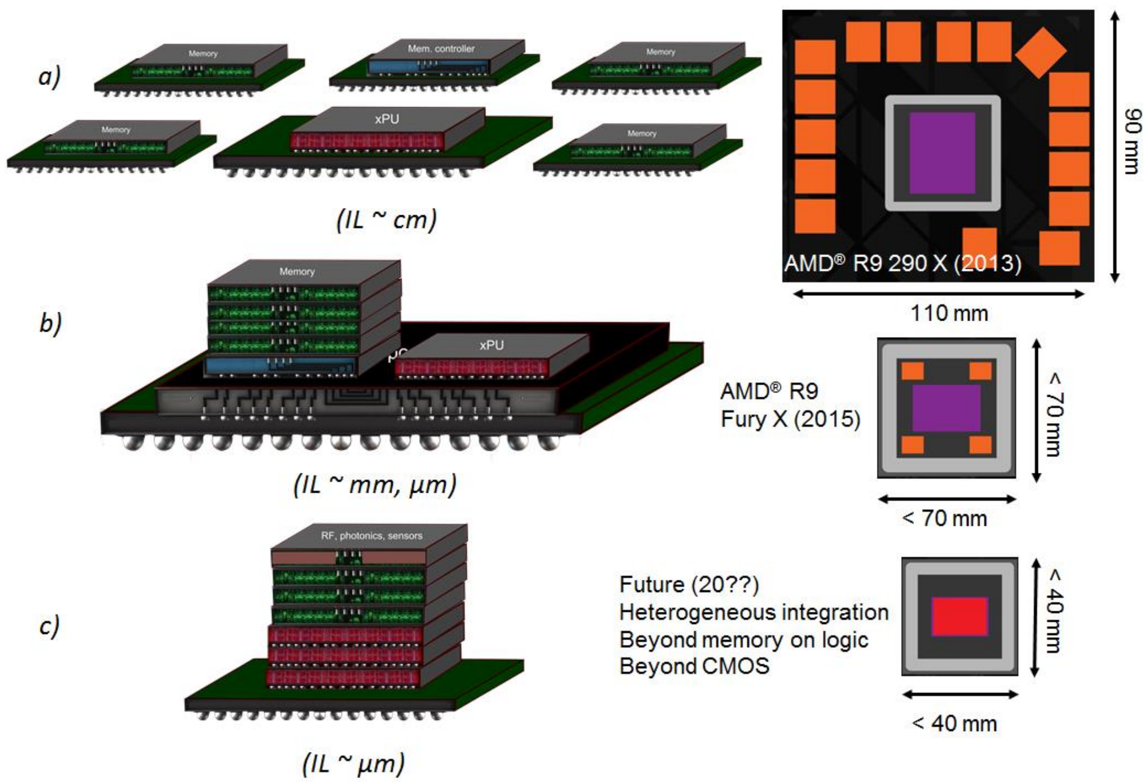

Figure 1.2 – Comparison between different approaches for microelectronics integration: a) 2D (planar), b) 2.5D (planar/vertical), c) 3D (vertical).

Although 2.5D applications offer significant performance advantages over planar electronics, the ultimate goal is achieving the so-called heterogeneous integration in which both logic and memory dies are vertically interconnected in the same stack, therefore reducing all of the interconnection lengths to the order of micrometers and minimizing the effects of latency. Figure 1.2c depicts the concept of full vertical integration, 3D microelectronics, in which not only heterogeneous integration is sought, but also going beyond such and integrate other types of dies for increased functionality such as RF, photonics, sensors, among others. Although such approach hasn't been commercially released yet, due to a number of challenges to be discussed in the next sections, the concept poses a promising alternative for continuing the advancement of the microelectronics industry.

1.3 Thermal implications and challenges of vertical integration

Thermal management has been for a long time one of the main limitations on speed and performance for computing processors. A key metric used to quantify processors' speed is its clock frequency (also known as clock rate or clock speed), which indicates the number of operations per second. For example, a processor with a clock frequency of 4 GHz is capable to perform 4 billion of such operations per second; therefore, for performance applications a high frequency is desired so more can be processed in less time. However, it is quite a challenge to increase such clock frequency due to thermal limitations; a linear increase in frequency grows the voltage consumption (and therefore power dissipation) by a cubic exponent. This is the main reason why most commercial CPUs are stuck between 2 and 4 GHz currently, requiring the use of advanced cooling solutions as these frequency limits are pushed. For such type of microelectronics, the maximum recommended device temperature is 85 °C, where low temperatures are desired as signal delay is affected by such parameter [6]. A plausible approach for such clock frequency and heat removal challenges has been parallelization with multiple compute cores, which although convenient still implies limitations related to the latency issues explained in the previous section, indicating the need of minimizing interconnection lengths through vertical integration.

Based on all of the aforementioned discussion and evidence, all of these roads lead to the vertical integration as a plausible solution for the evolution of microelectronics. However, such approach is not exempted from the thermal challenges; in fact, it is more vulnerable than the case of 2D and 2.5 integration approaches. For the case of the latter, above the silicon die and its package there is a significant amount of available volume that can be used for heat removal, only limited by the dimensions of the enclosure or system casing. Most of the planar electronic systems with high-power logic dies are cooled by using heat spreaders, providing the ability to dissipate concentrated power amounts to larger surfaces; Figure 1.3 depicts such conventional cooling system and the associated thermal resistance network.

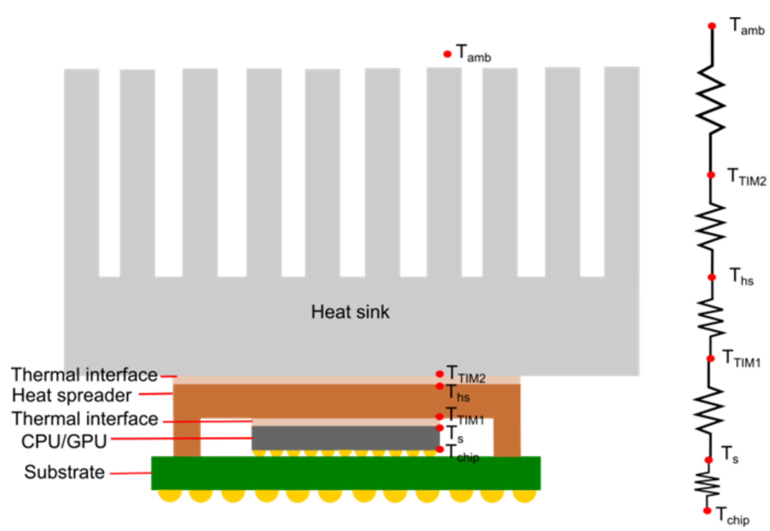

Figure 1.3 – Conventional cooling system for planar microelectronics and its associated thermal resistance network.

The conventional heat sinking method shown in Figure 1.3 has several thermal limitations too, due to the fact of having multiple interfaces (and therefore temperature jumps) that only increase the device temperature. State-of-the-art coolers (heat pipe towers and indirect liquid cooling systems) in the market are capable to remove heat fluxes in the order of 100 to 150 W/cm^2 [7] in cases that are not limited by volume for heat rejection; although a decent number when compared with the limits of conventional air cooling, it still runs short for the heat dissipation targets (from 200 to 1000 W/cm^2) desired in high performance systems [8].

For the case of vertically integrated (3D) microelectronics, the problem of thermal management is even more challenging because of the highly constrained volume that is left available for heat dissipation. Recalling that for a 10 nm process transistor the equivalent latency corresponds to that of a superconductive interconnect of 30 µm, this indicates that for the best performance in such case the separation between vertically connected dies should not be larger than this value. In addition to the problem, the silicon dies in a 3D stack have a very poor thermal contact with adjacent chips in the vertical direction due to the use of electrical bumps and insulating layers. Hence, a conventional "on top of the package" cooling solution is not feasible in such approach and the only available volume for heat removal is that formed by the distance between individual dies and their planar extension (typically less than 2 cm^2). Removing the aforementioned values of heat fluxes in such narrow gaps is definitely a big challenge, and it has been a topic of discussion for the last decade with significant number of investigations trying to find a solution.

1.4 Microfluidic interlayer cooling as a solution

Recognizing the challenges and the tradeoff that exists between the available volume for heat removal and the interconnection length, a number of solutions have sought a balance between heat transfer and electrical performance; from the heat transfer perspective, the ultimate cooling solution must avoid any thermal interfaces if there is no volume for spreading. The solution for this part of the problem then suggests that if no extra thermal resistances are allowed into the circuit, the heat sink must then be embedded into the heat source (i.e., the silicon die), so the power dissipation is directly addressed at the chip level.

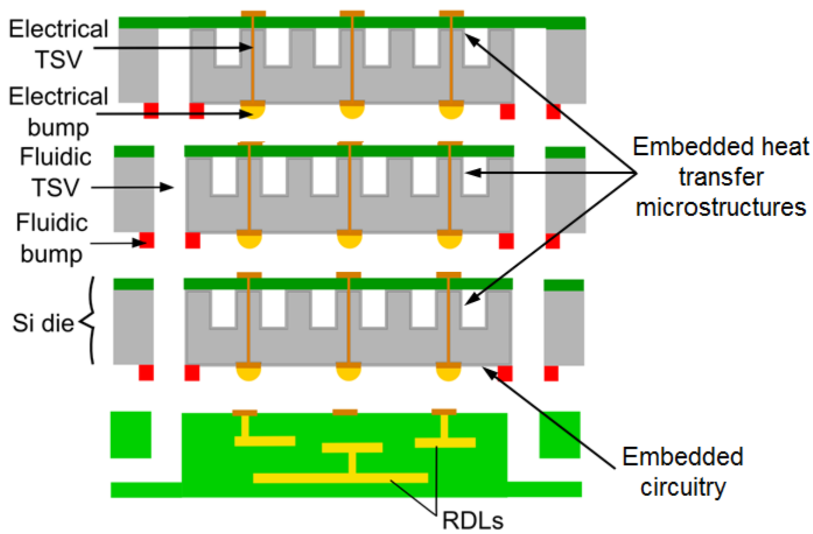

Figure 1.4 – Schematic of the vertical micro-integration (3D) concept with microfluidic passages (not to scale).

Figure 1.4 depicts the concept of microfluidic interlayer cooling. Considering that microelectronics are processed in one side of a silicon wafer, and that such have a typical thickness between 200 and 700 µm, a plausible alternative is micro-fabricating the heat removal structures on the backside of the chip. Once that a relatively large heat transfer surface is available at the chip-level, the other requirement for removing a high heat flux is having a large heat transfer coefficient; this can be achieved by circulating a fluid with desirable thermal properties through the embedded microstructures on the chip. From the electrical standpoint, the shortest interconnection for adjacent silicon dies is of course in the vertical direction and determined by the die thickness; for such vertical interconnect, micro-holes need to be passed from side to side of the die and contain a good electrical conductor. These features are referred to as electrical Through Silicon Vias (TSVs), and provide means of fast signal transmission between each layer, as indicated in Figure 1.4. For coolant manifolding and interconnection between layers, micro-holes can also be fabricated and these are known as fluidic TSVs, providing the path for fluid circulation along the die and means for direct heat removal; this significantly reduces the thermal resistance network to 2 components (conduction resistance across the silicon and convective resistance of the fluid), compared with the 5 thermal resistances encountered in the conventional cooling system of Figure 1.3. These features and considerations constitute the basics for 3D integration with microfluidic interlayer cooling, and the following sections are devoted to briefly explain the alternatives and main features of the physical mechanisms for convection in the microlayers.

1.4.1 Single-phase microfluidic cooling

As indicated by its name, such convection mechanism refers to the fluid circulation in only one phase (either gas or liquid). For the case of interest, it was mentioned that a fluid with relatively good thermal properties is desired in order to provide the required heat transfer coefficient; hence, a liquid with low viscosity, high thermal conductivity and specific heat is desired as the coolant. Figure 1.5 depicts a schematic concept of a single-phase liquid cooling layout at the cross-section of a vertically assembled system with 3 silicon dies; a liquid coolant enters from the left side, and exits the system from the right side also as a liquid, but at a higher temperature due to heat removal from each layer and the sensible heat of the liquid.

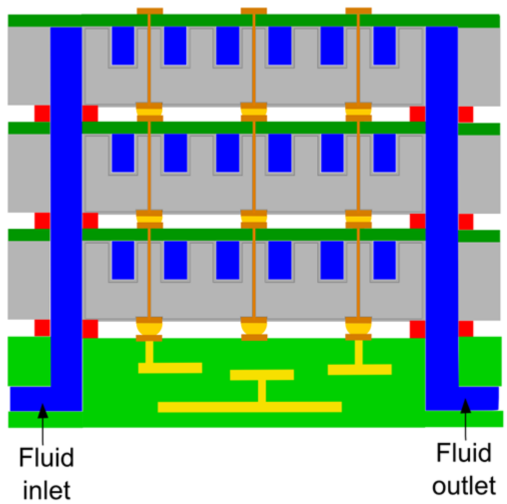

Figure 1.5 – Schematic of single-phase microfluidic cooling in a 3D IC stack.

Figure 1.5 depicts a schematic concept of a single-phase liquid cooling layout at the cross-section of a vertically assembled system with 3 silicon dies; a liquid coolant enters from the left side, and exits the system from the right side also as a liquid, but at a higher temperature due to heat removal from each layer. The sensible heat of the liquid is the main mechanism for such type of cooling approach, in which there is a change in the mean fluid temperature of the liquid with no change in volume.

Single-phase cooling is an extensively studied approach that has demonstrated several advantages in the microfluidic cooling of stacked ICs, such as a stable and reliable operation, capability to handle high heat fluxes under adequate flow rates, straightforward behavior and predictability in most cases, among others.

1.4.2 Two-phase microfluidic cooling

For the case of two-phase microfluidic cooling in stacked microelectronics, the latent heat of vaporization of the liquid is used to remove the heat from each layer through a phase change process also known as flow boiling. Figure 1.6 depicts a schematic of this process, in which the coolant enters the stack in the liquid phase (near its saturation temperature) and then starts to boil as a result of heat absorption from each layer; the formed vapor structures coalesce in the downstream direction and exit the system as the indicated vapor slug structures (liquid/vapor mixture).

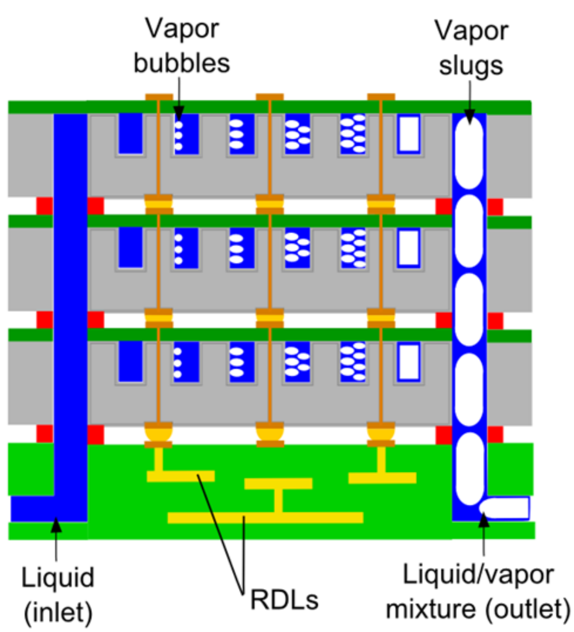

Figure 1.6 – Schematic of two-phase microfluidic cooling in a 3D IC stack.

The thermal management of stacked ICs through flow boiling has received significant consideration in recent years as an alternative to removing high heat fluxes, with the benefits of relatively low flow rate requirements and near uniform surface temperatures, slightly above the fluid saturation temperature. The use of the latent heat of vaporization in such approach also makes it a good candidate to adopt dielectric refrigerants and offset their relatively low specific heat and thermal conductivity when compared to other electrically-conductive liquids.

1.5 Remarks

The main objective of this introduction section was raising awareness of the current integration and thermal challenges in the microelectronics industry, laying a solid motivation for the present thesis work. Microfluidic cooling was introduced as a feasible solution to remove relatively large heat fluxes in small volumes, providing the features of vertically interconnecting several dies while keeping each layer at design temperatures. After explaining the basic concepts and possible microfluidic cooling approaches for the vertical integration of ICs, the specific topics to be addressed in this investigation are explained in the next chapter.

CHAPTER 2. LITERATURE REVIEW AND RESEARCH CHALLENGES

This chapter presents a literature review of related investigations to thermal management in vertically stacked ICs, indicating the main research highlights from each study and most relevant outcomes. Although remarkable contributions have been made in the last years for better understanding the heat transfer characteristics in microfluidic cooling applications, there are still a number challenges to be addressed from both applied and fundamental perspectives. The present literature review has helped to identify the state-of-the-art in the microfluidic cooling technology and determine the current opportunities for research in this area.

2.1 Review on single-phase cooling investigations

The first demonstration of single-phase microfluidic cooling may be attributed to the groundbreaking study presented by Tuckerman and Pease [9], where the removal of heat fluxes as high as 790 W/cm^2 was achieved by circulating liquid water through an array of parallel microchannels embedded on a silicon substrate with channel and fin widths of 50 µm and 302 µm depth; the substrate area for such array of straight microchannels was indicated as 1 cm^2. Results indicated that at such high heat flux value, a maximum surface temperature difference of 71 °C between inlet and outlet was measured, with a pressure drop of 203 kPa. Motivated by these promising results, the remaining concerns (such as high temperature gradients and pressure drop) have propelled a large number of studies in the literature dealing with different configurations and approaches [10-24]. The use of microscale cylindrical pin fins as surface enhancement structures was proposed in the work by Peles et. al. [10], where it was demonstrated that the thermal and hydraulic performance across an array of such microstructures was superior to that using a microchannel approach. It was reported that under the same heat flux and pressure drop values in the study of Tuckerman and Pease [10], the micro pin fin cooling layer was capable to reduce the surface temperature rise to a value of 30.7 °C, a significant decrease when compared with the 71 °C value reported in [10]. The main reasons behind these improvements are related to the fact that forced convection benefits from the transversal fluid mixing when using an array such microstructures, the continuous boundary layer interruption as the flow moves downstream and separates at the pin surfaces, and the increase in heat transfer area. The effect of alternative pin fin cross-section shapes, arrays, spacing and improvements to the silicon micro pin fin heat sink of [10] have been studied in the multiple studies by Kosar et al. [11-13].

The heat removal of fluxes up to 500 W/cm^2 with a relatively low flow restriction resulting in a pressure drop of 65 kPa, was reported in the investigations by Colgan et al. [14-15]; a two-layer heat sink featuring a staggered array of elliptical pin fins with multiple inlets and outlets, was used in such study with liquid water as the coolant. Zhang et al. [16] experimentally analyzed the thermal characteristics of a microfluidic cooling layer for 3D ICs with cylindrical micro pin fins of 150 µm in diameter and height of 200 µm in a staggered array; it was demonstrated that such design was capable of sustaining the stack temperature below 50 °C for heat fluxes up to 200 W/cm^2. In a complimentary study by Zhang and Bakir [17], the same micro-cooling layer design from [16] was used for independent tier cooling of a two-processor stack with different heat fluxes, reporting significant advantages when compared with forced air-cooling. Alfieri et al. [18] proposed liquid cooling for a 3D stack constituted by four chips with a through-silicon-vias (TSV) length of 150 µm and channel height of 100 µm, reporting the dissipation of 135 W/cm^2 using water with a pressure drop of 110 kPa. More recently, the heat transfer and hydraulic characteristics of microgaps with pin fins, and the effects of the Reynolds number, geometry and spacing have been reported in the study by Wan and Joshi [19]. Results from such investigation suggest that circular cross-sections offer the best balance and performance for fixed operating conditions.

An important challenge associated with single-phase cooling is that as the mean fluid temperature increases downstream due to its sensible heat, the wall surface temperature is offset in a similar fashion for fully developed conditions, leading to the non-desirable high temperature gradients from inlet to outlet. Recently, the concept of introducing a variable density of pins has been proposed as a solution to homogenize the device temperature by increasing the available area for heat transfer in the flow direction [20, 21]. Rubio-Jimenez et al. [20] reported a numerical investigation of variable fin density arrays, assessing the effects on performance of geometrical parameters such as fin length, height, and cross-section shape. It was suggested that by increasing the fin density in the flow direction, a more uniform temperature distribution may be obtained and reduce the pressure drop when compared with a uniform array of pins. A maximum heat flux of 230 W/cm^2 with a pressure drop of 29.5 kPa, with water as the coolant, was predicted by their numerical model with maximum temperature gradient within the heat sink of 10 °C. Lorenzini and Kandlikar [21] proposed different configurations of interlayer coolers for 3D ICs with a variable density of offset strip fins for channel and TSV heights (die separation) as low as 100 µm, indicating the removal of an equivalent heat flux of 200 W/cm^2 with a pressure drop of 34 kPa using single phase water, and a maximum temperature gradient on the silicon surface from inlet to outlet below 30 °C.

In addition to the relatively high heat fluxes and constrained volumes, another relevant challenge in the practical application of 3D ICs is the highly heterogeneous heat flux distribution (power dissipation map) that arises from the specific microelectronic architecture and computational load. Core regions are known to have the largest concentrated power in small areas, leading to the formation of localized hotspots. Most of the reported layouts with uniform distribution of microchannels or micro pin fins have the disadvantage of undercooling hotspot areas due to both the insufficient local heat transfer coefficient and inadequate surface area; it is very relevant to figure out strategies to increase both of these parameters, and different approaches have been suggested in recent years [22, 23]. Green et al. [22] presented the concept of a hybrid fluid-to-fluid, spot-to-spreader (F2/S2) heat sink that uses two separate flow loops per tier, with one fluid of high thermal conductivity and specific heat (e.g., water) dedicated to hotspot regions only, and a second fluid of easy circulation (e.g., air) used for removing the background heat fluxes. Successful removal of up to 365 W/cm^2 in hotspot regions and background heat fluxes of 20 W/cm^2 was experimentally demonstrated, with pressure drops lower than 100 kPa with a separate thermal control design. Sharma et al. [23] presented a numerical study to assess the concept of hotspot-targeted manifold microchannel heat sinks with multiple inlets and outlets using water as coolant, in which narrow channels are defined in the hotspot areas, while wider channels are used to cool background zones. Model results predicted the capability of this design to remove hotspot heat fluxes up to 300 W/cm^2, in combination with a background heat flux of 20 W/cm^2 with a pressure drop below 35 kPa. More recently, Wan et al. [24] investigated the co-design of a 16-core architecture using a compact thermal model with liquid cooling through microgaps with pin-fins, employing a realistic localized heat flux input to the model.

2.1.1 Challenges and proposed contributions to the single-phase cooling of stacked ICs

Based on the previously discussed review of relevant studies of single-phase cooling in microsystems, the current challenges for this approach have been identified as follows:

- *Temperature non-uniformities:* Relatively high temperature gradients arise due to the increase of the mean fluid temperature in downstream locations as the heat is absorbed by the coolant; these issues are worsened in cases where the heat flux distribution is heterogeneous, therefore requiring the development of mitigation strategies.
- *Detailed modeling techniques:* Although there are several approaches for predicting the thermal and hydraulic characteristics in micro cooling layers, most empiric models are limited to simple geometries and uniform heat fluxes. The literature review indicated that most studies using CFD-HT modeling for single-phase cooling in these applications are limited; there is scarce literature addressing the modeling of realistic applications with hotspots and variable heat fluxes.
- *Oversimplified cooling layers:* Conclusions from the literature survey indicate that existing numerical and experimental studies neglect important aspects of practical applications for vertical integration of ICs, such as the inlet/outlet manifold design and implications in flow distribution, use of surface enhancement structures compatible with vertical interconnects, structural considerations to withstand high flow rates/pressures, and very importantly, non-uniform heat flux distribution. Although different studies may be found for

each of these considerations, these focus on a single feature and fail to consider the combined effect of other aspects.

Based on the aforementioned challenges, the proposed dissertation will strive to provide a solution to each by assessing the single-phase cooling in microgap cooling layers that comply with design considerations for their actual implementation in stacked ICs. It was identified that there are breaches in the literature relating numerical and experimental studies; while most experimental studies discard the comparison with modeling, numerical studies often fail to provide a relevant validation of their model. The present work intends to bridge these gaps by proposing an approach that is capable of accurately predicting the fully-resolved temperature and flow fields across the entire cooling layer and capturing non-trivial aspects such as hotspot cooling. Unlike existing literature, the model will be fully-validated with in-house experimental data and will capture the entire details of relatively complex cooling layers, therefore representing a cost-effective thermal modeling technique that may be applicable to virtually any type of heat flux distribution or power map, and IC architecture, for a realistic design. Benchmark simulation cases of reduced computational domains will also be described and validated with the corresponding experiment, with the objective of providing a more relevant case of validation for numerical studies of microgaps with pin fins.

2.2 Review on two-phase cooling investigations

The heat transfer phenomena associated with flow boiling in microsystems is not as well understood as it is for the case of single-phase cooling; significant challenges are related to the control of flow instabilities, critical heat flux (CHF), flow regime transition, and two-phase pressure drop. Several reviews regarding the challenges and opportunities on flow boiling in microchannels [25-29] have given some guidelines for future design and analysis of such systems.

Krishnamurthy and Peles [30] investigated the features of flow boiling of water in a silicon device with a flow channel 250 µm high and 1.8 mm width, populated with cylindrical pin fins of 100 µm diameter. The device was powered at the bottom with heat fluxes ranging from 20 to 350 W/cm^2 and mass fluxes in the range of 346 to 794 kg/m^{2}s; the reported wall temperatures ranged between 100 to 140 °C, due to the saturation properties of water above atmospheric pressures. Koo et al. [31] investigated a one-dimensional thermal model to predict the cooling performance of a 3D IC with an integrated microchannel network using flow boiling for the removal of heat fluxes up to 135 W/cm^2 with a maximum temperature of 85 °C. In the investigation by Kim et al. [32], the single and two-phase cooling of a 3D-stacked IC was analyzed with a reduced-order model for a non-uniform power map corresponding to a dual-core microprocessor, with localized heat fluxes ranging from 11.3 to 305 W/cm^2. The implications on heat transfer, microchannel layout, and flow directions were reported and provided suggestions for the optimization of such devices.

In the experimental investigation by Han et al. [33], the flow boiling of water was assessed in a silicon microgap 200 µm high and 10 mm width over a 1 cm^2 heated area, populated with cylindrical pin fins of 90 µm diameter in a staggered array. The device was tested for heat fluxes ranging from 198 to 444 W/cm^2, and mass fluxes from 1351 to 1784 kg/m^{2}s. In an effort to reduce the operating temperatures, subcooled water was supplied to the device at sub-atmospheric pressures; results indicated a maximum wall superheat of 60 °C at a heat flux of 444 W/cm^2. Water has been the preferred coolant in several studies due to its superior thermophysical properties, such as high thermal conductivity and latent heat of vaporization, when compared with other fluids. However, reliability concerns, such as the direct contact of the coolant with the device in interlayer configurations, have prompted the use of dielectric refrigerants instead of water. Asrar et al. [34] experimentally studied the flow boiling of the dielectric refrigerant R245fa in a silicon microgap 200 μm high and 10 mm width, with pin fins of circular cross-section shape covering a 1 cm^2 heated area. The cooling performance was assessed for heat fluxes up to 498 W/cm^2 mass flux values up to 7896 kg/m^{2}s, and inlet temperatures of 13 °C and 18 °C, while also discussing on the observed two-phase flow regimes.

Modeling has been identified as one of the main challenges for the development of superior cooling technologies and understanding of boiling phenomena; despite the encouraging experimental evidence that suggests two-phase cooling as a potential candidate for the 3D-stacking of ICs, the detailed thermal modeling of such has lagged behind due to the complexity of the involved phenomena. Although this type of modeling is computationally intensive, the development and refinement of new and current models can eventually lead to more cost-effective tools for optimizing and analyzing these systems; considering the expensive, time-consuming, and complex processes related to the microfabrication and testing of experimental prototypes. Several challenges remain to improve the capabilities of the available multiphase models, in particular for incorporating the analysis of phase-change phenomena. The CFD analysis of boiling requires the coupling of a multiphase flow model with a phase-change model to estimate the heat and mass transport across the interface. Despite inherent modeling limitations and assumptions, a few modeling efforts regarding this topic have been presented. Wu et al. [35] and Yang et al. [36] investigated the induced two-phase flow regimes due to boiling of refrigerant R141B in an evaporator coiled tube using the mechanistic phase-change model proposed by Lee [37], with coupling to the Volume of Fluid (VOF) method for interface tracking. The presented results indicated a remarkable capability to predict the flow regime evolution when compared to experimental results. De Schepper et al. [38] presented a similar phase-change model, comprehensively describing its features and limitations in order to simulate the flow boiling of a hydrocarbon feedstock; the authors indicated that the predicted flow regimes were in accordance with experimental results available in the literature. Fang et al. [39] studied the flow boiling inside a microchannel with a hydrophobic vapor-venting membrane in an effort to reduce flow instabilities and vapor phase accumulation, where the phase-change model was adapted from the work of Yang et al. [36]. The bubble dynamics and condensation process due to subcooled flow of refrigerant HFE 7100 were numerically analyzed by Zhuan and Wang [40] using the model of Plesset and Zwick [41] to predict bubble growth; the authors indicated that their results were in good agreement with a range of experimental data. More recently, Magnini and Thome [42] presented the numerical simulation of saturated flow boiling in a circular microchannel by using the VOF method with extra functions to improve the surface tension calculation and to include the phase-change, based on the kinetic theory of gases.

2.2.1 Challenges and proposed contributions to the two-phase cooling of stacked ICs

Although this approach offers inherent advantages over other methods, such as relatively low flow rate requirements and near uniform surface temperatures, after the literature survey the following challenges were identified:

- *Lack of two-phase CFD-HT models:* Modeling has been identified as one of the main challenges in the development of this cooling technology and a better understanding of boiling phenomena; this important area has lagged behind experimentation due to the complexities of simulation of two-phase flow with involved phase-change. Although there are scarce publications regarding this topic, most of them are basic and not appropriate for designing/understanding the two-phase cooling in stacked ICs.
- *Technology validation:* Although different experimental studies were found in the literature, a number of them do not to consider the aspects of vertical integration discussed in the introduction. It is of critical importance to experimentally study the flow boiling characteristics in microgap cooling layers specifically designed for this purpose.

Based on the aforementioned challenges, there were identified a number of opportunities to expand the research of this developing area. On a more fundamental side of this work, the physics of two-phase flows, in specific flow boiling in microgap cooling layers, will be extensively studied by means of proposing and adapting a mechanistic phase change model that can be used with general-purpose CFD-HT codes. Due to the fact that there are not available models for the simulation of such cases, the modeling techniques and implications will be discussed as they evolved with the development of this dissertation until reaching the point of successfully predicting a number of relevant cases for two-phase cooling in stacked ICs.

In order to assess the aforementioned challenges in the modeling and experimental requirements for validation this technology, both aspects highlight the present dissertation by being the first investigation to experimentally characterize the flow boiling in silicon microgaps with a variable density of pin fins, and with spatial/ temporal variable heat fluxes in Thermal Demonstration Vehicles (TDVs) specifically designed for the vertical integration of ICs. In addition, the results from this experimentation will be used to directly and fully validate the proposed CFD-HT model, therefore providing evidence that such modeling technique is capable to predict the flow regimes, temperature distribution, and two-phase pressure drop in complex cooling layers, with the ultimate goal of constituting a valuable tool in the design of advanced, two-phase cooling microsystems.

CHAPTER 3. EXPERIMENTAL SETUP AND METHODS

This chapter presents the experimental setup, instruments and methods used for measuring relevant and accurate data for the analysis of silicon microgap cooling layers designed to comply with practical considerations of vertical integration. The setup was fully-instrumented in order to assess the temperature, pressure and phase distributions; it is capable to operate in both single and two-phase conditions, and was used for testing different refrigerants under a range of conditions and compared against model predictions.

3.1 Thermal Demonstration Vehicles (TDVs)

As discussed in Section 2.1.1, the present thesis work strives to analyze both practical and fundamental characteristics of the cooling mechanisms in silicon microgaps designed in compliance with the several operation requirements of vertically integrated, high-power microelectronics. The microgap cooling layer must comply with design considerations for 4 major parameters: electrical, structural, hydraulic and thermal, which have been reviewed by Green et al. [43]. Recalling that the motivation behind vertical integration is having interconnects as short as possible, for the practical problem it would be very challenging if not impossible achieving an interconnection length of 30 μm between two adjacent dies. Considering that silicon is a brittle material, substrate thickness and structural parameters must be considered in the design, therefore imposing a constraint on the minimum interconnection length, as discussed in the work by Woodrum et al. [44]. Interconnection length also influences the flow gap height and therefore affects thermal and hydraulic response of the device.

Bearing these multiple considerations in mind, the analyzed microgap cooling layers (or TDVs) in the present thesis constitute an effort to obtain more reliable data, closer to the ultimate application, and use it for model validations for a better understanding of the involved phenomena. Figures 3.1 and 3.2 depict a schematic of the two analyzed silicon TDVs with their relevant geometric features and layout. The silicon microgap has a nominal height of H = 200 µm (slight height variations may arise due to the etching process), subtracted from a silicon wafer of 500 µm thickness. The inlet and outlet plenums are populated with an array of cylindrical pin fins with a diameter of D_{ST} = 500 µm and the same height as that of the microgap (i.e., connecting bottom and top of the flow gap), which serve as structural support features in order to withstand high fluid pressure and allow the circulation of relatively high flow rates.

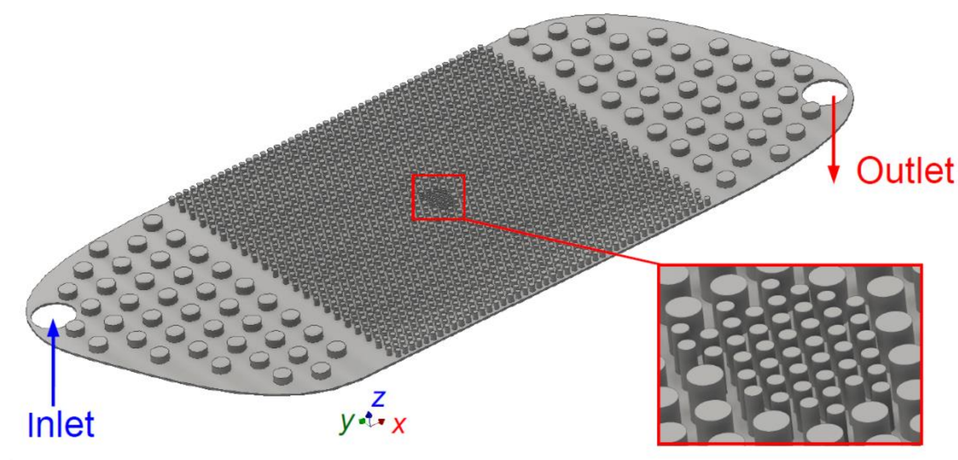

Figure 3.1 – Geometric features of the analyzed silicon microgap cooling layer with a local clustering design.

Both designs have an active heated area (A_h) of 10 mm by 10 mm, distributed in four zones at the back side of the chip as shown in Figure 3.3, with a central hotspot area (A_{HP}) of 500 µm × 500 µm, which allows the heterogeneous heating of the device.

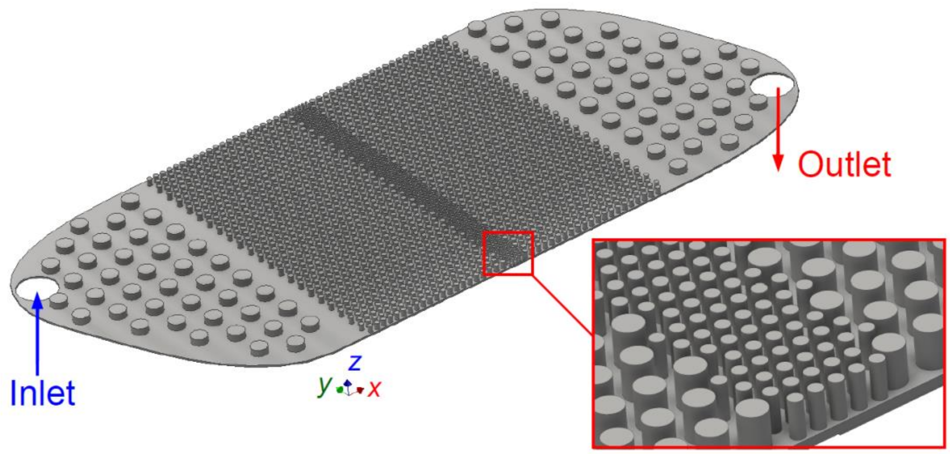

Figure 3.2 – Geometric features of the analyzed silicon microgap cooling layer with a spanwise clustering design.

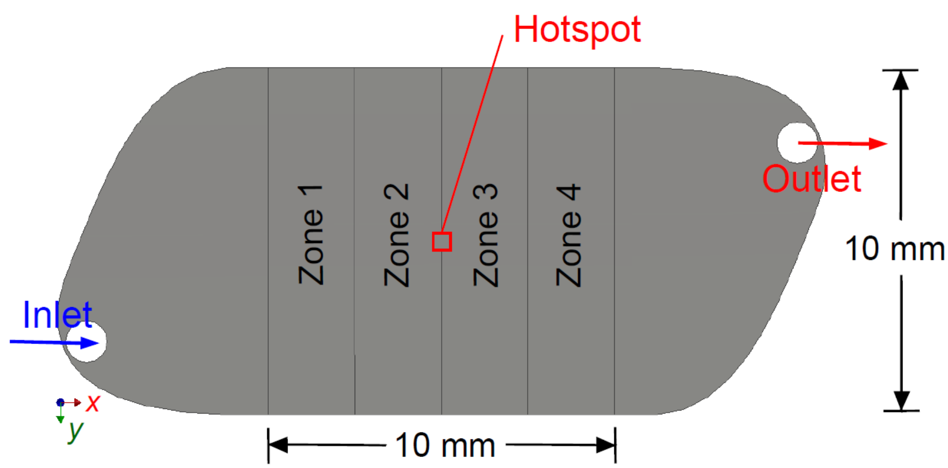

Figure 3.3 – Backside resistive heating of the TDVs, and RTD zone layout.

There is only one difference between the two TDVs, and that is the layout of the variable pin fin clustering near the hotspot; for the first design (local clustering, Figure 3.1) the fin density is just locally increased in the hotspot zone, while for the second design (spanwise clustering, Figure 3.2) the fin density is uniformly increased in the transversal *y*-direction. The objective of choosing these designs is to assess the effects of the flow features (such as bypass) and the corresponding thermal implications.

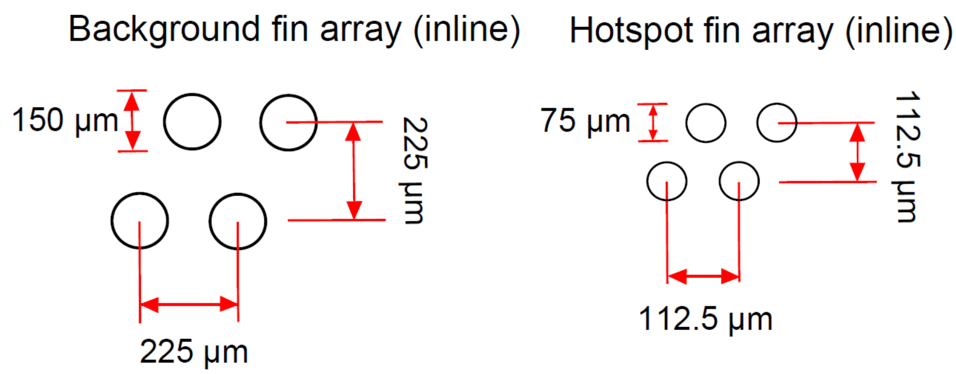

Figure 3.4 – Geometrical array and spacing of the cylindrical micro pin fins.

The active heated area is cooled by an inline array of cylindrical pin fins, which are distributed according to Figure 3.4 depending on whether it is a background or hotspot zone. For background cooling zones, the diameter of the pin fins is D_B =150 µm, with equal longitudinal and transversal pitches (S_T = S_L) of 225 µm. For the hotspot zones, the concept of locally increasing the surface area is employed by reducing the diameter to D_{HP} = 75 µm and both of the pitches to 112.5 µm.

The TDV samples used for the experimental work in this thesis were kindly microfabricated by the research group of Professor Muhannad Bakir at the School of Electrical and Computer Engineering at Georgia Tech. The TDVs were obtained from a double-side-polished (DSP) silicon wafer of 500 µm thickness, using a time-multiplexed etching (Bosch) process for the generation of the different cooling structures and manifolds. The upper side of the sample is anodically bonded to a transparent borosilicate glass window that allows visual inspection during testing. A 2 µm-thick silicon dioxide (SiO_2) insulating layer is deposited on the back side of the samples through the chemical-vapor-deposition (CVD) process. The heaters are deposited at each of the four zones indicated in Figure 3.3 and the hotspot area through the deposition of a 0.2 µm-thick platinum layer; in addition to providing zone-independent heating to the sample, the platinum heaters also serve as resistance-temperature-detectors (RTDs), which yield the zone-average heater/substrate temperature.

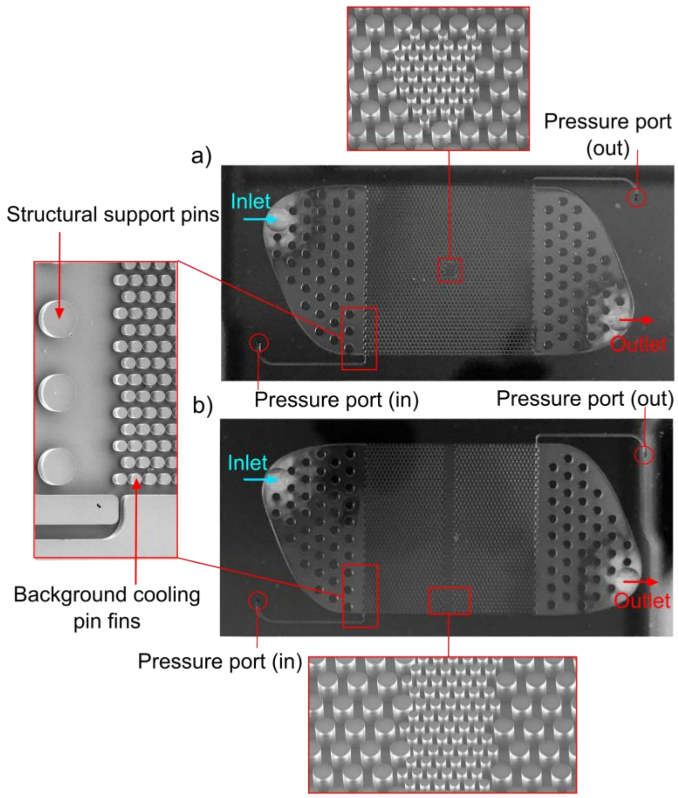

Figure 3.5 – Top view photograph and SEM image details of the microfabricated TDVs: a) local clustering design, b) spanwise clustering design.

Figure 3.5 shows a top view picture of the microfabricated TDVs for the local and spanwise pin fin clustering designs, indicating relevant zones and features such as the inlet and outlet fluidic ports; two pressure measurement ports are located at the beginning and end of the active heated area, which are used to calculate the pressure drop across the main fin array. The magnification boxes in Figure 3.5 show scanning-electron-microscopy (SEM) images which provide high resolution details of the microfabrication features, such as the structural, background and hotspot cylindrical pin fins.

3.2 Electrical connections for test section

In order to experimentally characterize the described TDVs, it was necessary to provide means of electrical connection to the power supply and also visualization of the upper side of the TDV; a Printed Circuit Board (PCB) was used for such purpose.

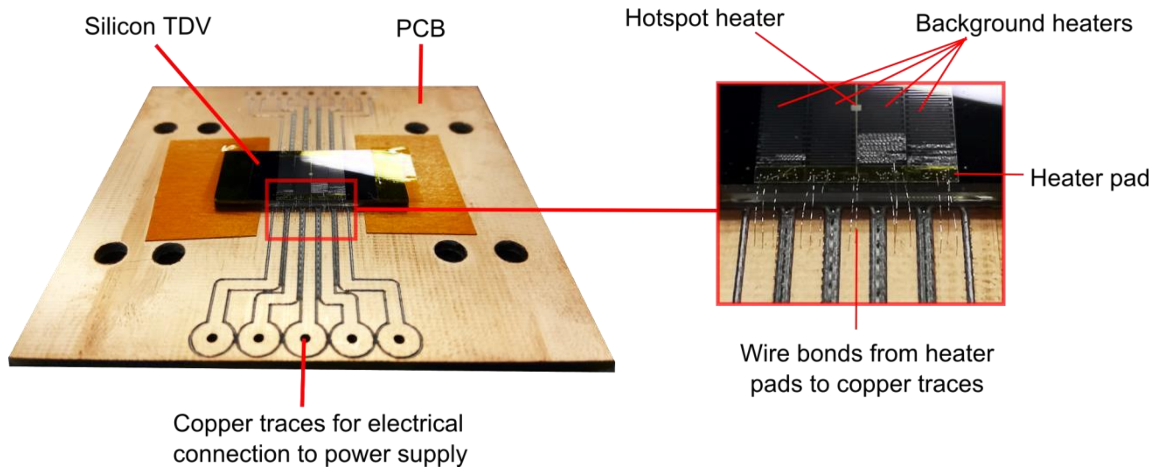

Figure 3.6 – Backside of the TDV/PCB assembly and its main features.

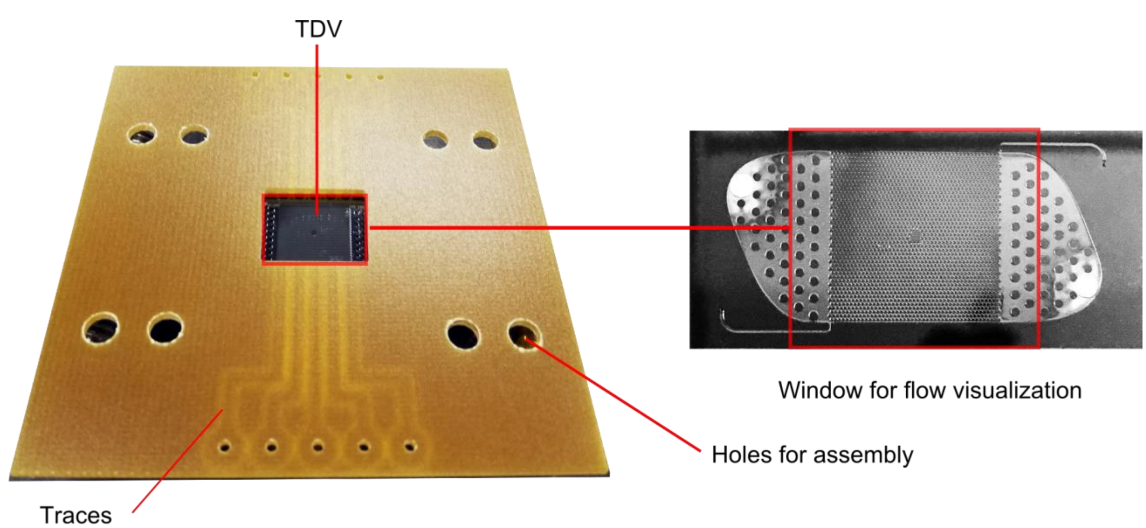

Figure 3.7 – Upper side of the TDV/PCB assembly and its main features.

Figure 3.6 shows a photograph of the backside of the TDV/PCB assembly, indicating the location of the different platinum RTD heaters and also the wire bonds used for fanning out the electrical pads for each of these heaters at the TDV to the copper traces that were precision-machined onto the conductive side of the PCB. A 5-pin screw-compression terminal was then soldered to each of the end sides of the copper traces, allowing the electrical connection to the power supply and independent heating of each RTD. Figure 3.7 shows a photograph of the upper side of the TDV/PCB assembly, which shows the machined pocket at center of the PCB in order to allow the flow visualization through the transparent borosilicate glass that seals the TDV.

3.3 Fluidic package and assembly of the TDV test section

The test section needs to be assembled in such a way that allows probing of the different flow variables; such test section is formed by assembling the TDV/PCB and a fluidic package that seals the sub-system and allows connection to standard fittings and probes. Figure 3.8 depicts an isometric view of the fluidic package and the internal conduits that allow the flow routing to the inlet, outlet, pressure and temperature probes of the TDV. The fluidic package was precision-machined from polyether ether ketone (PEEK), chosen because of its desirable properties such as relatively low thermal conductivity (0.25 W/m-K), high melting point (343 °C), and ease of milling. Figure 3.9 depicts a photograph of the assembled test section in the flow loop, which was sealed through nitrile O-rings (placed in the pockets shown in Figure 3.8) when assembling the PEEK fluidic package with the PCB/TDV component. Once the temperature and pressure probes were installed in the designated ports, the test section was connected to hydraulic fittings and brought to vacuum conditions for seal checking.

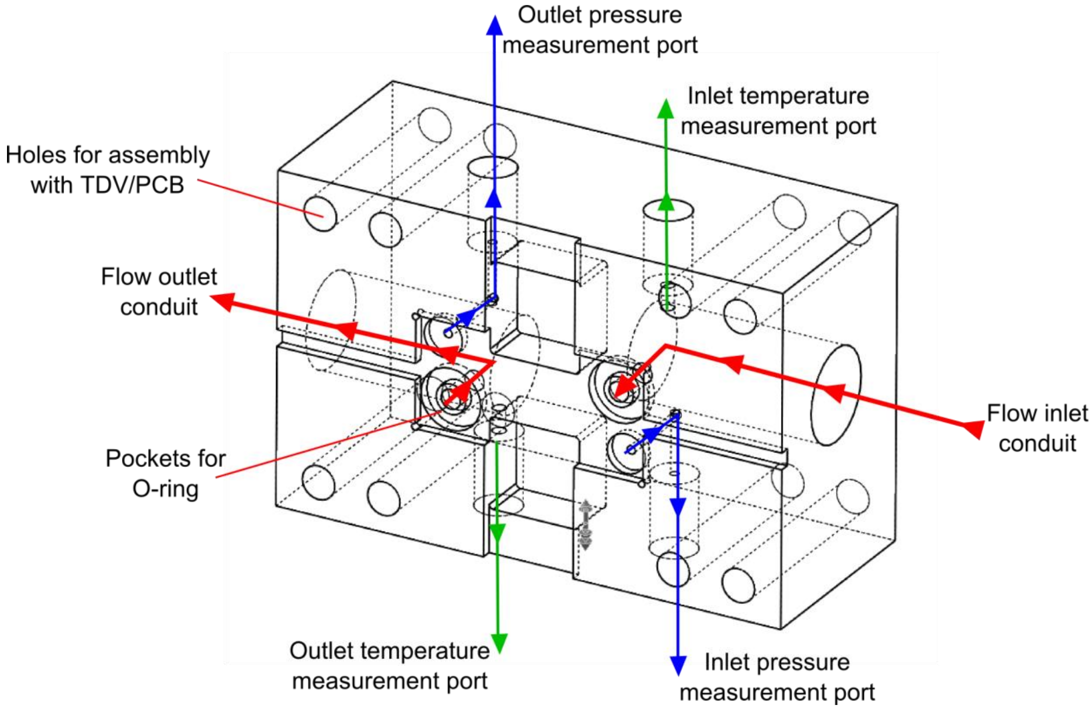

Figure 3.8 – Isometric view of a CAD model for the fluidic package for test section assembly.

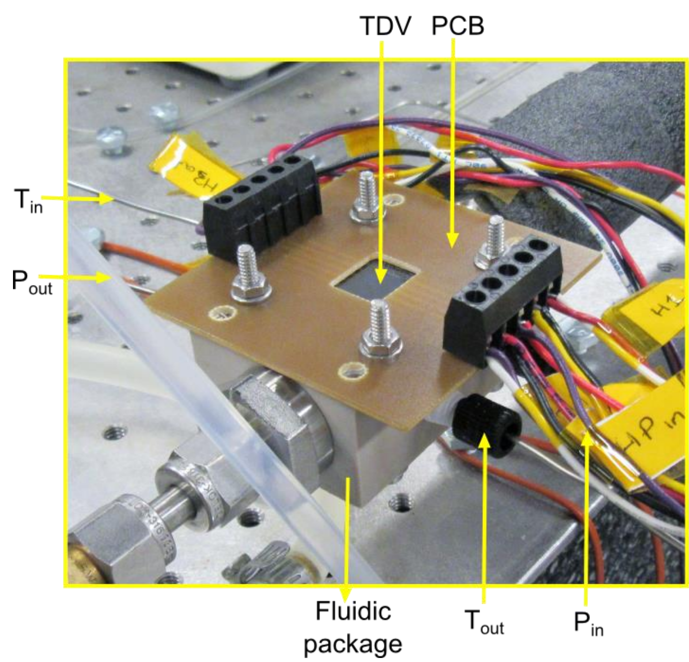

Figure 3.9 – Photograph of the assembled test section and its electrical and hydraulic connections.

3.4 Description of the flow loop and components

Once the TDV test section was assembled, the flow loop components were set up in a benchtop with vibration isolation system (Vibraplane, Kinetic Systems, Inc.) and connected by stainless steel tubing of 3/16" ID and 1/4" OD, and the appropriate compression fittings (Swagelok®). Figure 3.10 shows a photograph of the experimental setup, indicating the main components for the loop, which allow the detailed characterization of relevant flow variables in both single and two-phase conditions. Figure 3.11 depicts a schematic diagram of the flow loop for a better interpretation of how the different components are connected and data is acquired.

The closed-loop system was initially evacuated to an absolute pressure of 5 kPa using a vacuum pump (DV-200N, JB Industries Inc.) connected to the charging point valve; after confirming a completely leakage-free system with the vacuum held for 24 h, the flow loop was charged with the working fluid depending on the test and study (indicated in the individual chapters of results). The flow path is described as follows: starting with the 300 mL stainless steel reservoir (Swagelok®), gravity feeds a digitally-controlled, magnetic drive gear pump (Series GAF, Micropump Inc.), which circulates the fluid through the closed loop indicated in Figure 3.11. The flow rate is measured with a dual-column rotameter (034-39-N, Cole-Parmer®) and then is circulated through a resistance-heated tube serpentine working as a pre-heater that allows increasing the fluid temperature close to saturation conditions (only turned on for two-phase measurements). The fluid then enters a 0.5 μm filter (Swagelok®) that captures any particulates (in order to assure no clogging conditions exist in the TDV), and next it is routed through the fluidic package and TDV assembly as explained in Section 3.3.

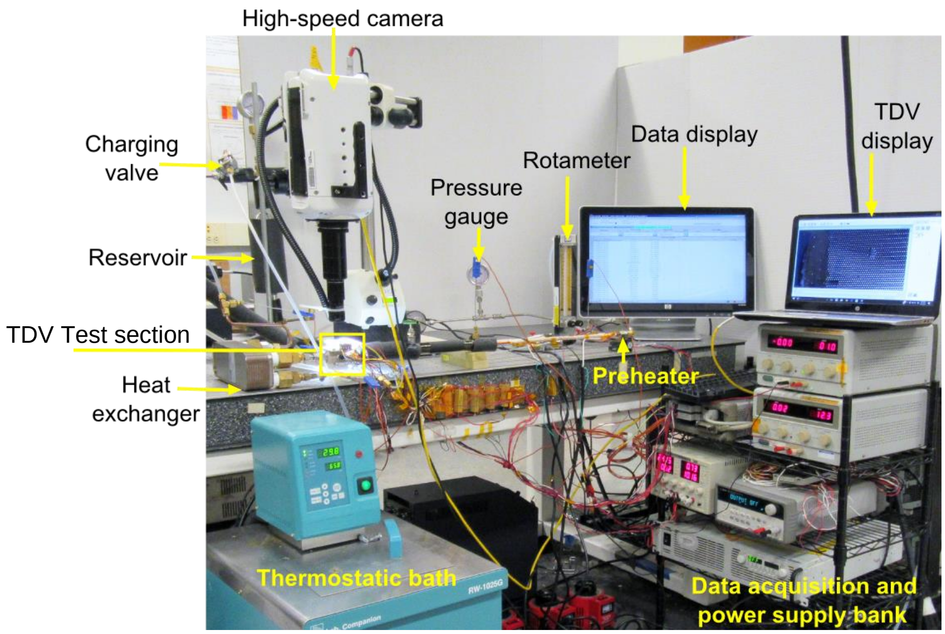

Figure 3.10 – Photograph of the experimental setup and indication of the relevant components.

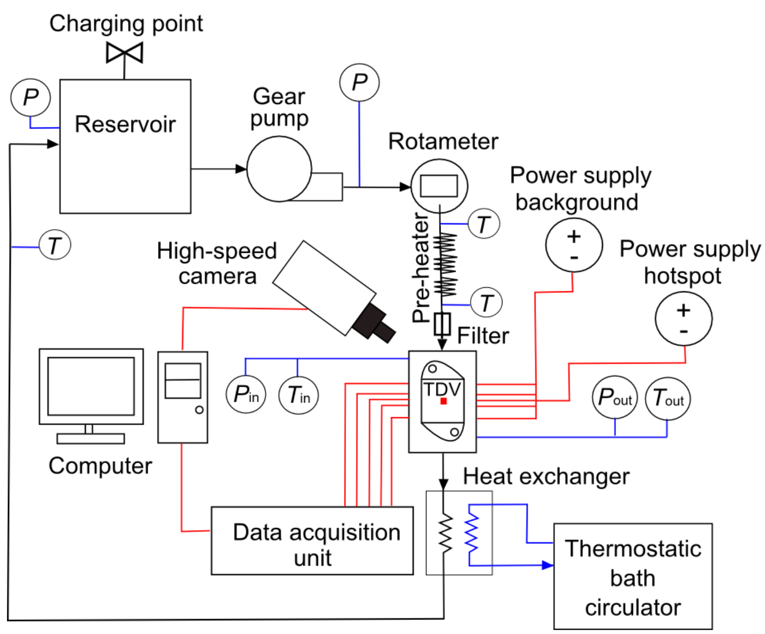

Figure 3.11 – Schematic diagram of the flow loop and layout of components.

After going through phase-change conditions (or just a temperature increase in single-phase conditions) due to heating in the silicon TDV, the resulting liquid/vapor mixture (or heated liquid) at the outlet port flows to a nickel-brazed plate heat exchanger (LL510G14, Lytron Co.); the two-phase mixture is condensed (or the liquid temperature is lowered to room conditions) through heat rejection to a constant-temperature thermostatic bath circulator (RW-1025G, Lab Companion Co.), and the condensed liquid completes the cycle returning to the reservoir, which is in vertical position and includes a vapor trap for any uncondensed gas.

3.5 Data acquisition and methods

Pressure and temperature values are measured at different points in the loop as indicated in Figure 3.11, using type-K thermocouple probes (TMQSS-062G, OMEGA^{TM}) and solid state pressure transducers (PX219-300A5V, OMEGA^{TM}), respectively; the measured values for these parameters were recorded and processed by a data acquisition unit (Agilent 34970A, Keysight Technologies Inc.). The electrical power to the TDV background and hotspot heaters is provided by two independent DC power supplies (Agilent N8742A, Keysight Technologies Inc.) connected to the PCB terminals.

Prior to testing, all of the measurement instruments were calibrated and their uncertainties were calculated. The platinum RTD heaters on the back side of the TDV were calibrated by placing the sample inside a temperature-controlled oven (Lindberg/Blue M, ThermoFisher Scientific, Inc.) and the heater resistance as a function of temperature was recorded in quasi-steady state conditions in the range of 20 to 140 °C, obtaining a linear relationship with R^2=0.999 for each of the RTDs. Figure 3.12 shows the calibration curves for one of the background heaters (Zone 1, other background zones yielded similar correlations) and the central hotspot heater.

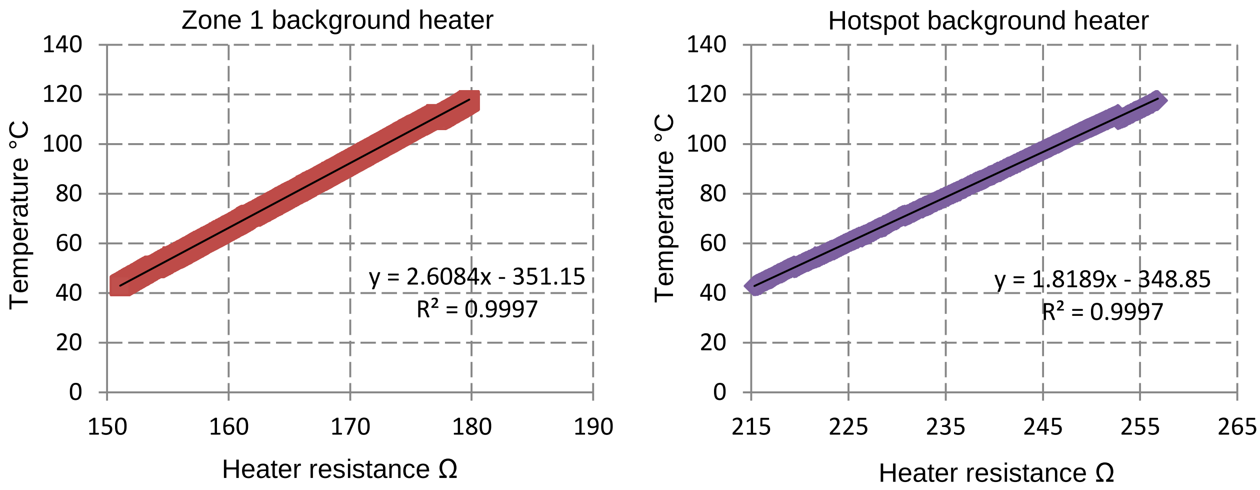

Figure 3.12 – Calibration lines for the RTD heaters and its linear correlations.

The type-K thermocouple probes were calibrated by using a heating/cooling block calibrator (CL122, OMEGA™) with a precision platinum thermometer in the range of 20 to 110 °C. The pressure transducers were calibrated with a pressure calibrator (DPI610, OMEGA™). The rotameter was calibrated by using a high-precision analytical balance (HR-100AZ, A&D Co.) and correlating the mass flow rate to the device, obtaining a linear relationship with R^2=0.999 in the range of 5 to 150 mL/min. Measurements of the voltage/current variation from the power supply were performed to estimate the heat flux uncertainty. The heat loss was estimated by performing single-phase energy balances, and found to be less than 3% of the input power for all of the cases; such value is subtracted from the power supply input in order to correct the heat flux and this is the effective value used for comparison with the developed CFD-HT models. The Kline-McClintock methodology was used in order to estimate the experimental uncertainties [45]; the calculated values for flow rate, pressure, temperature (thermocouple probes), TDV temperature (RTD heaters), and heat flux are ± 0.45 mL/min, ± 0.12 kPa, ± 0.1 °C, ± 0.5 °C, and ± 0.2 W/cm^2, respectively.

The experimental data was acquired after quasi-steady state conditions were reached for each of the analyzed tests, which were assumed once the variations in temperature in each of the RTDs and pressure transducers were within ± 0.1 °C and 0.5 kPa, respectively, in a time interval of 5 min. For the flow boiling experiments, two-phase flow visualization is possible through a high-speed camera (Phantom V11, VISION Research, Inc.) that is focused on the top glass surface of the TDVs; with the capability of recording videos up to 2229 frames per second (fps). The recorded high-speed videos and images were post-processed using the Phantom Vision software included with the high-speed camera.

3.6 Remarks

After presenting the experimental setup and describing its features and capabilities for providing a comprehensive set of data points for characterizing the non-trivial thermal and hydraulic behavior of the TDVs, the following sections are focused to report the most relevant findings of this dissertation in a gradual mode, starting from the single-phase study of the system and its modeling implications, then passing through the evolution nodes to develop a significantly more complex and challenging two-phase modeling approach, until reaching the point of successfully validating the model with relevant experimental data of such TDV operating in microscale flow boiling conditions.

CHAPTER 4. SINGLE PHASE MICROFLUIDIC COOLING IN SILICON MICROGAPS WITH VARIABLE PIN FIN CLUSTERING AND HOTSPOTS

In this chapter, the described TDVs are analyzed for demonstrating the combined and efficient cooling of hotspot and moderate power (background) areas through a comprehensive numerical model, which is fully-validated with experimental results. De-ionized water is used as the coolant through the silicon microgap; the hotspot heat flux is varied from 250 to 750 W/cm^2, while the background heat flux is fixed at 250 W/cm^2. Results indicate the outstanding capability of these designs to keep the maximum temperature of the combined device below 65 °C for an inlet water temperature of 21.3 °C, with moderate temperature gradients and pressure drop. The described CFD-HT model is capable of predicting spatially resolved temperature fields arising from heterogeneous heating. Detailed benchmark simulations are provided, and a reduced domain is suggested so it can be reproduced and used for reference in numerical studies with variable pin fin densities. The described methodology represents a cost-effective thermal modeling technique that may be applicable to virtually any type of heat flux distribution/power map and IC architecture, and therefore a valuable tool for the design of such vertical microsystems.

4.1 Computational model

The numerical modeling is a central part of the present thesis due to the number of advantages that a fully-validated model offers, such as first principle understanding of measured performance data and the dramatic speed increase in the design and optimization stages, considering the complexities, high-cost, and time-consuming characteristics of the microfabrication processes; the details and implementation of the CFD-HT model are given in the next sections.

4.1.1 Model assumptions and thermophysical properties

The numerical solution of the conjugate heat transfer problem relies on the following assumptions:

- Steady state, laminar and incompressible flow.
- Radiation heat transfer effects are negligible.
- Temperature-dependent fluid and solid thermophysical properties are employed.
- Negligible viscous dissipation.

The coolant used for the results discussed in this chapter is water, while the solid domain is the silicon TDV. The dynamic viscosity is a property very sensitive to variations in the mean fluid temperature, which may lead to overestimations in pressure drop as high as 30% if a constant value is assumed [21]. The variation of this property for liquid water may be closely predicted in the range from 273 to 373 K with the following form [46]:

$$\mu = 2.414 \times 10^{-5}\left(10^{247.8/(T-140)}\right)\ \mathrm{Pa.s} \tag{1}$$

where the temperature must be in Kelvin (K). The thermal conductivity of the silicon domain is also modeled as temperature-dependent with values obtained from the software

Engineering Equation Solver [47], which have been curved-fitted (R^2=0.99) with a third order polynomial with the form:

$$k_{\mathrm{Si}} = 2122.1 - 16.765\,T + 4.8183 \times 10^{-2}\,T^2 - 4.7442 \times 10^{-5}\,T^3 \qquad (2)$$

where the temperature must be in Kelvin (K), and the applicability range is from 280 to 373 K. The remaining thermophysical properties such as density, fluid thermal conductivity, and specific heat may be safely assumed to be constant with the values listed in Table 4.1 since their variation is less than 5% for the temperature range of interest in this application.

Table 4.1 – Properties of water/coolant and silicon/substrate.

Property	Symbol	Silicon	Water
Density (kg/m^3)	ρ_{Si}, ρ	2330	998
Thermal conductivity (W/m K)	k_{Si}, k	Eq. (2)	0.6
Specific heat (J/kg-K)	c, c_{p}	712	4182
Dynamic viscosity (Pa.s)	μ	--	Eq. (1)

4.1.2 Governing equations and boundary conditions

Based on the modeling assumptions, the resulting governing equations for the numerical solution of the mass and momentum conservation of fluid in the Cartesian coordinate system are:

$$\frac{\partial u}{\partial x} + \frac{\partial v}{\partial y} + \frac{\partial w}{\partial z} = 0 \qquad (3)$$

$$\rho\left(u\frac{\partial u}{\partial x}+v\frac{\partial u}{\partial y}+w\frac{\partial u}{\partial z}\right)=-\frac{\partial P}{\partial x}+\mu\nabla^2 u \tag{4}$$

$$\rho\left(u\frac{\partial v}{\partial x}+v\frac{\partial v}{\partial y}+w\frac{\partial v}{\partial z}\right)=-\frac{\partial P}{\partial y}+\mu\nabla^2 v \tag{5}$$

$$\rho\left(u\frac{\partial w}{\partial x}+v\frac{\partial w}{\partial y}+w\frac{\partial w}{\partial z}\right)=-\frac{\partial P}{\partial z}+\mu\nabla^2 w \tag{6}$$

The resulting energy conservation equation for the fluid domain is:

$$\rho c_{\mathrm{p}}\left(u\frac{\partial T}{\partial x}+v\frac{\partial T}{\partial y}+w\frac{\partial T}{\partial z}\right)=k\nabla^2 T \tag{7}$$

The heat diffusion equation for the solid domain (silicon) is:

$$\frac{\partial}{\partial x}\left(k_{\mathrm{Si}}\frac{\partial T}{\partial x}\right)+\frac{\partial}{\partial y}\left(k_{\mathrm{Si}}\frac{\partial T}{\partial y}\right)+\frac{\partial}{\partial z}\left(k_{\mathrm{Si}}\frac{\partial T}{\partial z}\right)=0 \tag{8}$$

Regarding boundary conditions, a constant flow rate is specified at the inlet section (normal to boundary) with a value of 190.66 mL/min (1585 kg/m^{2}s), which was chosen according to the available pump speeds used for the experimentation. The inlet fluid temperature for the model is specified at 21.3°C, from the controlled conditions of the experimental data set. The internal walls where the solid and fluid domains meet are set as interfaces with a no-slip boundary condition and continuity of heat flux and temperature. The outlet port is specified as a pressure outlet with a zero-gauge pressure, which is convenient to post-process the pressure drop across the different sections of the TDV. The four background zones and hotspot area indicated in Figure 3.3 are specified with a constant heat flux condition with values ranging from 250 to 750 W/cm^2. The remaining exterior walls are defined as adiabatic, under the assumption of negligible heat loss through these boundaries; the validity and applicability of the foregoing assumptions for accurate modeling is demonstrated in the upcoming results section.

4.1.3 Numerical procedure

The numerical solution of the conjugate heat transfer problem was obtained using the software ANSYS® FLUENT® 16.2 with the finite volume method. A second-order upwind scheme was used for discretizing both the momentum and energy equations with the least squares cell-based gradient method. The coupling of the pressure and velocity fields was achieved with the Semi-Implicit Method for Pressure Linked Equations (SIMPLE) algorithm. The numerical solution was assumed to have converged when the residuals for mass and momentum equations reached a value of 10^{-4}, while the energy equation reached a residual value of 10^{-7}.

Realizing that the solution of the momentum equation is the most resource-consuming and time-intensive part of the simulation, a convenient method for the analysis of multiple cases is to first find the adiabatic flow field solution to the problem for a given flow rate, and then use the converged solution for such case to initialize the conjugate heat transfer problem for the remaining cases with different heating conditions. Although the flow field will change since the viscosity is temperature dependent, the converged solution can be found after just a few iterations, making this technique quite expedient in analyzing a variety of powermaps (heterogeneous heat flux distribution) for a specified flow rate.

4.1.4 *Mesh independence analysis*

The computational domains used for the simulations are those indicated in Figures 3.1 and 3.2, where although the fluid domain is not shown, it is known to fill out the entire microgap. The meshing of the different designs was completed by using a hybrid method in which the fluid and solid domains are meshed with hexahedral and tetrahedral elements, respectively. A non-conformal meshing scheme is used to reduce the number of solid elements where the temperature gradients are considerably lower than those experienced in the fluid domain. Figure 4.1 depicts a zoomed-in picture with the meshing features for the fluid and solid regions; boundary layers (or inflation layers in general meshing) are defined at the fluid/solid interface with a total number of five layers with a growth rate (GR) factor of 1.2.

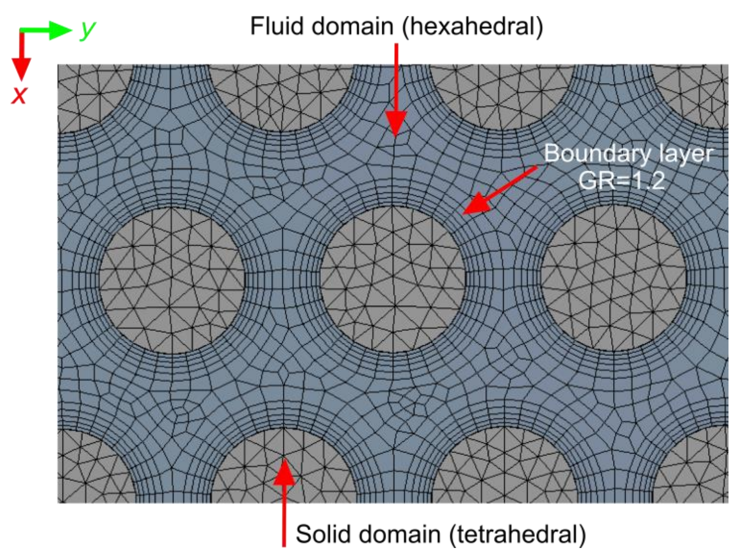

Figure 4.1 – Detail of the hybrid non-conformal mesh with medium refinement.

Despite the large number of geometric features (84 structural fins, ~2000 background fins, and ~500 hotspot fins) in a relatively small and low-profile cooling layer, the current capabilities of computing and the software ANSYS® Meshing made the detailed analysis of the entire TDV possible in order to capture important effects, such as the influence of the plenum shape, structural support fins, and variable pin fin clustering on the flow and temperature fields. By doing this, the model can be fully-validated with the experimental data for both TDV pin fin clustering arrangements and then be used to predict with confidence the behavior for virtually any type of a powermap. The parallel-meshing of an entire device under these settings was achieved in ~15 hours for ~12 million elements with four cores of an Intel® Xeon® processor, consuming ~25 GB of RAM memory.

Table 4.2 – Summary of the mesh independence study.

		Average temperature (K)										Press. drop (kPa)	
		Zone 1		Zone 2		Zone 3		Zone 4		Hotspot		Main fins	
Mesh	Cells	T_{wz1}	C_{wz1}	T_{wz2}	C_{wz2}	T_{wz3}	C_{wz3}	T_{wz4}	C_{wz4}	T_{HP}	C_{HP}	ΔP_{mf}	C_{mf}
1	11,480,671	315.98	6.2×10^{-3}	319.65	3.5×10^{-3}	324.42	4.9×10^{-3}	331.13	8.5×10^{-3}	316.53	2.5×10^{-3}	165.72	5.3×10^{-2}
2	13,996,473	313.92	2.5×10^{-3}	318.50	1.2×10^{-3}	322.81	1.7×10^{-3}	328.30	3.2×10^{-3}	315.75	9.5×10^{-5}	156.86	5.6×10^{-3}
3	16,031,251	313.12	--	318.12	--	322.27	--	327.25	--	315.72	--	155.97	--

In order to ensure a grid-independent solution, different mesh sizes were tested for fixed operating conditions. The spanwise clustering design (Figure 3.2) was chosen for this mesh sensibility analysis with a flowrate of 190.66 mL/min, inlet temperature of 20 °C (just for this part of the study), and a uniform heat flux of 250 W/cm^2 at each of the four zones and the hotspot area. Mesh independence was achieved by performing successive refinements, focusing on the fluid domain of the cooling pin fin array. Unlike conventional grid-independence studies, the number of elements was not doubled from one meshed model to another, but alternatively the mean element size was carefully reduced due to the large number of fins in this domain. The cost-effective mesh density that offered a grid-independent solution was found after a number of meshes were tested, and the criterion $C_i = \left| (N^j - N^{j+1}) / N^j \right| < 5\times10^{-3}$ was satisfied, where N^j is the computed value for the field variable of comparison and N^{j+1} is the value obtained with the next refined mesh. The pressure drop across the main fin array and average temperature at each zone were chosen as the variables of comparison. Table 4.2 lists a summary of the grid-independence study for three selected meshes. Based on these results, the settings of Mesh 2 were used to balance the solution accuracy and computational time.

4.2 Results

Recalling that one of the main objectives of the present thesis is the assessment of variable pin fin clustering microgaps through detailed modeling for a variety of scenarios, the following results sections are devoted to discussing the comprehensive assessment of experimental data with CFD-HT simulations. Then, the flow and thermal behavior for each of the analyzed TDVs is compared, so the implications and trade-offs of the proposed concepts can be identified for the effective design of cooling layers for actual 3D-IC architectures. Finally, the details and guidelines for a reduced-domain simulation are given so they can be easily reproduced by other investigators, and used as a point of validation for their numerical models.

4.2.1 Model validation with TDV benchmark experiments

While the concept of vertically integrated microelectronics has been intensively studied in the past years and significant advances have been achieved, there is still a lack of detailed experimental data for microgap cooling layers with pin fins, especially for the case of heterogeneous heating and variable pin fin clustering. Clear examples of these previous limitations are the numerical studies of variable fin density layers in [20] and [21], where the model validation used the experimental average thermal resistances reported in [9], which are actually for microchannels, where the temperature profile is mostly linear and can even predicted by 1D models under thermally and hydrodynamically fully developed conditions. For the case of a micro pin fin array, the boundary layer re-develops at each pin front, and hence may provide enhanced heat transfer characteristics when compared with microchannels. The thermal and flow behavior of such geometries requires CFD-HT simulations, supported by a reliable set of experimental data for the same layouts and operating conditions; the latter aspects are key contributions from the present thesis.

Figures 4.2 and 4.3 present the summary of the thermal profiles and validation plots for the local and spanwise clustering designs, respectively. The plotted curves show the model-predicted temperature variations across a centerline in the flow direction which passes through the hotspot area, where the values are plotted for the 10 mm length of the active heated area indicated in Figure 3.4. A highly non-linear temperature variation is noted, especially across the hotspot area, with very interesting behaviors as the hotspot heat flux is varied. Since the platinum RTD heaters return an average electrical resistance value, which is then translated to a temperature for each zone during the tests, the square dots represent the experimental average wall temperature values. The circular dots represent the area-averaged temperature values from the corresponding model results. The model predictions and experimental temperature values are in a very good agreement, with the difference between the two of the zone-averaged absolute temperature ranging from 0.02 to 0.5% for the background zones, and from 0.06 to 0.48% for the hotspot area.

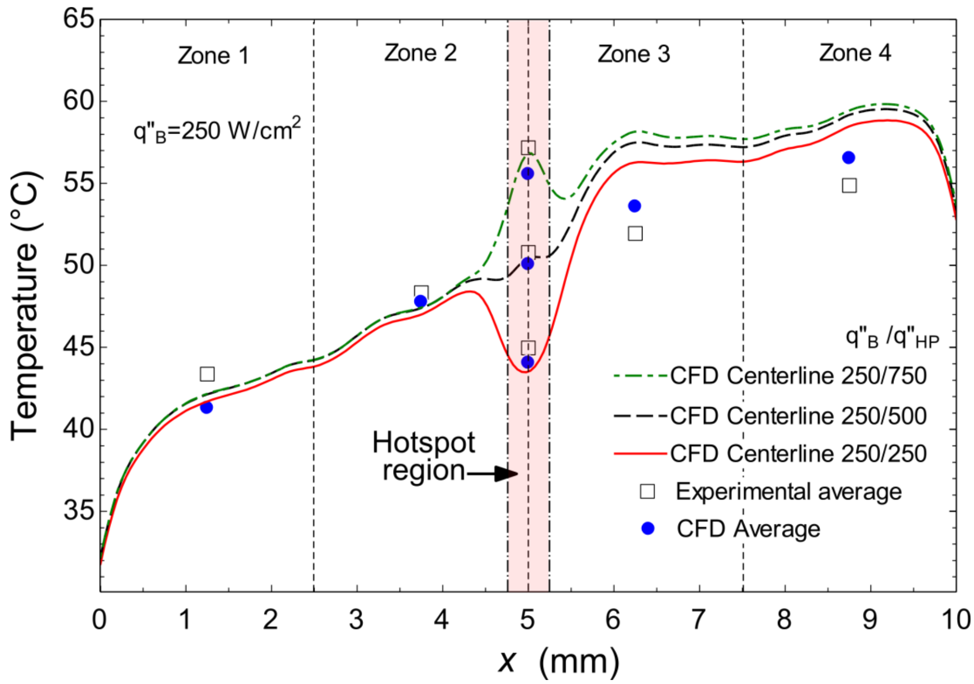

Figure 4.2 – Validation of the CFD-HT model with experimental data for the TDV with local clustering design for a background heat flux of q''_B = 250 W/cm^2, hotspot heat fluxes from q''_{HP} = 250 – 750 W/cm^2, and flow rate of 190.66 mL/min.

Considering the large temperature gradients across the hotspot, whose behavior is dictated by the entire TDV layout, the prediction capabilities of the present model are noteworthy. For the first analyzed case in which the background and hotspot zones have the same heat flux values at 250 W/cm^2, there is a significant temperature drop in the hotspot due to local increase of heat transfer area, which serves the main objective of offsetting the hotspot temperature at this heat flux. As the hotspot heat flux is increased by 2x and 3x of the background values, there is a local temperature increase proportional to its magnitude. Despite the relatively high hotspot heat flux at 750 W/cm^2, both of the TDV designs are capable to maintain its average temperature below 60 °C, demonstrating the effectiveness and potential of the variable pin fin clustering concept for the practical stacking of microelectronics with high power dissipation.

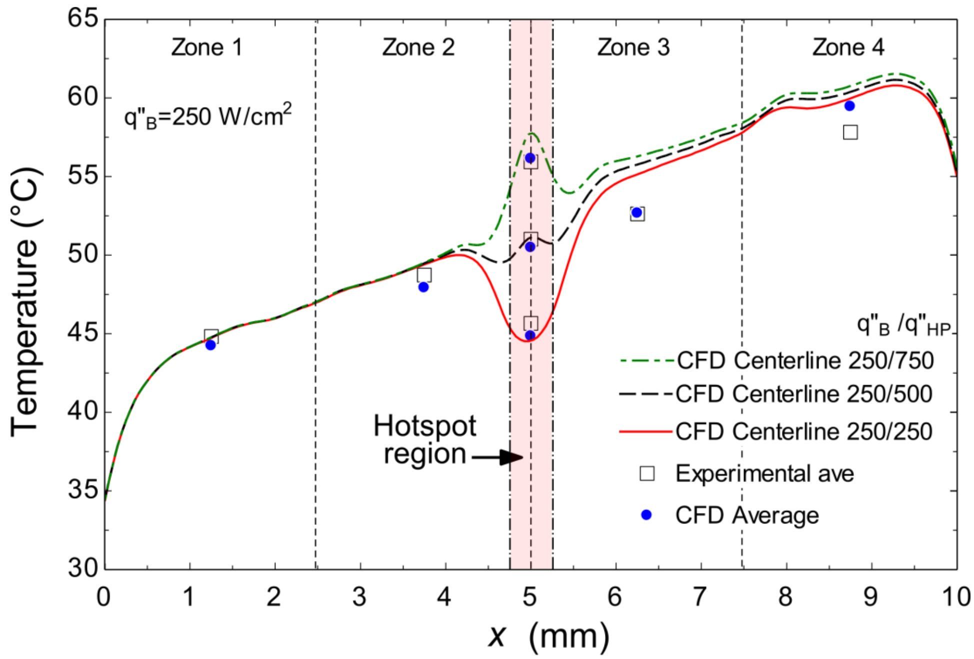

Figure 4.3 – Validation of the CFD-HT model with experimental data for the TDV with spanwise clustering design for a background heat flux of q''_B = 250 W/cm^2, hotspot heat fluxes from q''_{HP} = 250 – 750 W/cm^2, and flow rate of 190.66 mL/min.

The pressure drop across the main fin array was also compared between the experimental measurements and the model predictions. The results from both the numerical and the experimental methods are within a difference below 2.3%. Considering the complex flow field that is strongly influenced by the structural pin fins at each plenum, the background cooling fin array and the variable clustering density near the hotspot, this agreement is considered excellent.

Table 4.3 – Summary of the model validation with relevant experimental data.

			Zone temperature rise above inlet fluid temperature				q''_{HP}=250 W/cm^2	q''_{HP}=500 W/cm^2	q''_{HP}=750 W/cm^2	
TDV design	Result type	ΔT_f (°C)	ΔT_{wz1} (°C)	ΔT_{wz2} (°C)	ΔT_{wz3} (°C)	ΔT_{wz4} (°C)	ΔT_{HP} (°C)	ΔT_{HP} (°C)	ΔT_{HP} (°C)	ΔP (kPa)
Local	Exp.	18.40	23.76	28.71	32.33	35.26	25.36	31.17	37.56	119.8
	Model	18.86	21.7	28.18	33.99	36.93	24.47	30.48	35.97	122.1
Spanwise	Exp.	18.40	23.52	27.42	31.31	36.52	24.35	29.72	34.64	141.6
	Model	18.85	22.95	26.64	31.38	38.16	23.55	29.19	34.86	147.1

Table 4.3 lists a summary of the relevant average values for this model validation, where the reported values correspond to the surface temperature rise above the inlet fluid temperature. It is important to point out that the effect of varying the hotspot heat flux on the average temperatures of zones 1 to 4, fluid temperature rise, and pressure drop is negligible (< 0.1%) for a fixed background heat flux and flow rate, and hence these values are not included in Table 4.3, nor Figures 4.2 and 4.3 for practical purposes.

4.2.2 Flow distribution effects and thermal implications

One of the great advantages of the present CFD-HT model is the level of detail at which the simulation results can be post-processed, and the insight that can be obtained from such, which is not accessible from experiments. As mentioned, the resulting flow field is relatively complex due to the presence of several pin fin structures in a variable layout, where the full details could not be obtained even with the most advanced experimental techniques. Hence, the simulation results are very helpful in understanding the hydrodynamic behavior, which is of main interest for optimization studies.

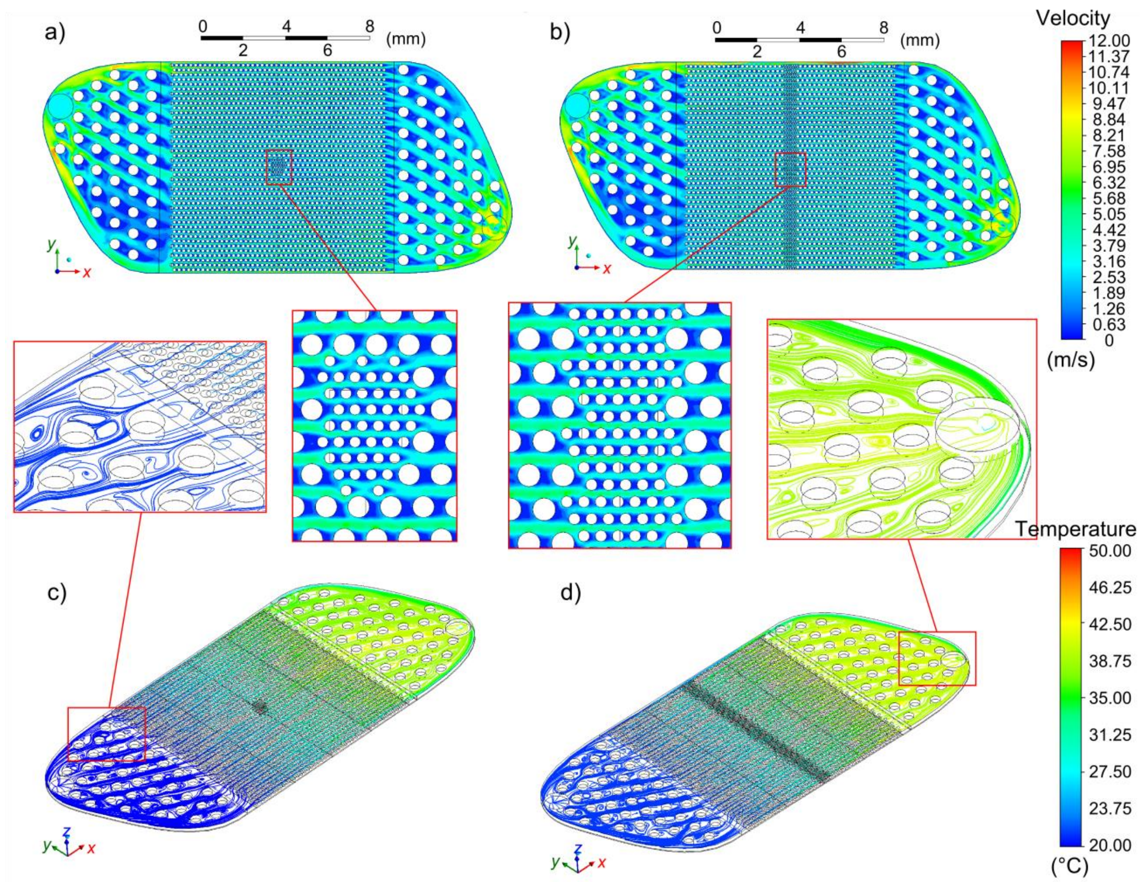

Figure 4.4 – Flow field results for the simulated TDV designs at 190.66 mL/min. Velocity contours (m/s) on a mid-section plane for: a) local clustering, b) spanwise clustering. Streamlines colored by fluid temperature (°C) for: a) local clustering, b) spanwise clustering.

Figure 4.4 presents the main flow field model results for both TDV designs for a flow rate of 190.66 mL/min and uniform heating at 250 W/cm^2, where useful information and details regarding the flow distribution behavior can be observed in the velocity contours at a mid-section plane shown in Figures 4.4a and 4.4b. An important aspect to be noted is that the flow distribution is non-uniform across the entire device due to the plenum shape and strong influence of the structural pin fins, where the preferred flow lanes may be identified in the main diagonals connecting the inlet and outlet ports. Despite these flow distribution effects, a useful advantage of using microgaps with pin fins in single-phase cooling is that the flow may interact in the transversal direction (y) and therefore the main fin array helps in straightening the flow as it moves downstream; a clear advantage over microchannels arrays.

The zoom-in windows of Figures 4.4a and 4.4b reveal important flow features for both designs in one of the areas of main interest, which is the hotspot. For the local clustering design, it may be observed that there are flow bypass effects due to the variable flow resistance in the transversal direction (i.e., the locally higher pressure drop across the hotspot is offset by lower mean flow velocities across the parallel lanes). Since such effects were expected during the conceptual stage of the investigation, the alternative spanwise design was proposed in order to homogenize the local flow resistance in the transversal direction, at the expense of a higher overall pressure drop. Figure 4.4b provides confirmation of these effects, where the quantified mean flow velocities across the hotspot array are 3.47 and 4.12 m/s for the local and spanwise clustering designs, respectively; such increase in velocities also results in an increase in the local heat transfer coefficient. Some other useful predictive capabilities of the present model are depicted in Figs. 4.4c and 4.4d, in the form of the streamlines from inlet to outlet colored by fluid temperature. The zoom-in windows indicate the presence of recirculation regions in the wake zone of the structural pin fins in the inlet and exit plena, which although not the best for hydrodynamic performance, still allow a balance between flow circulation and structural reliability of the design.

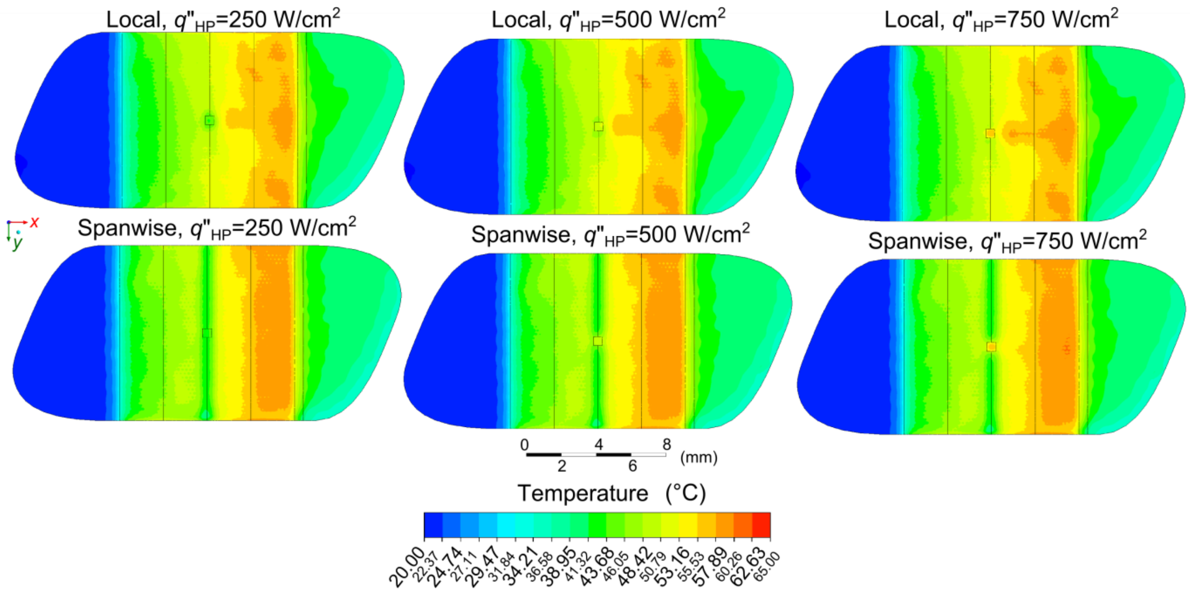

Figure 4.5 – Temperature field results for the simulated TDV designs at 190.66 mL/min, background heat flux of q''_B = 250 W/cm^2 and different hotspot heat fluxes.

The previously discussed hydrodynamic features have an important influence on the resulting temperature fields, and it is of main interest to analyze the temperature distribution on the heater surfaces of the TDVs, as this represent closely what the temperature of the integrated circuits would be in actual operation. It is more insightful to look at the continuous temperature distribution predicted by the full 3D model than the discrete values from experimentation, only when the former has been validated. Figure 4.5 presents the temperature contours at the TDV bottom surface (where the heating is applied) for the different heat flux combinations and layouts of the present investigation. It can be noted that the temperature distributions are reasonably symmetric due to the beneficial effects of transversal flow interaction offered by the main cylindrical pin fin array. The results of most interest are those regarding the combined performance of each TDV. For the spanwise clustering design, it can be observed that there is a temperature drop for each case across the strip of highest fin density, where the local temperatures of the hotspot increase according to the magnitude of the applied heat flux. In contrast, the excess temperature control for the local clustering design is only targeted to the hotspot and it is important to point out that a tradeoff exists between the local heat transfer coefficient (effects of flow bypass) and the total pressure drop across the main fin array.

It is important to point out that one of the main objectives in this chapter was to assess the previously explained effects in order to decide which configuration would offer the most balanced performance in terms of local hotspot temperatures and pressure drop. Both the experimental evidence and the numerical predictions indicate that the effect of flow bypass is not as significant to justify the increase in pressure drop associated with the use of the spanwise design; the hotspot temperature values are very similar for both TDVs. In quantification of the aforementioned statement, the results indicated that under the same flow rate and background heat flux, the hotspot temperature rise/pressure drop of the TDVs were 37.56 °C / 119.8 kPa and 34.64 °C / 141.6 kPa for the local and spanwise clustering designs, respectively. Such metrics reveal an important conclusion: the cooling layer may be properly designed by locally increasing the heat transfer area just in the vicinity of the hotspot, which is of major relevance for the design of combined thermal control of a variety powermaps with large heat flux gradients. Besides such results, the reduction in flow restriction (or overall pressure drop) for the local clustering design also means that for a given pump in a practical system, the flow rate would be higher and therefore lower temperatures should be expected with this design.

4.3 Reduced simulation domain as a reference for validating numerical models

In order to provide a point of reference to future numerical studies interested in the concept of variable pin fin clustering for heterogeneous heat flux conditions, a reduced domain was created and simulated with the same model, meshing settings, and operating conditions as those described in Section 4.1. The objective of reducing the domain is to facilitate the repeatability of results by decreasing the number of elements at the expense of not capturing the entire physics of the problem; this should allow the researcher to faster reproduce the results reported here as the start point in a new numerical simulation or design based on the similar concept.

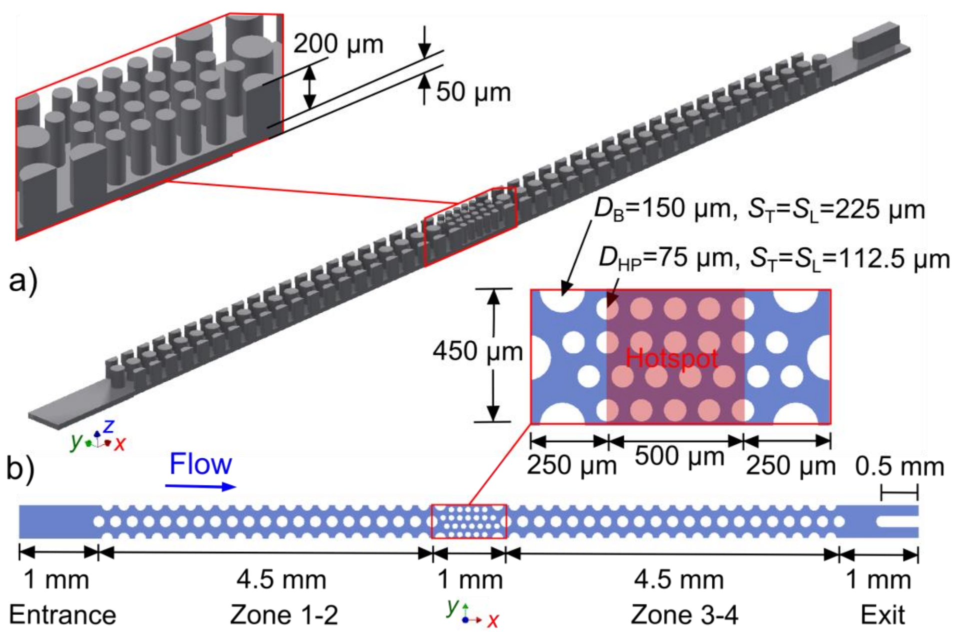

Figure 4.6 – Geometric features and dimensions of the reduced domain for numerical model validation: a) isometric view of the solid domain, b) top view of the fluid domain.

The simplified computational domain is depicted in Figure 4.6, where all of the geometrical details and required dimensions for replication are indicated; just a strip of the main fin array is considered with the cylindrical background and hotspot cooling fins in the same inline array and longitudinal and transversal pitches ($S_T = S_L$) of the analyzed TDVs. As indicated in Figure 4.6, the domain has a width of 450 μm, and a total length of 12 mm with a 1 mm long entrance region to allow the flow to develop and a 1 mm long exit region with an elongated fin to split the flow and help the solution convergence. The total length of the heated section is 10 mm with the hotspot at the middle and a length of 500 μm. The zoom-in window of Figure 4.6b gives the required geometric details and dimensions for pin fin clustering at this zone. Regarding boundary conditions, since the heat flux is fixed in background zones at 250 W/cm^2, zones 1-2 (and 3-4) have been merged in order to report their average temperature for the sake of simplicity. Symmetry boundary conditions were specified at each of the domain sides. It is important to point out that such reduced problem formulation is not capable to account for important effects such as the flow bypass, upstream flow distribution, or flow interactions through the entire fin array. However, a reasonable approximation may be obtained for the case of the spanwise clustering design (no flow bypass) with the domain in Figure 4.6. The inlet section was specified with a flow rate of 8.58 mL/min at an inlet temperature of 21.3 °C, which comes from the assumption that the total flowrate (190.66 mL/min) is equally distributed at each section of the device.

The main simulation results for the described conditions are presented in the form of temperature and velocity contours in Figures 4.7a and 4.7b, respectively. The zoom-in windows in Figure 4.7a give a detail of the local temperature distribution in the hotspot for different heat fluxes, where the qualitative behavior is similar to that predicted by the full TDV simulation for the spanwise clustering design. The velocity contours at a mid-section plane are depicted in Figure 4.7b, where the zoom-in windows give the details of the streamlines colored by velocity and the re-circulation regions for the flow past the cylindrical structures.

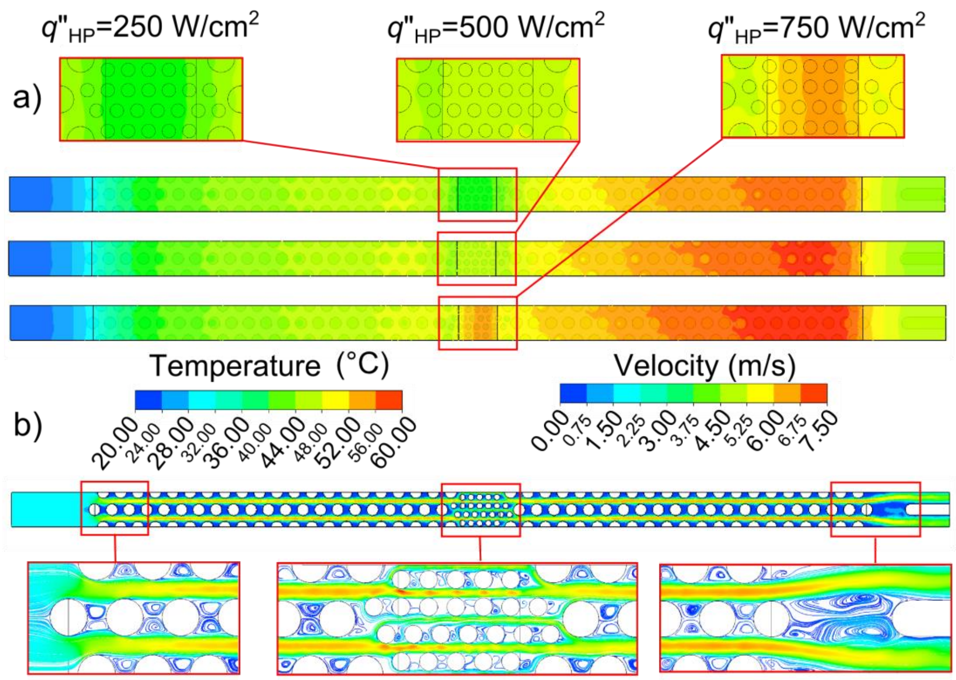

Figure 4.7 – Simulation results for the reduced domain at a background heat flux of q''_B = 250 W/cm^2 with different hotspot heat fluxes, and a flow rate of 8.58 mL/min: a) temperature distribution, b) velocity contours at a mid-section plane.

The axial temperature variation for the discussed cases is plotted in Figure 4.8, where a similar behavior to that of the full spanwise clustering design of Figure 4.3 is noted for the different hotspot heat fluxes. However, some differences may be observed such as the upstream temperature variation, and the magnitude of the peak temperatures at the hotspot, which are related to the use of symmetry boundary conditions and uniform flow assumption, respectively. Nevertheless, the curves and values of Figure 4.8 are intended for validation purposes in future numerical studies, since they provide a robust approximation to the complex temperature variations and hydrodynamic characteristics for the concept of variable pin fin clustering, which are demonstrated by experimental data and supported by the employed CFD-HT model.

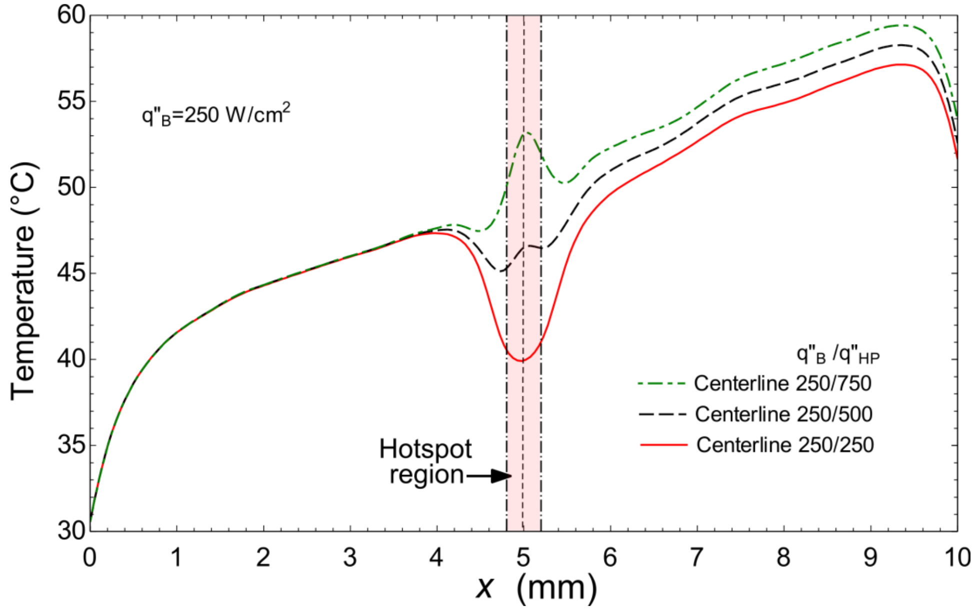

Figure 4.8 – Axial temperature variation for the reduced domain simulations with a background heat flux of q''_B = 250 W/cm^2, hotspot heat fluxes from q''_{HP} = 250 – 750 W/cm^2, and flow rate of 8.58 mL/min.

Besides reproducing the curves of Figure 4.8, the average temperature values, fluid temperature rise, and pressure drop may also be compared with those reported for each case in Table 4.4.

Table 4.4 – Reduced domain simulation results for different hotspot heat fluxes and q''_B = 250 W/cm^2.

q''_{HP} (W/cm^2)	ΔT_f (°C)	$T_{wz1\text{-}2}$ (°C)	$T_{wz3\text{-}4}$ (°C)	T_{HP} (°C)	ΔP (kPa)
250	18.77	42.94	52.42	40.45	140.14
500	19.70	43.38	53.90	46.74	138.23
750	20.65	43.80	55.37	53.09	137.28

It is to be noted that the hotspot average temperatures are slightly under predicted when compared to the experimental and full model results due to the aforementioned assumptions and limitations, but they may be confidently used for validation purposes since the computational model and numerical procedure techniques remain the same as those used for the full TDV assessment.

4.4 Remarks and conclusions

The experimental and numerical results discussed in the present chapter have demonstrated the advantages of using the concept of variable pin fin clustering for the combined thermal control of heterogeneous heating conditions. A single, combined cooling layer with variable sizes and layouts of structural, background, and hotspot cooling fin array was shown to facilitate multi-tier thermal management of the practical 3D-stacking of ICs with one-inlet and one-outlet microfluidic ports for coolant delivery. The most relevant results from the present study indicated that a microgap with pin fins allows the transversal flow interaction, which led to beneficial effects such as the downstream flow straightening and reasonably symmetric temperature distributions. The objective comparison between the proposed designs for local and spanwise clustering near the hotspot indicated a relatively high increase in pressure drop for the latter with only a slight improvement in the local heat transfer at the hotspot. This led to the important conclusion that the effect of flow bypass is negligible and therefore the local surface area may be increased just in the vicinity of the hotspot, allowing keeping reduced pressure drops and yet improving locally the heat transfer performance; an important finding for the design of combined cooling layers for actual IC architectures with large heat flux gradients.

The selected range of experimental data for this study was used to validate a detailed, physics-based CFD-HT model that was capable of predicting and providing fundamental insights into the problem, such as the detailed 3D temperature distributions and flow field in the entire TDVs. Due to the scant current literature on this topic, and the relevance of these type results, a reduced domain for simulation was proposed in order to aid future numerical studies focused on performance optimization and proposing different types of cooling layouts employing the concepts of this thesis.

As a logical sequence in the development of this dissertation, at this point it can be mentioned that the challenges outlined in Section 2.1.1 for single-phase cooling have been addressed. The rest of this dissertation will focus on the relatively unexplored and significantly more complex area of two-phase cooling in microsystems, and as such, it is to be noted here that going from the full-scale simulations and experiments shown in this chapter for single-phase is not easily scalable for the case of flow boiling. Therefore, a gradual approach was taken in order to achieve the ultimate goal of being the first investigation of its type to demonstrate both numerically and experimentally the two-phase cooling characteristics in silicon microgaps with a variable fin density and hotspots.

CHAPTER 5. COMPUTATIONAL FLUID DYNAMICS MODELING OF FLOW BOILING: AN INITIAL APPROACH IN MICROCHANNELS WITH NON-UNIFORM HEAT FLUX

The first endeavors toward developing a CFD-HT model for two-phase cooling purposes are presented in this chapter. As it was pointed out in the introduction section, there are not studies reporting the three-dimensional flow boiling characteristics through numerical modeling applicable to the cases of interest; such fact is attributed to the intricacies of the problem. A good methodology when facing new, challenging problems is to start simple; there was no immediate way in which the experimental two-phase cooling data of the described TDVs could be directly contrasted with numerical simulations because of its complexity and computational requirements. Therefore, the initial development of the two-phase modeling framework is discussed in this chapter by presenting an approach for the analysis of flow boiling in microscale using a three-dimensional (3D) Volume of Fluid (VOF) model coupled with a phase-change model accounting for the interfacial mass and energy transfer. This type of modeling allows the transient analysis of flow boiling mechanisms while providing the ability to visualize in detail temperature, phase, and pressure distributions for microscale applications with affordable computational resources (i.e. , ran on a workstation for relatively small computational domains). For this initial study, the microscale flow boiling phenomena was modeled in a single microchannel for the sake of speed and ease of model adjustment/refinement, with the main objective of acquiring the necessary skills and know-how for its implementation in the ultimate application of relevance to this thesis

(TDVs). The results for a plain microchannel are validated against benchmark correlations for heat transfer coefficients and pressure drop as a function of the heat flux and mass flux. Furthermore, the model is used for the assessment of two-phase cooling in microelectronics under a realistic scenario with non-uniform heat fluxes at localized regions of a silicon microchannel, relevant to the cooling layer of 3D integrated circuit (IC) architectures. Results indicate the strong effect of two-phase flow regime evolution and vapor accumulation on heat transfer; the effects of reduced saturation pressure, subcooling and flow arrangement are explored in order to provide insight into the underlying physics and cooling performance, before jumping to significantly more complex cases.

5.1 Volume of Fluid (VOF) model

The Volume of Fluid (VOF) model is used for the interface-tracking of two or more immiscible fluids, in which a single set of momentum equations is shared by all of the fluids, and the volume fraction of each phase in every cell element is solved and tracked throughout the domain [48]. For two-phase flow, the continuity equations for the liquid and vapor phases are:

$$\frac{\partial}{\partial t}(\alpha_l \rho_l) + \nabla \cdot (\alpha_l \rho_l \vec{v}) = S_l \tag{9}$$

$$\frac{\partial}{\partial t}(\alpha_\mathrm{v} \rho_\mathrm{v}) + \nabla \cdot (\alpha_\mathrm{v} \rho_\mathrm{v} \vec{v}) = S_\mathrm{v} \tag{10}$$

where the source terms S_l and S_v are the volumetric mass transfer rates between phases and its calculation will be discussed in the Phase-change model section. The sum of the volume fraction of each of the involved phases must equal unity in each computational cell.

In the VOF model, a single set of momentum conservation equations is solved for the involved phases and has the following form:

$$\frac{\partial}{\partial t}(\rho\vec{v}) + \nabla\cdot(\rho\vec{v}\vec{v}) = -\nabla P + \nabla\cdot[\mu(\nabla\vec{v} + \nabla\vec{v}^{\mathrm{T}})] + \rho\vec{g} + \vec{F} \tag{11}$$

where ρ and μ are the mixture density and viscosity, respectively, and are computed as a function of the volume fraction of each phase with:

$$\rho = \alpha_l\rho_l + \alpha_{\mathrm{v}}\rho_{\mathrm{v}} \tag{12}$$

$$\mu = \alpha_l\mu_l + \alpha_{\mathrm{v}}\mu_{\mathrm{v}} \tag{13}$$

The energy conservation equation is coupled to the model; it is also shared among the phases and has the following form:

$$\frac{\partial}{\partial t}(\rho E) + \nabla\cdot[\vec{v}(\rho E + P)] = \nabla\cdot(k\nabla T) + S_{\mathrm{e}} \tag{14}$$

where the energy E is treated as a mass-averaged variable:

$$E = \frac{\alpha_l\rho_l E_l + \alpha_{\mathrm{v}}\rho_{\mathrm{v}}E_{\mathrm{v}}}{\alpha_l\rho_l + \alpha_{\mathrm{v}}\rho_{\mathrm{v}}} \tag{15}$$

The energy for each phase is computed with the corresponding specific heat and the shared temperature, and the mixture thermal conductivity k is defined in the same way as Eqs. (12) and (13).

Gravitational effects are considered as an implicit body force in the force momentum balance equation. The incorporation of surface tension, which is known to have a strong effect in the two-phase flow in small passages, is implemented through the Continuum Surface Force (CSF) model by Brackbill et al. [49]. In such model, the pressure drop across the interface is obtained as a function of the surface tension coefficient, and the surface curvature measured by the two radii in orthogonal directions:

$$\Delta P = \sigma\left(\frac{1}{R_1} - \frac{1}{R_2}\right) \tag{16}$$

In the CSF model, the surface curvature is obtained with phase composition gradients, where the surface normal is defined as the gradient of the secondary phase (vapor) volume fraction:

$$\overrightarrow{n_\mathrm{v}} = \nabla \alpha_\mathrm{v} \tag{17}$$

The interface curvature is computed as the divergence of the interface unit normal:

$$\kappa_\mathrm{v} = \nabla \cdot \hat{n}_\mathrm{v} = \nabla \cdot \frac{\overrightarrow{n_\mathrm{v}}}{|\overrightarrow{n_\mathrm{v}}|} \tag{18}$$

The surface tension force may be converted into a volumetric force upon the use of the divergence theorem, resulting in the source term that is included in the momentum equation to account for surface tension effects:

$$\vec{F} = \sigma \frac{\rho \kappa_{\mathrm{v}} \nabla \alpha_{\mathrm{v}}}{\frac{1}{2}(\rho_l + \rho_{\mathrm{v}})} \tag{19}$$

where the term $\rho / \big((\rho_l + \rho_v)/2\big)$ is used in order to refine the capability of the CSF model for high-density ratio interfaces (e.g., liquid water and its vapor); this method is referred as "*density scaling of the CSF*", and helps to keep a constant interface thickness for tracking [49].

The contact angle between the phases and the wall is used to compute the curvature of this phase near the solid domain, which allows the inclusion of surface wettability effects. The surface normal in adjacent cells to the wall is calculated as:

$$\hat{n} = \hat{n}_{\mathrm{w}} \cos \theta_{\mathrm{w}} + \hat{t}_{\mathrm{w}} \sin \theta_{\mathrm{w}} \tag{20}$$

where $\hat{n}_w$ and $\hat{t}_w$ are the unit vectors normal and tangential to the wall, respectively. The interface reconstruction is done based on the Piecewise-Linear-Interface-Calculation (PLIC) algorithm developed by Youngs [50], where the interface between two fluids is represented as a linear slope within each element for the calculation of the advection of fluid through the cell faces. This allows the reconstruction of sharper interfaces when compared with other schemes such as the Donor-Acceptor [48] and Compressive Interface Capturing Scheme for Arbitrary Meshes (CICSAM) [51].

5.2 Phase-change model

The present section is devoted to describing the formulation and implementation of the phase-change model, and the calculation of the source terms that account for the net mass transfer in Equations (9) and (10).

Starting the formulation from the kinetic theory of gases, the phase-change mass flux over a liquid-vapor interface using the so-called Hertz-Knudsen equation is:

$$m_{\mathrm{v}}^{"} = \frac{2\sigma_{\mathrm{e}}}{2-\sigma_{\mathrm{e}}}\left(\frac{M}{2\pi R_{\mathrm{u}} T_{\mathrm{sat}}}\right)^{1/2} (P_{\mathrm{v}} - P_{\mathrm{sat}}) \tag{21}$$

where P_{v} is the partial pressure of vapor at the interface, and σ_{e} is the accommodation coefficient for evaporation [28], which represents the portion of vapor molecules adsorbed by the liquid surface. Maa [52] and Cammmenga et al. [53] suggested a value of $\sigma_{\mathrm{e}} = 1$ based on experimental measurements. The condensation and evaporation accommodation coefficients are usually assumed to be equal ($\sigma_{\mathrm{e}} = \sigma_{\mathrm{c}}$), as would be required by thermostatic equilibrium conditions [28].

The equilibrium condition between the liquid and vapor phases requires their chemical potentials to be equal, and for the process of phase change at the saturation condition, the well-known Clausius-Clapeyron relation may be used to relate the pressure and temperature through the following expression:

$$\left(\frac{dP}{dT}\right)_{\mathrm{sat}} = \frac{h_{\mathrm{lv}}}{T_{\mathrm{sat}}(1/\rho_{\mathrm{v}} - 1/\rho_{\mathrm{l}})} \tag{22}$$

Near the saturation condition, the following expression may be obtained by integration:

$$(P_{\mathrm{v}} - P_{\mathrm{sat}}) = -\frac{h_{\mathrm{lv}}}{T_{\mathrm{sat}}(1/\rho_{\mathrm{v}} - 1/\rho_{\mathrm{l}})}(T_{\mathrm{v}} - T_{\mathrm{sat}}) \tag{23}$$

Combining Equations (21) and (23), the phase-change mass flux is obtained as:

$$m_{\mathrm{v}}^{"} = \frac{2\sigma_{\mathrm{e}}}{2 - \sigma_{\mathrm{e}}}\left(\frac{M}{2\pi R_{\mathrm{u}} T_{\mathrm{sat}}}\right)^{1/2} h_{l\mathrm{v}}\left(\frac{\rho_{\mathrm{v}}\rho_l}{\rho_l - \rho_{\mathrm{v}}}\right)\left(\frac{T - T_{\mathrm{sat}}}{T_{\mathrm{sat}}}\right) \tag{24}$$

The mass transfer source term for the vapor mass conservation equation may be obtained by multiplying the phase-change mass flux by the interfacial area density, which may be defined with the following expression:

$$\frac{A_{\mathrm{I}}}{V_{\mathrm{cell}}} = \frac{6\alpha_{\mathrm{v}}}{d} \tag{25}$$

The resulting source terms that account for the volumetric phase-change rate have the form:

$$S_i = \frac{6}{d}\left(\frac{2\sigma_{\mathrm{e}}}{2 - \sigma_{\mathrm{e}}}\right)\left(\frac{M}{2\pi R_{\mathrm{u}} T_{\mathrm{sat}}}\right)^{1/2} h_{l\mathrm{v}}\left(\frac{\rho_{\mathrm{v}}\rho_l}{\rho_l - \rho_{\mathrm{v}}}\right)\alpha_i\left(\frac{T - T_{\mathrm{sat}}}{T_{\mathrm{sat}}}\right) \tag{26}$$

where the subscript i denotes the corresponding phase. During the phase-change process, energy is also transported with mass and therefore the adequate source term S_{e} should be accounted for in the energy equation. The resulting heat transfer rate may be determined by multiplying the latent enthalpy of vaporization by the mass transfer rate of vaporization or condensation as:

$$S_{\mathrm{e}} = h_{l\mathrm{v}} S_i \tag{27}$$

According to the phase-change model by Lee [37], the expression for the volumetric phase-change rate given by Eq. (18) may be simplified upon the definition of relaxation parameters λ_i, which specify the rate of mass transfer between phases. Table 5.1 lists a summary of the set of reduced relations and criteria for the implemented phase-change model. For the present investigation, the values of λ_i for the boiling of water have a value of 0.1 s^{-1}, similar to the values employed in the investigations by Lee [37] and De Schepper et al. [38]. Bubble nucleation will occur at computational cells on the heated wall when the temperature criterion for vaporization given in Table 5.1 is satisfied.

Table 5.1 – Summary of the source terms included for the phase-change model*.

If $T_l > T_{\mathrm{sat}}$ (Vaporization)		If $T_{\mathrm{v}} < T_{\mathrm{sat}}$ (Condensation)	
$S_l = -\lambda_l \alpha_l \rho_l \dfrac{T_l - T_{\mathrm{sat}}}{T_{\mathrm{sat}}}$	(28)	$S_l = \lambda_{\mathrm{v}} \alpha_{\mathrm{v}} \rho_{\mathrm{v}} \dfrac{T_{\mathrm{sat}} - T_{\mathrm{v}}}{T_{\mathrm{sat}}}$	(29)
$S_{\mathrm{v}} = \lambda_l \alpha_l \rho_l \dfrac{T_l - T_{\mathrm{sat}}}{T_{\mathrm{sat}}}$	(30)	$S_{\mathrm{v}} = -\lambda_{\mathrm{v}} \alpha_{\mathrm{v}} \rho_{\mathrm{v}} \dfrac{T_{\mathrm{sat}} - T_{\mathrm{v}}}{T_{\mathrm{sat}}}$	(31)

*Equivalent to Eq. (18) with:

$$\lambda_l = \frac{6}{d}\left(\frac{2\sigma_{\mathrm{e}}}{2-\sigma_{\mathrm{e}}}\right)\left(\frac{M}{2\pi R_{\mathrm{u}} T_{\mathrm{sat}}}\right)^{1/2} h_{l\mathrm{v}}\left(\frac{\rho_{\mathrm{v}}}{\rho_l - \rho_{\mathrm{v}}}\right) \;\; ; \;\; \lambda_v = \frac{6}{d}\left(\frac{2\sigma_{\mathrm{e}}}{2-\sigma_{\mathrm{e}}}\right)\left(\frac{M}{2\pi R_{\mathrm{u}} T_{\mathrm{sat}}}\right)^{1/2} h_{l\mathrm{v}}\left(\frac{\rho_l}{\rho_l - \rho_{\mathrm{v}}}\right)$$

It is important to note that one of the main limitations for CFD modeling of boiling processes is the prediction of active nucleation sites (which are known to randomly vary in space and time, and occur at wall crevices with entrapped vapor); however, this behavior can be mimicked with the discussed approach and results in reasonable agreement with experimental observations can be obtained as will be discussed in foregoing sections.

5.3 Computational domain

As mentioned in the beginning of the chapter, due to the complexity and transient nature of microscale flow boiling, it was decided to start the model development and adjustment by using simple computational domains, comparing results against available data in the literature, and then raise the bar with more challenging problems until reaching the ultimate described goals for the TDVs. A straight microchannel formed by zero-thickness walls was first analyzed in order to compare the model results with an experimental correlation for flow boiling in small flow passages.

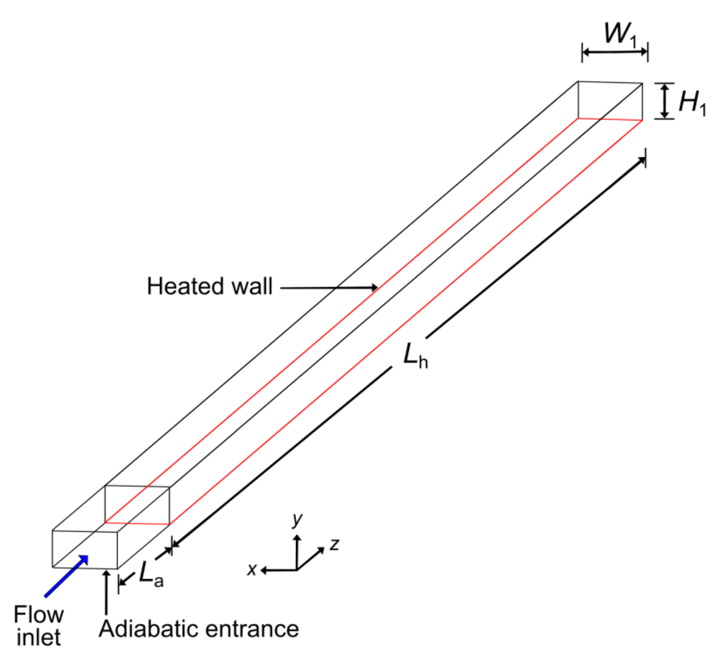

Figure 5.1 – Computational domain used for comparison with a boiling correlation.

The mesh independence analysis was also carried out with this first computational domain in order to find the appropriate mesh size to capture the two-phase flow phenomena. The described plain microchannel has a rectangular cross-section of 300 μm width (W_1) and a height (H_1) of 150 μm, with an adiabatic entrance of length L_a= 0.5 mm and a heated length of L_h= 4.5 mm, as indicated in Figure 5.1.

The second computational domain represents a single silicon microchannel representative the cooling interlayer of a 3D IC chip stack. The dimensions used for this channel correspond to those used in the study of Kim et al. [32] for the baseline case with a channel depth of 100 μm (H_2), width (W_2) of 200 μm, side wall thickness (t_w) of 50 μm, and base thickness (t_b) of 50 μm. The channel length (L_2) is 6 mm, which has been divided into 24 modules (M) for the input of variable heat fluxes corresponding to selected sections from the powermap of a dual-core processor code-named Penryn [54].

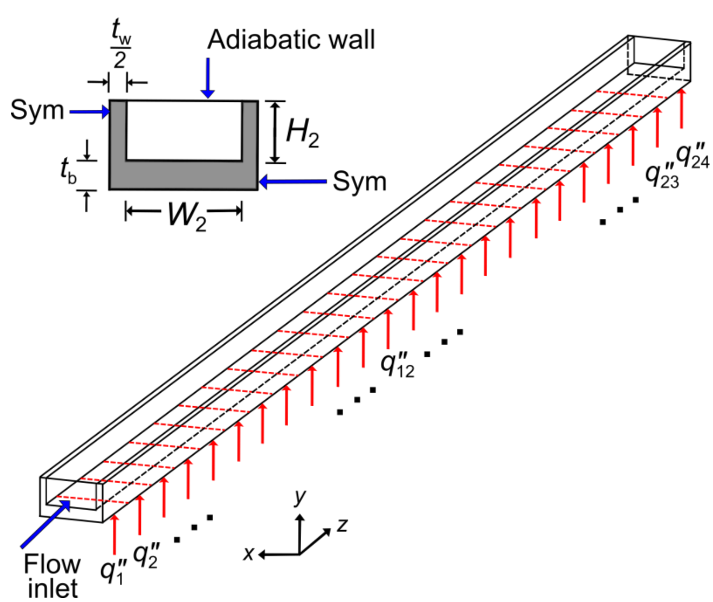

Figure 5.2 – Computational domain used for the analysis of flow boiling in a silicon microchannel subjected to a non-uniform power distribution.

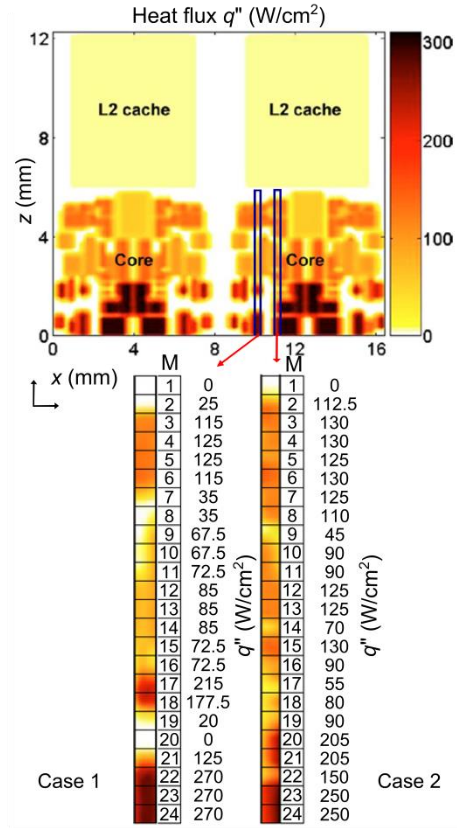

Figure 5.3 – Powermap of a dual-core architecture [54] and the selected cases for simulation with their corresponding heat flux per module.

The non-uniform powermap of the mentioned architecture is depicted in Figure 5.3, where two different power distributions have been selected in the core section in order to provide a realistic simulation of the transient two-phase cooling for such cases. The heat load is highly variable, with a few adiabatic modules and steep gradients to heat fluxes up to 270 W/cm^2. It can be observed that the power density for the L2 cache region is negligibly small (11.3 W/cm^2) compared with that of the core sections, and therefore the analysis is based on the latter regions. The discrete heat flux values for q_1'' to q_{24}'' in Figure 5.3 represent the two different analyzed scenarios and input values to the computational domain shown in Figure 5.2.

5.4 Boundary and operating conditions

Liquid water is used as the coolant at a saturation temperature of T_{sat} = 100 °C for the mesh independence analysis, and validation with a flow boiling correlation using the computational domain in Figure 5.1. For the cases of flow boiling for microelectronic components, a lower saturation temperature of T_{sat} = 60°C and absolute pressure of P_{sat} = 19.93 kPa are considered for the simulations of the silicon microchannel in Figure 5.3. A mass flux condition of G = 500 kg/m^{2}s is specified at the inlet, and a pressure outlet boundary condition is prescribed at the channel exit with a zero gauge pressure corresponding to the saturation pressure.

The solid domain corresponding to silicon is expected to present considerable temperature gradients due to the non-uniformity of the heated zones with relatively high heat fluxes, further exacerbated by local thermal conductivity decrease with temperature. Temperature-dependent thermal conductivity of silicon was incorporated to solve the heat conduction equation in the solid domain with the empirical expression proposed by Glassbrenner and Slack [55] for temperatures up to 800 K, and computed as:

$$k_{\text{si}} = 100\left(0.03 + \frac{1.56}{10^3}T + \frac{1.65}{10^6}T^2\right)^{-1} \tag{32}$$

where the units for temperature are K, and for thermal conductivity W/m-K. The thermophysical properties for silicon, liquid water and its vapor used for the simulations are listed in Table 5.2. The wall boundary conditions are indicated in Figures 5.1 and 5.2, while the internal walls have a non-slip condition.

Table 5.2 – Thermophysical properties of silicon, liquid water and its vapor used for the simulations.

Property	Symbol	Silicon	Water, Vapor at T_{sat} = 100 °C	Water, Vapor at T_{sat} = 60 °C
Density (kg/m^3)	$\rho_{si}, \rho_l, \rho_v$	2330	958.5, 0.595	983.2, 0.1303
Thermal conductivity (W/m-K)	k_{si}, k_l, k_v	Eq. (32)	0.665, 0.025	0.6409, 0.0212
Specific heat (J/kg-K)	c, c_{pl}, c_{pv}	712	4217, 2043	4183, 1937
Dynamic viscosity (Pa-s)	$-, \mu_l, \mu_v$	--	2.82×10^{-4}, 1.226×10^{-5}	4.666×10^{-4}, 1.093×10^{-5}
Surface tension coefficient (N/m)	σ	--	0.0589	0.0662

5.5 Numerical procedure

The CFD-HT software ANSYS® FLUENT® 15.0 was used as the solver for the governing equations through the finite volume approach. The described phase-change model for mass and energy transfer was coupled through the development of a user-defined-function (UDF).

The transient solution for laminar flow was obtained using the Green-Gauss cell based gradient evolution, and a first order implicit temporal discretization for momentum and energy. The coupling of pressure and velocity was performed with the SIMPLE algorithm, and the solution was considered converged when the residuals for mass and momentum were less than 10^{-4}, and for the energy equation less than 10^{-7}.

The single-phase steady state solution for the flow field corresponding to the given mass flux, and isothermal domain at the specified saturation temperature, was used as the initial condition for the flow boiling simulations. The explicit VOF formulation was employed, setting the Courant number for the volume fraction equation to a cutoff value of 0.25. The global Courant number was kept below a value of 1.0 for numerical stability, with resulting time steps in the range of 10^{-7} to 10^{-6} s, depending on the mesh size and mass flux combinations.

5.6 Mesh independence analysis

The domains in the present study were easily meshed with hexahedral elements due to their orthogonal geometry, where the challenge is rather to find the optimum mesh size that provides acceptable grid-independent results. As previously indicated, the channel in Figure 5.1 was used for the mesh sensitivity analysis by means of successive refinements, so the grid-independent model could be compared against available correlations for heat transfer and pressure drop, as discussed in Section 5.3. The number of elements from one case to another was approximately doubled, until attaining a mesh-independency criterion for one or more of the involved field variables, without significant changes in the two-phase flow regime. The chosen operating and boundary conditions for this assessment correspond to a mass flux of 500 kg/m^{2}s, uniform heat flux of 100 W/cm^2, and a saturation temperature of 100 °C. The transient solution was inspected at a flow time of t = 20 ms, when quasi-steady state conditions were reached (i.e., negligible change in two-phase pressure drop and wall superheat from one time step to another).

The criterion $\left|(N^j - N^{j+1}) / N^j\right| < 5\times10^{-3}$ was chosen for the grid-independence assessment, where N^j represents the computed value of the field variable of comparison for the current mesh and N^{j+1} is the same variable but evaluated for the next mesh. The two-phase pressure drop from inlet to outlet and the average surface temperature of the heated wall were chosen as the field variables of comparison together with qualitative comparison of the two-phase flow regime.

Table 5.3 – Two-phase pressure drop and average surface temperature for grid-independence attainment at *t* = 20 ms.

Case	Number of cells	ΔP (Pa)	$\left|(\Delta P^j - \Delta P^{j+1}) / \Delta P^j\right|$	T_w (K)	$\left|(T_w^{\,j} - T_w^{\,j+1}) / T_w^{\,j}\right|$
Mesh 1	33,630	2529.88	1.921×10^{-1}	397.771	3.326×10^{-3}
Mesh 2	64,676	2043.68	2.314×10^{-1}	396.448	2.224×10^{-3}
Mesh 3	113,988	2516.64	5.071×10^{-2}	395.566	5.255×10^{-3}
Mesh 4	267,900	2644.27	5.049×10^{-3}	393.487	8.767×10^{-4}
Mesh 5	524,400	2657.62	--	393.142	--

Table 5.3 presents the results for the mesh independence analysis, where the element size of Mesh 4 was selected for the simulations in the present study, in order to balance solution accuracy with computation time. Using this mesh density, the simulation of 20 ms of boiling flow for each case required between 40 and 65 hours of computational time using four cores of an Intel® Xeon® processor-based workstation at 3.1 GHz. The computational domain of Figure 5.2 (silicon microchannel) was meshed with an element density between Mesh 4 and Mesh 5, resulting in 632,400 cells due to the slight refinement and inclusion of the silicon domain. The computational time

required to obtain two-phase flow data for 20 ms of flow for these latter cases with the same machine was between 320 and 400 hours, due to the more complex solution and reduction in time step required for stability.

5.7 Comparison of model results with an empirical correlation

The results obtained for the plain microchannel in Figure 5.1 were used for validation with the correlation proposed by Bertsch et al. [27] for flow boiling in small passages. This correlation has the composite form accounting for nucleate boiling and forced convection heat transfer from the widely known correlation by Chen [56], intended for flow boiling in tubes with conventional size; this is modified in [27] in order to account for confinement effects observed in mini and microchannels. The correlation is tailored from 3,899 data points for 12 different fluids (including water) for a wide range of flow rates and heat fluxes relevant to different applications, covering the analyzed cases for comparison of the present study.

The wall superheat versus heat flux (flow boiling curve) obtained with the chosen empirical correlation and the CFD model results are compared in Figure 5.4; the computed values between both approaches are in reasonable agreement. It is also observed that for heat fluxes above 90 W/cm^2 the wall superheat predicted by the CFD model starts to be slightly higher than the computed value using the correlation. However, at such heat fluxes the two-phase flow regime will be significantly affected and bubble confinement effects may arise, resulting in higher wall temperatures, where the predictive capabilities of semi-empirical correlations (formulated independently from two-phase flow regime) may be poorer.

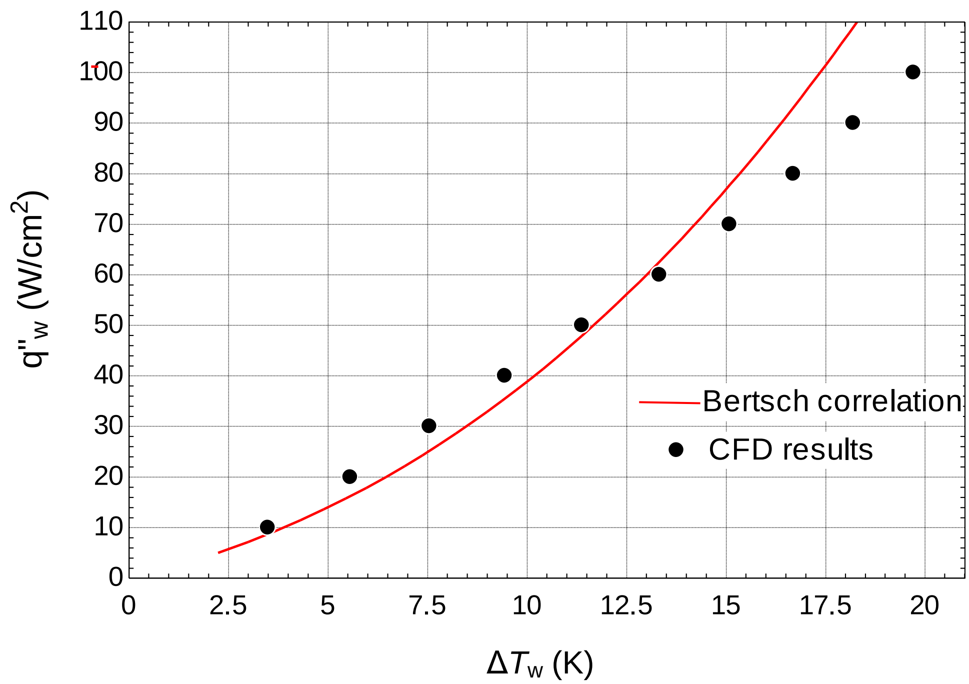

Figure 5.4 – Comparison of the flow boiling curves computed with the correlation by Bertsch et al. [27] and the present CFD model (G = 500 kg/m^{2}s, $T_{f,in}$ = 100°C).

Regarding the hydrodynamic behavior, the computed two-phase pressure drop by the CFD-HT model was compared against the value predicted by the following expression for a channel with variable flow quality (i.e., boiling) [28]:

$$\Delta P_{\mathrm{tp}} = \left(-\frac{\partial P}{\partial z}\right)_{\mathrm{fr,L0}} \frac{L_{\mathrm{h}}}{x_{\mathrm{out}}} \int_0^{x_{\mathrm{out}}} \phi_{\mathrm{L0}}^2\,(x) dx \tag{33}$$

where the first term on the right is the all-liquid (single phase) pressure drop, increased by the two-phase pressure drop multiplier integrated over the heated length. The two-phase pressure drop multiplier was computed as a function of the local quality using the correlation of Muller-Steinhagen and Heck [57], which is suitable for water and dielectric refrigerants in small flow passages. The two-phase pressure drop values computed with the CFD model and those predicted using Equation (33) were compared for the cases with mass fluxes of G = 250 kg/m^{2}s , G = 500 kg/m^{2}s, and a heat flux of q" = 50 W/cm^2, obtaining a good agreement between both methods, as can be noted in the results listed in Table 5.4.

Table 5.4 – Comparison of the predicted two-phase pressure drop using Equation (33) and multiplier from [57] against the CFD model results.

	Eq. (33) with pressure drop multiplier from [57]			CFD results
Mass flux (kg/m^{2}s)	Exit quality (x_{out})	$\frac{1}{x_{\mathrm{out}}}\int_0^{x_{\mathrm{out}}} \phi_{\mathrm{L0}}^2\,(x)dx$	ΔP_{tp} (Pa)	ΔP_{tp} (Pa)
250	0.02658	5.632	1492.57	1553.74
500	0.01329	4.916	2605.83	2557.08

5.8 Transient temperature distribution and two-phase flow regimes at T_{sat} = 60 °C

The operating conditions were set to those listed in Table 5.2 for a saturation temperature of 60 °C, with the main objective of maintaining the silicon domain at lower temperatures. The first set of simulations was analyzed during 10 ms of two-phase flow with the non-uniform heating conditions corresponding to Case 1 and 2 from Figure 5.3. The transient heating behavior and evolution of the two-phase flow regime due to boiling for these cases are depicted in Figure 5.5, where the computed 3D temperature fields are shown on the internal wall surface, edges, and bottom of the silicon microchannel using a semi-transparent contour in order to visualize and track the vapor-liquid interface which is denoted by a dark blue surface.

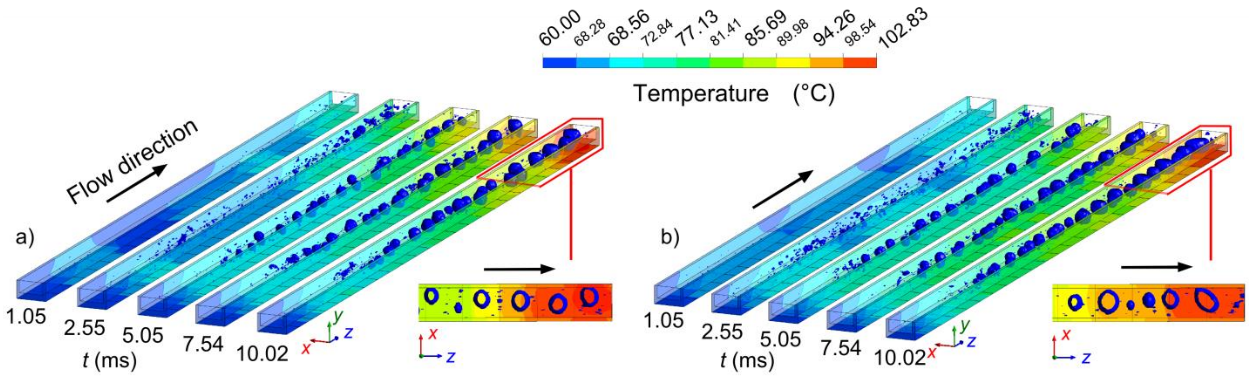

Figure 5.5 – Transient temperature field (°C) and two-phase flow regime at G = 500 kg/m^{2}s, and $T_{f,in}$ = T_{sat} = 60 °C for the heating conditions of: a) Case1, b) Case 2.

Visual inspection of Figures 5.5a and 5.5b provides insights about the transient boiling process in the flow passage. At t = 1.05 ms, the heat spreading from the modules with highest heat fluxes for Cases 1 and 2 can be observed, where bubble nucleation starts at zones with highest wall superheat, in agreement with the phase-change criteria. At t = 2.55 ms, an increased amount of generated vapor can be observed; for times between 5.05 and 10.02 ms, the two-phase flow regime continues to develop and larger bubbles are located in downstream regions, as a result of coalescence between smaller vapor structures nucleated upstream. The zoomed-in regions in Figure 5.5 depict a top view of the outlet section, indicating the presence of bubble confinement.

Since the heat flux distribution for both analyzed cases in the present investigation is spatially highly variable, the definition of an average surface temperature might lead to ambiguities due to the significant gradients in local temperature along the channel. In order to better quantify the transient heating behavior and high temperature spots, the computed temperatures are presented instead as an area-averaged value for six zones along the channel, consisting of four discretized modules each, and presented as T_{n-m} (e.g., T_{1-4} represents the average surface temperature for the modules 1 to 4 according to the nomenclature given in Figure 5.3).

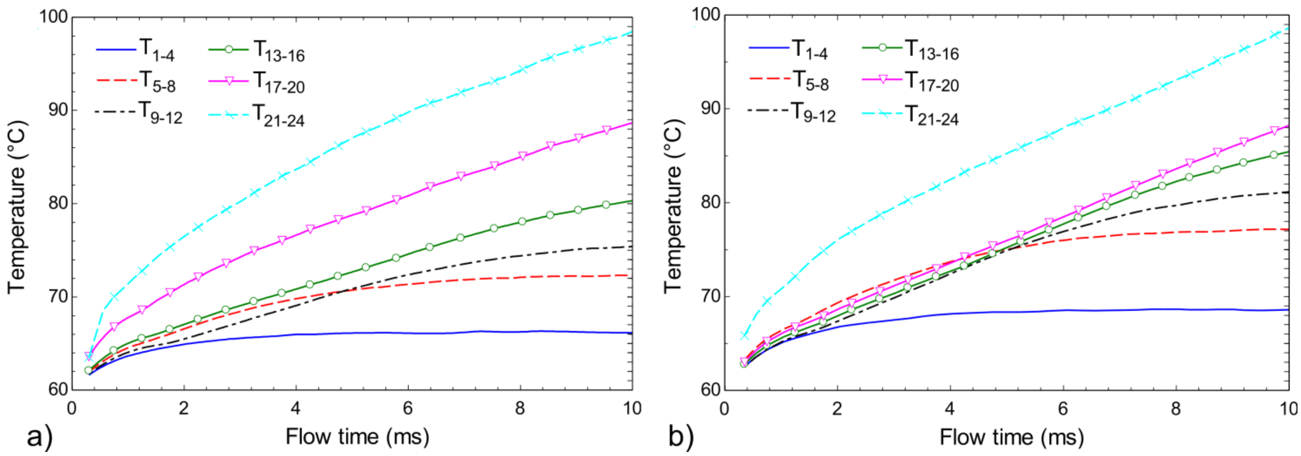

Figure 5.6 – Temperature variation in different modules of the silicon microchannel at G = 500 kg/m^{2}s, $T_{f,in}$ = T_{sat} = 60 °C, and the non-uniform powermap of: a) Case 1, b) Case 2.

The transient average module temperatures caused by the two analyzed powermaps are plotted in Figure 5.6; the temperature near the inlet section (modules 1 to 4) remains stable at a value of ~ 66 °C, which is slightly above the saturation temperature specified at the inlet for such cases. For modules 5-8 and 9-12 the temperature increases with time due to the higher heat fluxes near these zones, with stabilizing values around 6 and 8 ms of flow, respectively. As observed in Figure 5.6a, the formation of bubbles comparable in size with the channel cross-section occurs at downstream locations due to vapor coalescence, leading eventually to bubble confinement which results in increased temperatures for modules 13-24. Vapor phase accumulation and heat flux non-uniformity with high localized values are identified as the main issues in the cooling performance for this case.

5.9 Effect of flow inlet direction on the flow boiling characteristics

The results of the two-phase flow regime available through the surface-tracking technique indicate the presence of slugs at the outlet section due to vapor accumulation that significantly constrains the boiling heat transfer. Hence, it is of interest to study the effect of changing the flow direction in order to enhance boiling at the locations with highest heat fluxes. The transient boiling behavior for flow in the negative *z*-direction is depicted in Figure 5.7, where the powermap is shown on the left in order to compare with temperature contours and flow regime on the right.

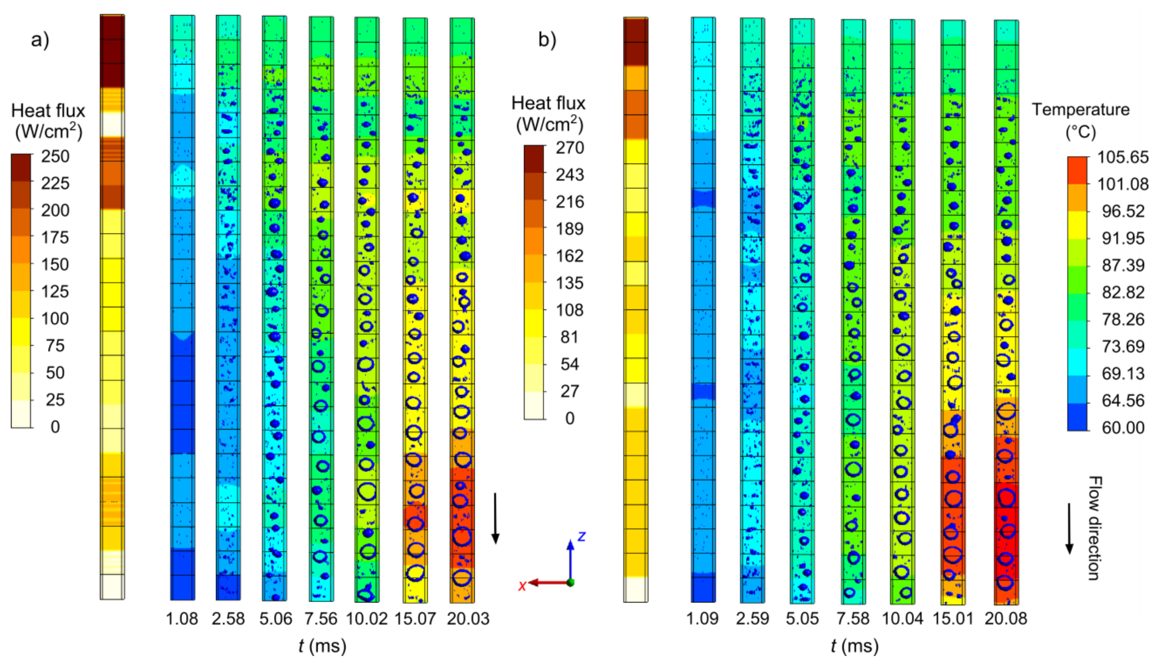

Figure 5.7 – Transient flow boiling behavior in the negative *z*-direction and temperature contours at G = 500 kg/m^{2}s, $T_{f,in}$ = T_{sat} = 60 °C, and powermaps of: a) Case 1, b) Case 2.

For the heating conditions of Case 1 (Figure 5.7a), since the fluid enters at the location with highest heat fluxes (250 W/cm^2), nucleation immediately starts here and the temperature for modules 21 to 24 (T_{21-24}) stabilizes after ~ 5 ms at a value of ~ 82 °C, see Figure 5.8a, which is significantly lower than the temperature for the case with flow in the positive *z*-direction (98.48 °C at t = 10 ms and increasing).

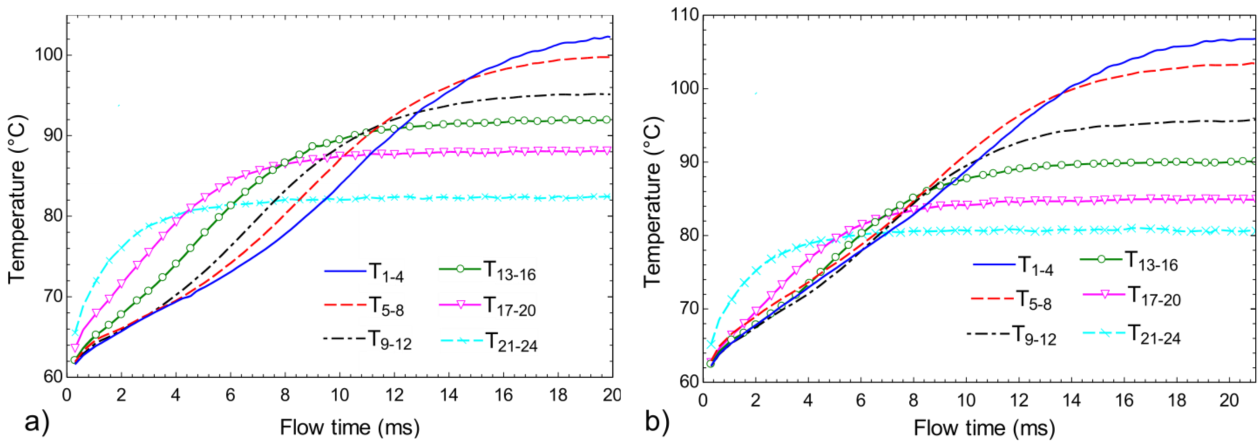

Figure 5.8 – Temperature variation in different modules of the silicon microchannel with flow in the negative z-direction at G = 500 kg/m^{2}s, $T_{f,in} = T_{sat}$ = 60 °C, and the non-uniform powermap of: a) Case 1, b) Case 2.

The main reason for the decrease in temperature from one case to another is that the boiling process is intensified in the region with highest heat flux and for the scenario analyzed in this section there is no accumulation of vapor phase at this location since it is the inlet. However, the relatively high frequency of bubbles nucleated at this zone will eventually result in coalescence at downstream locations, and exhibit a similar evolution as in the previously analyzed cases, where the boiling process will not be as intense as that at the inlet due to vapor confinement. The transient variation of temperature in different regions of the channel is plotted in Figure 5.8 for both of the analyzed powermaps for a flow time of ~ 20 ms; it can be observed that quasi-steady state conditions are reached at different times for each section and that hot spot values occur at downstream regions at values of ~ 106 °C near the outlet due to vapor-phase accumulation, as previously discussed. The highest temperature gradient occurs between inlet and outlet sections of channel, with a value of $T_{1-4} - T_{21-24} = 19.99$ °C for Case 1, and $T_{1-4} - T_{21-24} = 25.93$ °C for Case 2, which represent a significant improvement when compared with the flow arrangement in the positive *z*-direction, offering an improved quasi-steady temperature field for such high heat fluxes.

5.10 Effect of inlet subcooling on flow boiling in the negative *z*-direction

In order to further expand this initial analysis of flow boiling and model prediction capabilities, the inlet temperature of the coolant was reduced to $T_{f,in}$ = 50 °C (keeping the saturation temperature at T_{sat} = 60 °C and mass flux at G = 500 kg/m^{2}s) with the objective of reducing the accumulation of vapor-phase due to evolution of the two-phase flow regime along the channel that degrades heat transfer at outlet section. Figure 5.9 shows a comparison of the quasi-steady state solutions (around t = 20 ms) for the two-phase flow regime and corresponding temperature field for the analyzed cases with inlet water at both the saturation temperature and subcooled by 10 °C. The average temperature for each section is shown below the corresponding zone, and a classification for the evolution of the two-phase flow regime is provided at the bottom. These regimes are comparable to those reported in the experimental study by Choi et al. [58] for flow boiling of water in rectangular cross-section channels with a hydraulic diameter of 500 µm. It can be noted that with the use of subcooling the buildup of vapor phase within the channel is reduced, arising from condensation of the generated bubbles with the surrounding liquid phase. Although some vapor confinement is observed at the outlet sections, it is not as severe as that observed for the cases with water entering the domain at the saturation temperature, and the zone corresponding to dispersed bubbly flow is enlarged. For the subcooled cases, the highest temperature gradients correspond to

$T_{1-4} - T_{21-24} = 20.65$ ℃ for Case 1, and $T_{1-4} - T_{21-24} = 26.82$ ℃ for Case 2, which are very similar to those computed for the previous cases; however, the hot spot temperatures for the subcooled cases are reduced approximately by 10 % when compared with the saturated scenarios.

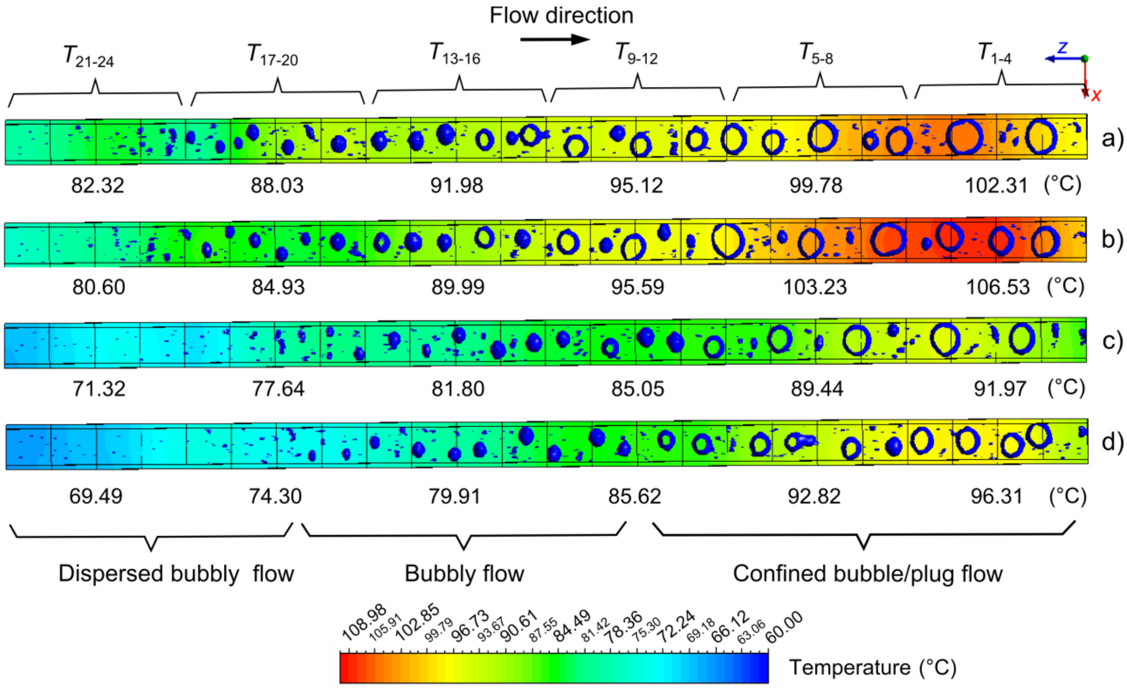

Figure 5.9 – Comparison of the quasi-steady state solutions for the two-phase flow regime and temperature field for the analyzed cases with flow in the negative *z*-direction at G = = 500 kg/m^{2}s, T_{sat} = 60 °C, and the powermaps of: a) Case 1 - $T_{f,in}$ = T_{sat}, b) Case 2 - $T_{f,in}$ = T_{sat}, c) Case 1 - $T_{f,in}$ = 50 °C, d) Case 2 - $T_{f,in}$ = 50 °C.

The variation of the heat transfer coefficient (computed as the local heat flux divided by the local wall superheat) along the microchannel for the different analyzed scenarios is plotted in Figure 5.10; the highly variable behavior is associated with the non-uniform distribution and values of local power densities, with the highest heat transfer coefficients at the inlet section (z = 6 mm) resulting from the high heat flux and relatively low wall superheat at this location. A very similar behavior between the saturated and subcooled cases is observed, arising from the comparable offset between the fluid inlet temperature and the resulting surface temperature.

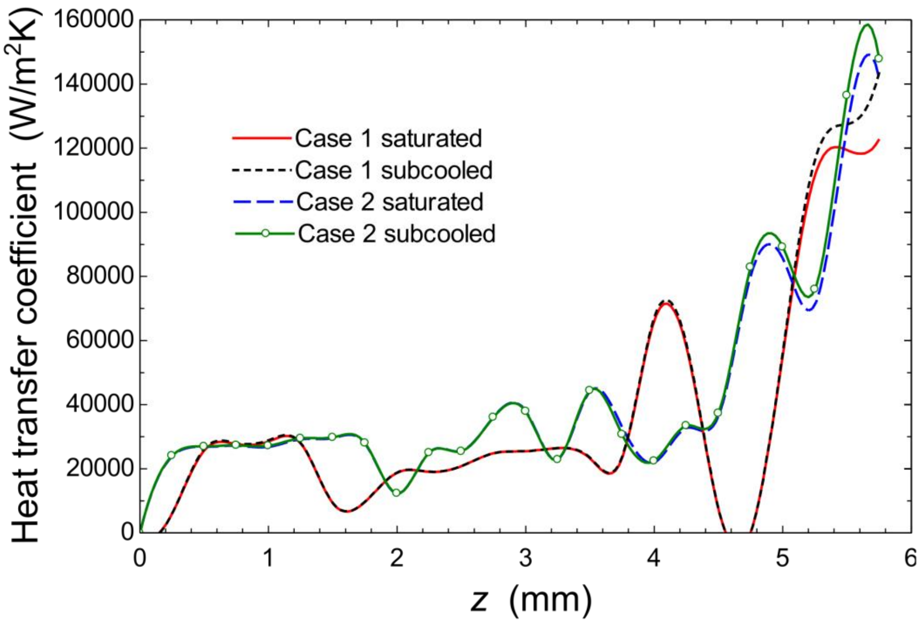

Figure 5.10 – Variation of the heat transfer coefficient along the microchannel for the analyzed cases with flow in the negative z-direction.

5.11 Two-phase pressure drop

The transient variation in the total two-phase pressure drop is plotted in Figure 5.11, where a fluctuating behavior is present for all of the analyzed cases, associated with the continuous change in the amount of vapor phase within the channel. The peaks correspond to instants at which the vapor amount significantly increases and constrains the flow, and the valleys correspond to instants at which a large bubble (confined or plug) exits the domain. It can be observed that the pressure drop starts at a higher value for the cases in which flow is in the negative *z*-direction, when compared to their counterparts. The average pressure drop after certain time is similar for all cases with water entering at the saturation condition due to the same operating mass flux, and comparable two-phase flow regime evolution, with their average values listed in Table 5.5.

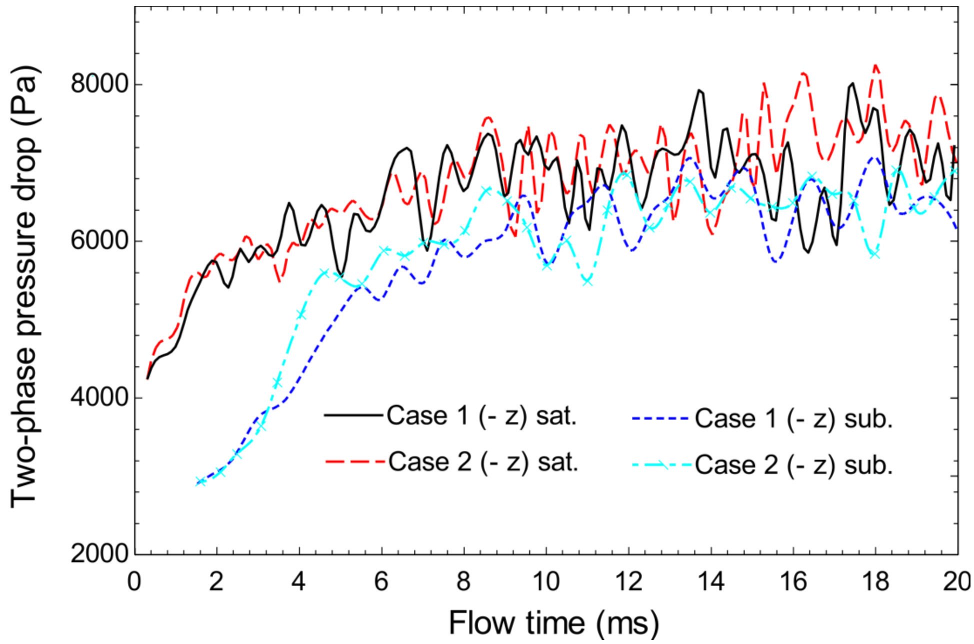

Figure 5.11 – Comparison of the two-phase pressure drop fluctuations for the different analyzed cases and flow conditions.

The average two-phase pressure drop for the subcooled cases is slightly lower than the saturated scenarios due to the reduction in vapor phase amount within the channel for the evolved two-phase flow regimes (see Figure 5.9), hence providing a better cooling performance in both temperature and hydrodynamic aspects when compared with the saturated scenarios.

Table 5.5 – Average two-phase pressure drop for the analyzed cases and flow arrangements.

Case	Case 1 (-z) saturated	Case 2 (-z) saturated	Case 1 (-z) subcooled	Case 2 (-z) subcooled
ΔP (Pa)	6867.53	7009.28	6225.76	6291.45

5.12 Remarks and conclusions

This chapter presented the initial approach toward the development of a three-dimensional CFD-HT model for the assessment of flow boiling phenomena at microscale. Results from the present study indicate the promising capability of the implemented two-phase model with phase change to predict trends from flow boiling correlations in microchannels, with remarkable capabilities for two-phase flow visualization, evolution, and tracking. The model was also tested with a realistic power map, providing results that indicate the strong effect of heat flux non-uniformity on both the hydrodynamics (two-phase flow regime evolution) and boiling heat transfer. The completion of this chapter partially meets the challenges outlined in Section 2.2.1 by representing one of the first studies analyzing the two-phase cooling in silicon microchannels under relevant conditions for the stacking of ICs, motivating for its improvement and further validation with more complex domains.

CHAPTER 6. IMPROVEMENT OF THE PHASE-TRACKING CAPABILITIES THROUGH THE COUPLED LEVEL-SET VOLUME OF FLUID (CLSVOF) METHOD

The results in the previous chapter indicated the very promising capabilities of the proposed method to estimate the flow boiling features such as temperature, pressure, and phase distribution in microchannels, while also reporting good agreement when compared to available empirical correlations. Although remarkable advances were achieved, one of the identified challenges in such approach is the interface resolution, dictated by the mesh size. Further reducing the mesh size for a sharper interface reconstruction has a significant constraint on the time step, so therefore a tradeoff exists between two-phase prediction and computational time.

In an effort to expand the studied possibilities for the modeling of flow boiling, this chapter presents an improvement to the modeling technique by using the Coupled Level Set – Volume of Fluid (CLSVOF) technique. The advantages of such method are explained and demonstrated by improving the surface tension calculation and interface reconstruction in the simulation of flow boiling in a silicon microgap with cylindrical pin fins, a significantly larger domain than the plain microchannels studied in the last chapter, and important leap toward meeting the thesis goals as these are closer to the outlined challenges. The flow boiling regimes with their spatial and temporal evolution are compared between the standard VOF and the CLSVOF methods by maintaining the operating conditions. Results indicate that the CLSVOF offers a sharper interface reconstruction than the standard VOF method by predicting bubble nucleation and departure mechanisms more closely to the actual physics to the problem, constituting the key achievement to allow direct comparison with the generated experimental data in the final chapter of this dissertation.

6.1 Coupled Level- Set Volume of Fluid (CLSVOF) model

When it comes to phase-change modeling, the standard VOF model (such as the one presented in Chapter 5) has been preferred over other alternative techniques due to its conservative formulation in which the interface is advected without violating the mass conservation. However, the main disadvantage of the VOF model is the resolution of the interface when compared with other available models. Other alternatives for a sharper interface reconstruction are the Level-Set (LS) and Phase-Field (PF) methods; however, they present the disadvantage of being not-conservative in mass. A more detailed discussion regarding the features of these methods may be consulted in the studies by Aniszewski et al. [59], and Hua et al [60]. In an effort to reduce the associated issues with the available models for the analysis of multi-phase flows, Sussman and Puckett [61] proposed and developed an algorithm more accurate than either of the original versions of the LS or the VOF techniques; the so-called Coupled Level-Set Volume of Fluid (CLSVOF) method. In the cited study, it was shown that the CLSVOF could calculate sharp interfaces as the LS method, with the important advantage of conserving mass within a fraction of a percent, while the standard LS method could lose up to 20% of the mass.

The Coupled Level-Set Volume of Fluid (CLSVOF) method is a hybrid approach in which the desirable features of each technique are combined, such as the accurate spatial gradient calculation of the LS model, and the volume-conservative nature of the VOF model. In the CLSVOF model, the advection equation for the Level-Set function ϕ is incorporated (in addition to the volume fraction equation, Equation 10) for the phase-tracking as:

$$\frac{\partial \phi}{\partial t} + \nabla \cdot (\vec{v}_{\mathrm{int}} \phi) = 0 \tag{34}$$

where $\vec{v}_{\mathrm{int}}$ is the characteristic velocity of the interface, calculated as $\vec{v}_{\mathrm{int}} = \vec{v} + m_{\mathrm{v}}^{"}/\rho$. In the case of no phase-change, the velocity of the interface therefore corresponds to the velocity field. The term $m_{\mathrm{v}}^{"}$ represents the phase-change mass flux between phases due to boiling, and its calculation was discussed in Section 5.2 through Equation (24) of the proposed phase-change model.

The LS function ϕ is a signed distance to identify the interface $(\phi = 0)$ by defining the primary phase (liquid) as the set of points where $\phi > 0$ and the secondary phase (vapor) as the set of points where $\phi < 0$. This definition makes the LS function smooth and continuous across the interface, hence improving the accuracy of both the normal and curvature of the interface when compared with the standard VOF model where the volume fraction is discontinuous across the interface [62]. The calculation of the unit normal vector to the interface and the interface curvature are improved with the LS function as:

$$\vec{n} = \left. \frac{\nabla \phi}{|\nabla \phi|} \right|_{\phi=0} \tag{35}$$

$$\kappa = \nabla \cdot \frac{\nabla\phi}{|\nabla\phi|}\bigg|_{\phi=0} \tag{36}$$

The velocity field $\vec{v}$ is computed from the momentum equation introduced in Section 5.2 through Equation (11), where the source term for surface tension ($\vec{F}$) is also calculated with the CSF model [49], but now using the LS function ϕ as:

$$\vec{F}_{\mathrm{st}} = \sigma \frac{\rho\kappa\delta(\phi)\vec{n}}{\frac{1}{2}(\rho_l + \rho_{\mathrm{v}})} \tag{37}$$

$$\delta(\phi) = \begin{cases} 0 & |\phi| \geq \alpha \\ \dfrac{1 + \cos(\pi\phi/\alpha)}{2\alpha} & |\phi| < \alpha \end{cases} \tag{38}$$

where $\alpha = 1.5h$, and h is the grid spacing. The advantage of the LS function for interface curvature representation provides a more accurate surface tension calculation than using the standard VOF method, which is a significant advantage relevant to microscale applications where such effects are dominant. Physical properties, such as density and viscosity, to solve the momentum equation are computed as:

$$\rho = \rho_{\mathrm{v}}\big(1 - H(\phi)\big) + \rho_{\mathrm{l}}H(\phi) \tag{39}$$

$$\mu = \mu_{\mathrm{v}}\big(1 - H(\phi)\big) + \mu_{\mathrm{l}}H(\phi) \tag{40}$$

where $H(\phi)$ is a Heaviside function defined as:

$$H(\phi) = \begin{cases} 1 & \text{if } \phi > 0 \\ 0 & \text{otherwise} \end{cases} \tag{41}$$

In order to reduce the mass loss problem of the standard LS method, both the LS and VOF function values are used for the interface reconstruction, where the solution of the volume fraction equation is used to get the size of the cut in the cell where the interface is advected, and the gradient of the LS function provides the direction of the interface [62]. The PLIC algorithm [50] is used for the interface reconstruction, and after this step is completed, all of the possible distances from a given point to the front-cut segments are minimized to reinitialize the LS function [62].

6.2 Computational domain

Recalling that the ultimate application for developing such models is the prediction of the two-phase cooling in the TDVs described in Chapter 3, the computational domain is based on the dimensions for the interlayer cooling of such devices. Considering the complexity and transient nature for modeling flow boiling in such application, the simulation of the entire domain and its number of surface features (unlike the case of steady-state single phase cooling) results computationally restrictive even using high-performance computing. Therefore for the present investigation just a portion of the silicon microgap is considered, in which it is included a sufficient amount of pin fins in order to simulate the flow boiling phenomena in a relatively complex computational domain where the flow can interact in more than one direction. Figure 6.1 depicts the analyzed domain consisting of a portion of the microgap TDV populated with cylindrical pin fins distributed on a length of 10 mm, and a width of 2 mm; dimensions of pin fins and spacing correspond to those of the described TDVs in Chapter 3. Adiabatic entrance and exit sections of 0.6 mm each are also defined in the computational domain. It is important to point out here that for the cases reported in this chapter, the hotspot geometry and non-uniform heating were not considered due to the fact that for the present study the surface tracking capabilities and their improvement are the main interest; the ultimate comparison of the generated in-house experimental data with the refined model resulting from this study is reserved for the final chapter of this dissertation.

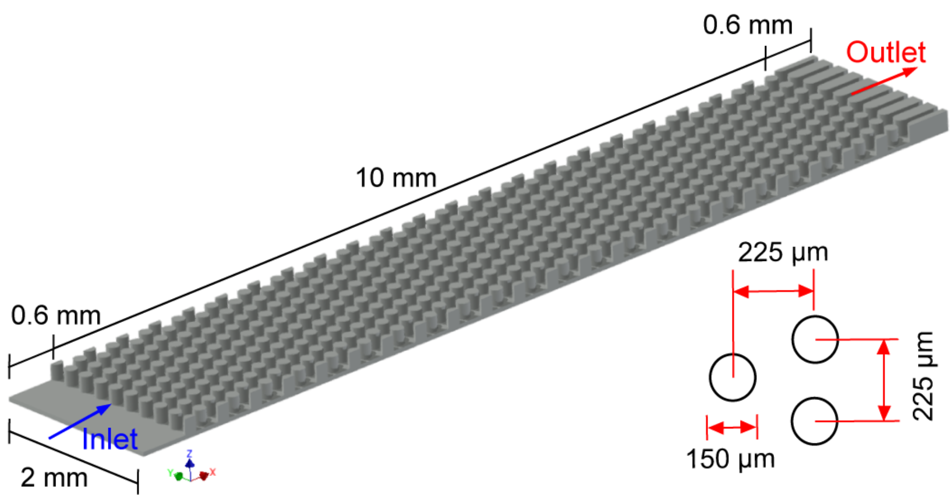

Figure 6.1 – Schematic of the analyzed portion of the silicon microgap and its relevant dimensions.

6.3 Boundary and operating conditions

Regarding boundary conditions for the present modeling, heating in the form of a constant heat flux of $q'' = 100$ W/cm^2 is defined at the bottom surface of the computational domain in the area that is populated by the cylindrical pin fins only, while the bottom surfaces below the inlet and exit sections and top wall of the microgap are prescribed as adiabatic surfaces. The lateral surfaces of the computational domain are defined as symmetry boundary conditions, considering that 10 rows of pin fins may provide useful insight for the analysis of the two-phase flow regime evolution, and the objective of the present study is comparing the interfacial resolution and implications of using the VOF and CLSVOF methods for this application. The flow inlet is specified with a constant mass flux condition using the dielectric refrigerant R245fa with a value of G = 1000 kg/m^{2}s at a saturation temperature of T_{sat} = 30 °C. The fin structures located in the exit section serve the purpose of splitting the flow in different outlets in order to mitigate flow reversal issues in the simulation and hence help its convergence; these outlet faces are specified as pressure outlets. The internal walls where the fluid and solid domains interact are prescribed with no-slip boundary conditions for the liquid phase, while also specifying a temperature continuity condition at the solid/fluid interface. The thermal conductivity of silicon is calculated as a function of the local temperature with the values obtained from Equation (32). The thermophysical properties of silicon and R245fa used for the present modeling are listed in Table 6.1.

Table 6.1 –Thermophysical properties of the silicon domain, liquid R245fa and its vapor at T_{sat} = 30 °C.

Property	Symbol	Silicon	R245fa (liquid)	R245fa (vapor)
Density (kg/m^3)	$\rho_{\mathrm{si}}, \rho_l, \rho_{\mathrm{v}}$	2330	1325	10.13
Thermal conductivity (W/m-K)	$k_{\mathrm{si}}, k_l, k_{\mathrm{v}}$	Eq. (32)	0.07966	0.01436
Specific heat (J/kg-K)	$c, c_{\mathrm{p}l}, c_{\mathrm{pv}}$	712	1333	972.2
Dynamic viscosity (Pa-s)	$-, \mu_l, \mu_{\mathrm{v}}$	--	3.79×10^{-4}	1.035×10^{-5}
Surface tension coeff. (N/m)	σ	--	0.01299	

6.4 Numerical procedure

The CFD solver ANSYS® FLUENT® 15.0 was used for the numerical solution of the governing equations through the finite volume method; the built-in multiphase models for the VOF and also CLSVOF techniques in this package were used and coupled with the described phase-change model through the development of a user-defined-function (UDF) for mass and energy source terms, as described in Section 5.2. The problem is treated as transient laminar with a first-order explicit temporal discretization, and a second order upwind spatial discretization.

The coupling between pressure and velocity fields is done through the use of the Pressure Implicit with Splitting of Operators (PISO) algorithm, and the solution for each time step was considered converged when the residual values reached to a value of less than 10^{-4} for the mass and momentum equations, and less than 10^{-7} for the energy equation. The time step was automatically adjusted with values in the range from 10^{-8} to 10^{-6} s in order to maintain the global Courant number below a value of 1.0 for stability.

The transient simulation for these cases was computed through a High Performance Computing (HPC) cluster, in which a total of 80 cores from Intel® Xeon® E5-2680 v2 processors at 2.8 GHz are used through a parallel configuration with a 4x QRD InfiniBand® Interconnection at 40 GB/s.

6.5 Mesh independence

The computational domain was meshed through the use of the same hybrid method as the one described in Section 4.1.4, where hexahedral elements are used for the fluid domain and tetrahedral elements for the solid (silicon) domain. The parallel meshing of the computational domain indicated in Figure 6.1, under this specified settings, was achieved in ~2 hours for a model with ~2.5 million elements using the ANSYS® Meshing software with 4 cores of an Intel® Xeon® E5-1507 processor, consuming ~4 GB of RAM memory.

A mesh sensibility analysis was conducted to ensure grid-independency; the field variables used for comparison were the average bottom surface temperature and the two-phase pressure drop for the quasi-steady state solution. Three mesh models with different element densities were created: the first with 912,234 cells, the second with 2,446,686 cells, and a third mesh with 3,895,640 cells. While the first mesh presented convergence issues due to its coarse resolution, the results for the second and third meshes were in a reasonable agreement with an error between solutions of 1.5 % for absolute temperature, and 7.5 % for the mean two-phase pressure drop. The second meshing scheme was therefore selected in order to balance the solution accuracy with the computational time, which is directly increased by reducing the element size due to the Courant number definition in such explicit formulations. The computational time for the solution to reach the quasi-steady state with the second mesh was ~80 hours while the third mesh took ~200 hours for the same problem using the HPC resources aforementioned.

6.6 Solution initialization

The two-phase flow calculation requires being initialized with the single-phase isothermal flow field solution for the specified mass flux; the solution data is then loaded into the two-phase case file and the transient flow boiling simulation is started. Figure 6.2

depicts the single-phase flow field solution as a velocity contour (m/s) in a mid-section plane; the fluid properties for such solution correspond to those listed in Table 6.1 for a mass flux of 1000 kg/m^{2}s and a saturation temperature of 30 °C. The hydrodynamic solution produces expected features such as the recirculation zones in the back side of the pins resulting from the boundary layer separation; such zones are denoted in the streamlines at the bottom of Figure 6.2.

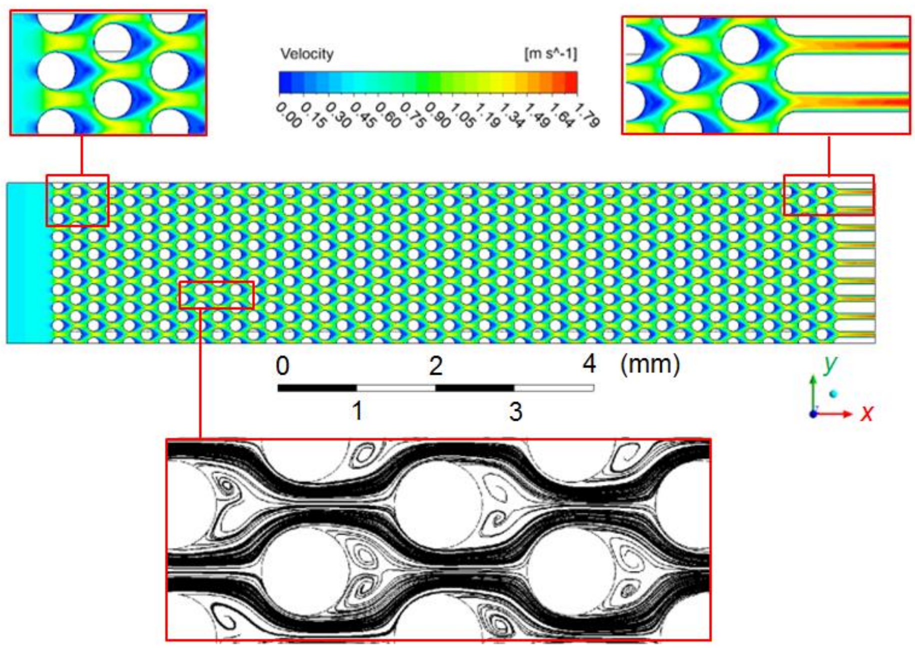

Figure 6.2 – Velocity magnitude contours (m/s) for the single-phase isothermal solution at G = 1000 kg/m^{2}s and T_{sat} = 30 °C.

6.7 Comparison of two-phase flow regime evolution between VOF and CLSVOF model results

Once the saturated, single-phase flow field is loaded, the heat flux condition at the bottom of the microgap is enabled and vapor formation will start. According to the conditions defined in the phase-change model, bubble nucleation will occur at fluid cells in the fluid-solid interface that exceed the saturation condition. Although the real process involves bubble nucleation at wall crevices with entrapped vapor, these effects cannot be captured through a CFD based-model considering the large number of features in the computational domain. However, it has been observed that such approach is reasonable and comparable to the experimental bubble nucleation processes reported in the literature for similar configurations and refrigerants, which are discussed in Section 6.8.

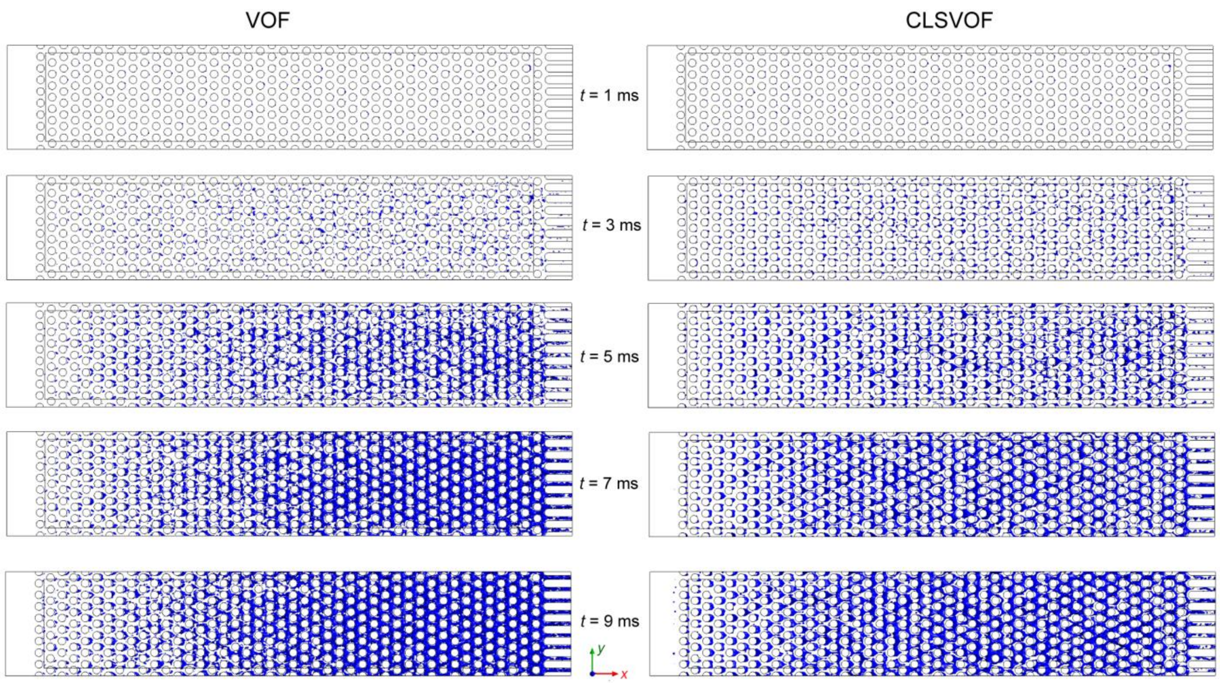

Figure 6.3 – Transient evolution of the two-phase flow regime in the silicon microgap predicted by the VOF and CLSVOF models for a mass flux of 1000 kg/m^{2}s and a heat flux of 100 W/cm^2. The blue surface indicates the liquid-vapor interface as seen from a top view (+z).

The evolution of the two-phase flow regime for the saturated flow boiling conditions in the silicon microgap is depicted in Figure 6.3 from a top view (+z) perspective, where the liquid-vapor interface is represented by a blue isosurface. At first glance, it may be supposed that both methods provide similar results in terms of the flow regime evolution inside the microgap. For the first millisecond (ms) of flow, a few bubbles start to nucleate at the rear part of the pin fins, and these can be barely noticed in the corresponding subset of Figure 6.3. As the flow simulation time increases, at t = 3 ms it can be noted a significantly higher amount of vapor inside the microgap as the silicon temperature is increasing. For latter times, the two-phase flow regime keeps evolving as a result of the tracking capabilities of both the VOF and CLSVOF that allow vapor merging. The trend of vapor accumulation within the microgap continues until quasi-steady state conditions are reached, which are defined as the point in which the two-phase flow regime and variable fields such as temperature and pressure are not varying significantly with time. For the present cases, such point was observed approximately after 10 ms of two-phase flow conditions. It can be observed in Figure 6.3 how the vapor structures between t = 7 ms and t = 9 ms are very similar, resulting from the balance between the applied heat flux and mass fluxes, boiling conditions through the phase-change model, and the continuous vapor generation and removal from the computational domain.

Although the overall trend in vapor generation and evolution between both methods is similar, there are important differences regarding the interfacial reconstruction when the details of each solution are analyzed. Figure 6.4 shows the comparison between both methods for the quasi-steady state solution at t = 10 ms, where the zoom-in windows provide further details of the vapor structures and their behavior near the inlet, center, and outlet of the analyzed silicon microgap. Starting from the inlet, and recalling that the flow direction is in the positive x-direction, it may be observed that bubble nucleation starts from the first column of pins and that the reconstructed interfaces actually differ between both methods; for the standard VOF method these bubbles have an oval shape and some of them are somewhat distorted, while the CLSVOF clearly offers a sharper interfacial reconstruction with rounded and smooth bubbles that better resemble the physics of the problem (see Section 6.8 for further discussion).

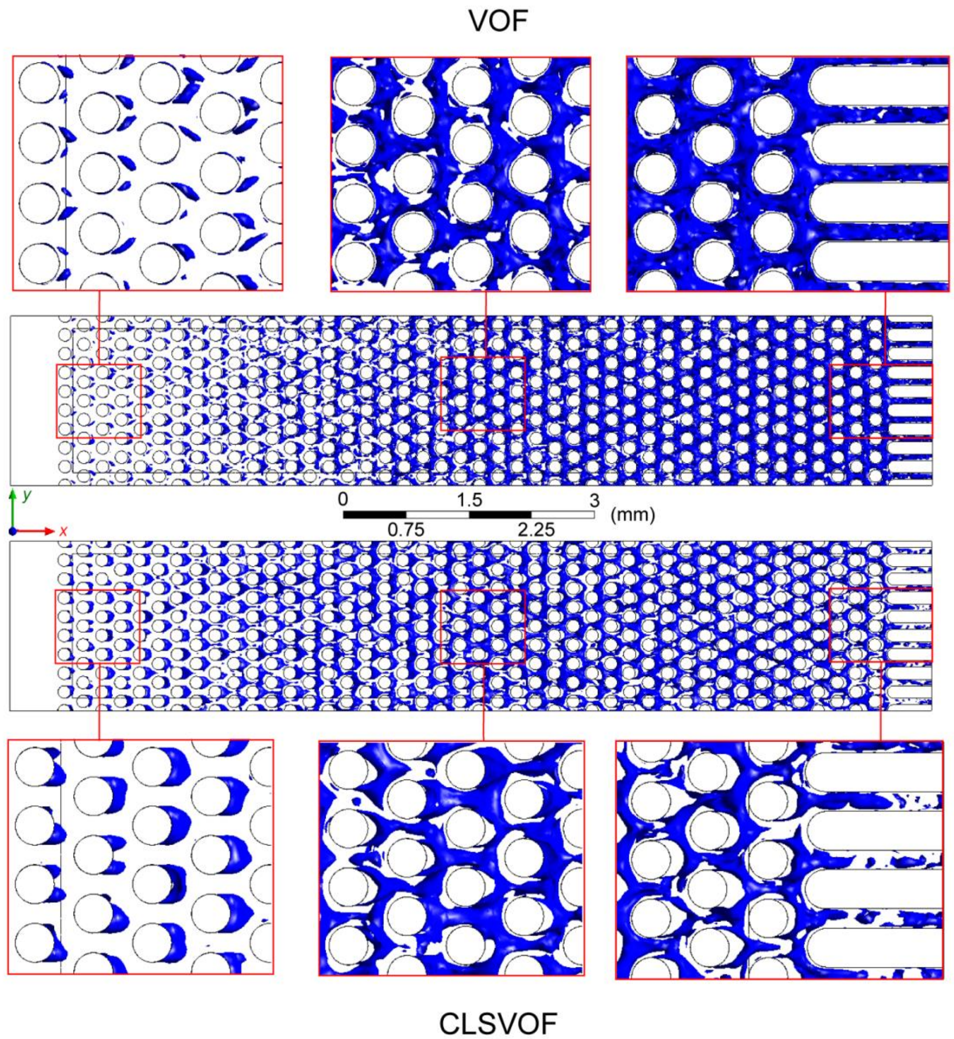

Figure 6.4 – Comparison of the evolved two-phase flow regimes (*t* =10 ms) in the silicon microgap predicted by the VOF and CLSVOF models for a mass flux of 1000 kg/m^{2}s and a heat flux of 100 W/cm^2. The blue surface indicates the liquid-vapor interface as seen from a top view (+*z*).

When comparing the mid-section details between both solutions (where there is a considerable amount of vapor due to buildup), it is observed that the VOF solution is formed by a set of vapor blobs varying in shape and size, and that the interface resolution is somewhat distorted. In contrast, the CLSVOF solution is capable of providing a significantly better interpretation for the same problem through smoother vapor films that continuously break up at the front pins and remerge as they flow downstream. Such features are possible through the use of the LS function, which is continuous across the interface and helps for improved interfacial reconstruction and therefore, a more accurate surface tension calculation than the standard VOF method. Regarding the outlet section, it may be noted that with the VOF solution the section is nearly occupied in its entirety by vapor, while the CLSVOF technique handles the breaking and merging of vapor structures in a more physical mode.

6.8 Bubble nucleation in pin fins

In the present section, the bubble nucleation and detachment are discussed for a region of pin fins in the three first columns of the microgap since vapor buildup is not significant here and allows a better interpretation of this mechanism and its representation. It is also important to remark that the present type of modeling has a number of advantages for the detailed analysis of two-phase flow, such as the three-dimensional representation of the liquid-vapor interface with access to any point within the computational domain. The CFD results for two-phase flow were post-processed with the software ANSYS® CFD-Post® 15.0, which allowed the representation and tracking of the interface in a variety of useful ways. Figure 6.5 shows a set of detailed views for a selected array of pin fins near the inlet section for analyzing the different predictions for bubble nucleation between both studied methods. In order to facilitate the interpretation of results, the isometric view and top view of the liquid-vapor interface for an array of 8 upstream pin fins is shown; a top view of the cross-section plane that depicts the volume fractions contours is also included, where the red color denotes the vapor phase, the blue color corresponds to the liquid phase, and the in-between range of colors indicates the interface.

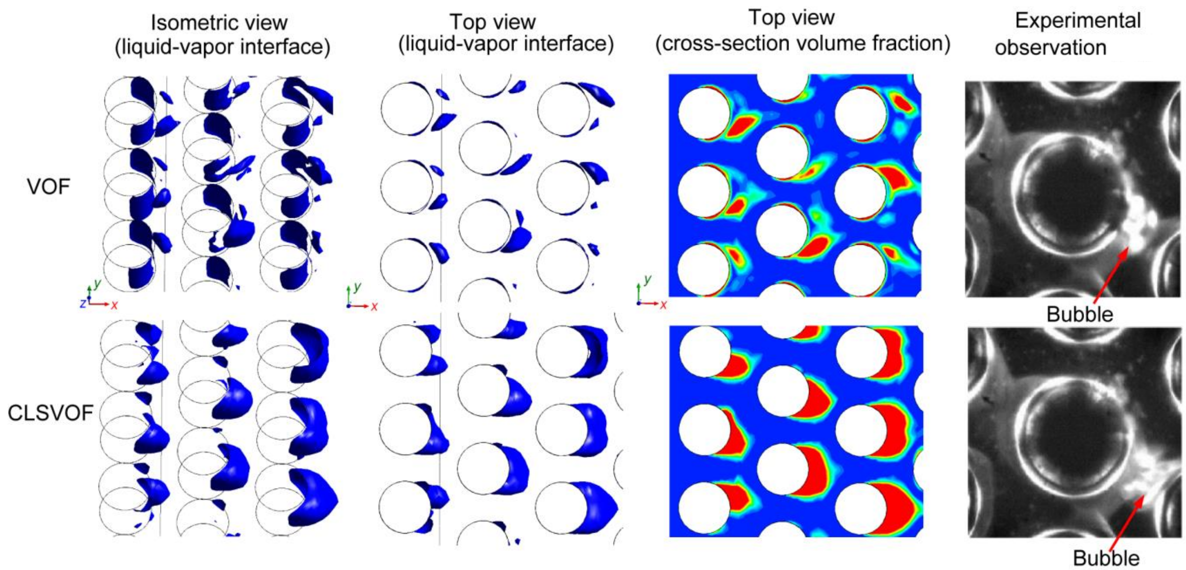

Figure 6.5 – Comparison of the bubble nucleation process at upstream pin fins.

It is noted that there are important differences between the VOF and CLSVOF solutions; the isometric view for the VOF case shows that the bubbles are nucleated and detached from thin vapor films that originate approximately 90° from the stagnation point of the pin fins. There is also some bubble breakup into slightly distorted shapes, which may be attributed to the discontinuous VOF function across the interface and its impact on the surface tension calculation. In contrast, the CLSVOF solution provides a different representation in which bubbles form at the rear part of the pin fins and eventually detach as they grow and are removed by the surrounding flow; the interface curvature is considerably better resolved recalling that both solutions were obtained with the same mesh size and settings. The predicted behavior of bubble growth and detachment is found to be in agreement with the experimental observations reported by Isaacs [63], who investigated the two-phase flow features of R245fa in a silicon microgap with a similar arrangement. The points with the lowest pressure in a cylindrical pin fin array correspond to those where boundary layer separation occurs, which for laminar flows is approximately 90º from the stagnation point; these points also have the lowest saturation temperature condition and hence promote bubble nucleation at wall crevices in the experiment. A similar process is approached by the implemented CFD model, where these flow field conditions are also predicted and hence promote the bubble nucleation at computational cells in the solid-fluid interface meeting the phase-change criteria.

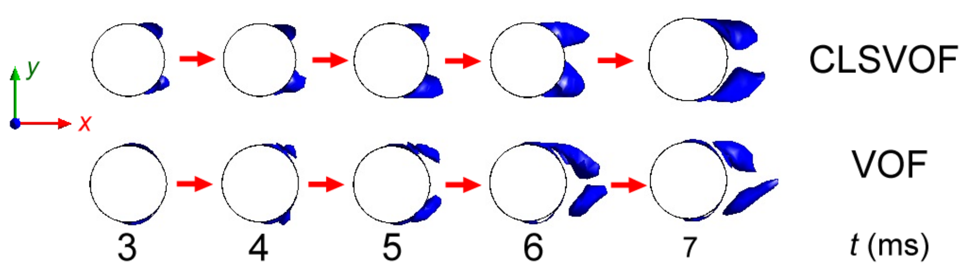

Figure 6.6 – Comparison of the bubble growth process at one of the upstream pin fins.

Isaacs [63] reported that vapor bubbles originated at the mentioned location, and then these were moved due to inertial forces to the recirculation zone (rear part of the pin fin, at 180º from the stagnation point), growing to sizes up to 50 – 75 μm before detachment. The last column of Fig. 5 depicts the bubble nucleation mechanism observed by [63], which is comparable to the predictions by the CLSVOF model. In support to this discussion,

Figure 6.6 shows a comparison of the transient bubble growth process at one of the pin fins adjacent to the flow inlet (upstream). It can be observed that under the same mesh and operating conditions, the CLSVOF model predicts sharper bubbles than the standard VOF model, where the interface resolution and surface tension calculation negatively impact with an early bubble departure and distortion.

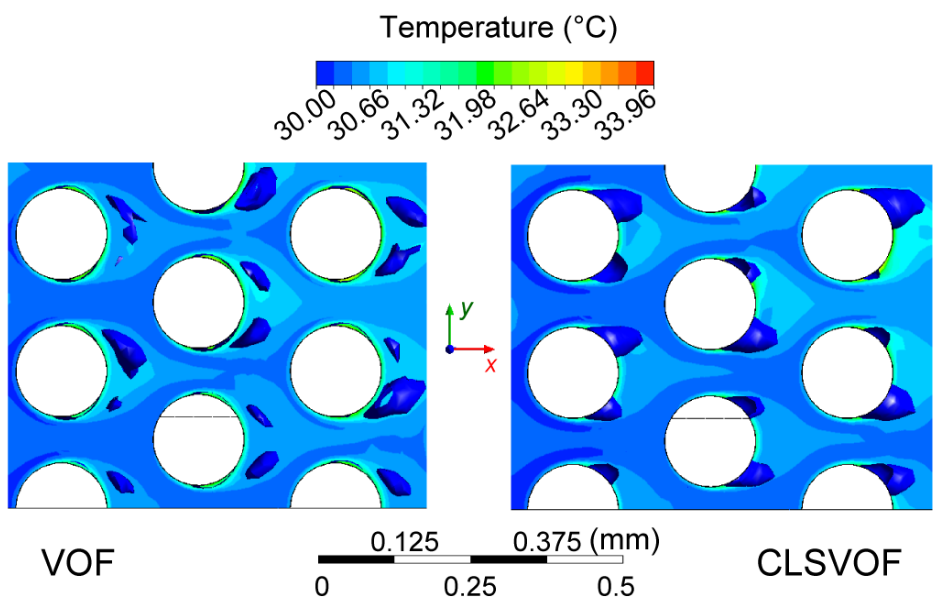

Figure 6.7 – Fluid temperature field (°C) in a cross-section plane for an array of upstream pin fins.

It was mentioned in Section 5.2 that for the implemented phase-change model, bubble nucleation occurs in the fluid-solid interfaces that exceed the saturation condition. However, for the case of flow boiling in a silicon microgap, vapor generation actually comes from pre-existing vapor nuclei at the crevices of the solid surface (heterogeneous nucleation), which requires some degree of liquid superheat to the onset of bubble nucleation. Figure 6.7 depicts a zoom-in comparison of the temperature field (cross-section contour) around an array of pin fins, in an upstream location of the microgap, at a flow time of 6 ms for both analyzed methods. It can be observed that the liquid is superheated (T > T_{sat}) in the fluid periphery and wake zone of the pin fins, with the bubble nucleation process that has been discussed.

6.9 Temperature distribution

Recalling that thermal control is one the ultimate objectives sought through this type of modeling, the present section is devoted to discuss the implications on the temperature field solution by using the two described methods in this chapter.

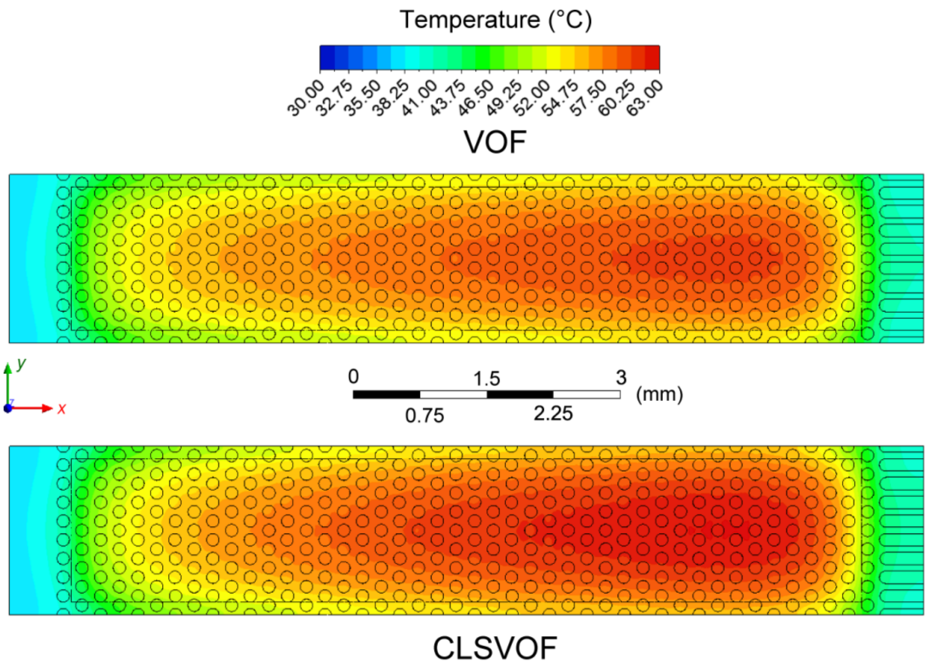

Figure 6.8 – Comparison of the temperature contours (°C) regimes (t = 10 ms) in the silicon microgap predicted by the VOF and CLSVOF models for a mass flux of 1000 kg/m²s and a heat flux of 100 W/cm².

Figure 6.8 depicts the predicted temperature contours by the VOF and CLSVOF techniques for the quasi-steady state solution at t = 10 ms, where the temperature contours (displayed at the bottom surface of the microgap) look similar in terms of the qualitative behavior. However, recalling that the implemented phase-change model includes a source term for the energy equation that is directly proportional to the vaporization rate, it is expected a difference between both approaches due to the described two-phase flow features in previous sections.

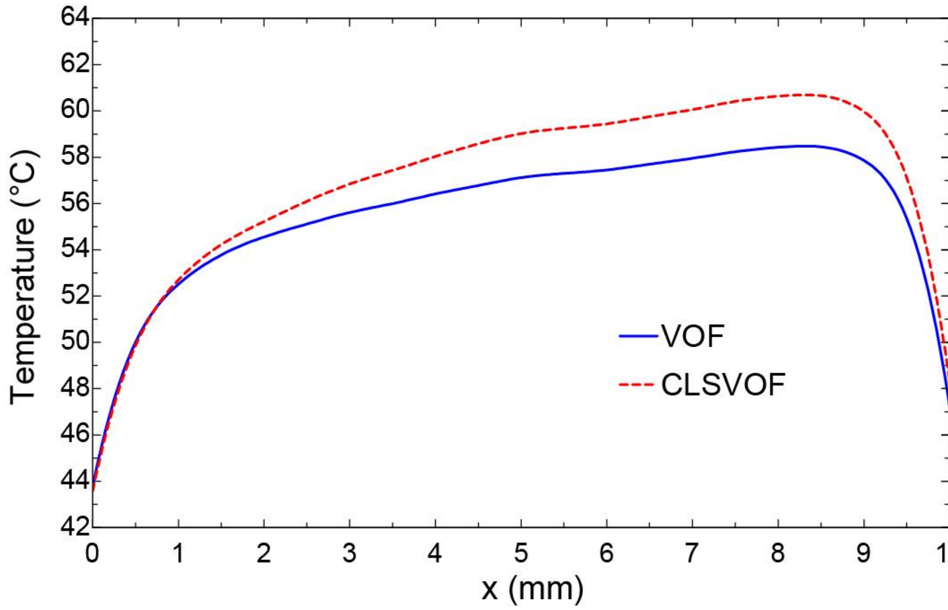

Figure 6.9 – Comparison of the average temperature variation at the bottom surface between the VOF and CLSVOF methods.

In order to provide a quantitative comparison of the predicted temperature field by both methods, Figure 6.9 shows a plot of the average temperature variation for each case across the heated area of the computational domain; the average temperature is plotted by equally dividing the heated area into 20 zones in the *x*-direction. It is observed that both solutions are in agreement until the first millimeter of heated length, and after that the CLSVOF method predicts higher temperature values than its counterpart; this discrepancy is attributed to the interfacial reconstruction and tracking capabilities of each method. The fact that temperature curves depart in the downstream regions is consistent with the higher amounts of vapor-phase predicted by the VOF method as discussed in Section 6.1 for Figures 6.3 and 6.4, which therefore provide a larger interfacial area and energy sink through the defined source terms. This behavior is related to the intrinsic capabilities for curvature resolution of these techniques, which dictate the surface tension calculation and how the vapor structures form, break up and interact in the computational domain. The largest temperature difference between both methods occurs near the outlet section, where the vapor amount difference is the highest; the steep temperature decrease is due to the heat spreading to the non-heated zones after the cylindrical pin fin section.

6.10 Pressure drop

The variation of the two-phase pressure drop as a function of time was also assessed for both techniques and it is plotted in Figure 6.10. The two-phase pressure drop is calculated as the difference in the mass-flow-weighted average pressure values between the inlet and outlet sections. As expected, the pressure drop increases as vapor structures are formed within the microgap, and follows this trend in a non-linear fashion as the two-phase flow regime evolves. The plotted data is consistent with the discussed results of Figure 6.3, where vapor continues to build up until the point that it is balanced by the surrounding flow conditions leading to vapor evacuation. After t = 5 ms, the pressure drop begins to stabilize for both methods, and hence it is assumed that the two-phase flow regimes is evolved. Noting that the pressure drop values oscillate due to the continuous generation/evacuation of vapor structures, a mean value is achieved at the so-called quasi-steady state. The mean pressure drop for the evolved two-phase flow regimes is 161.88 kPa and 161.58 kPa for the VOF and CLSVOF methods, respectively. Although both values are very similar, a difference in behavior should be noted between both techniques, where the CLSVOF solution presents larger pressure drop oscillations than the VOF results. This is again associated to how both methods reconstruct the vapor structures and the corresponding calculation of the surface tension forces.

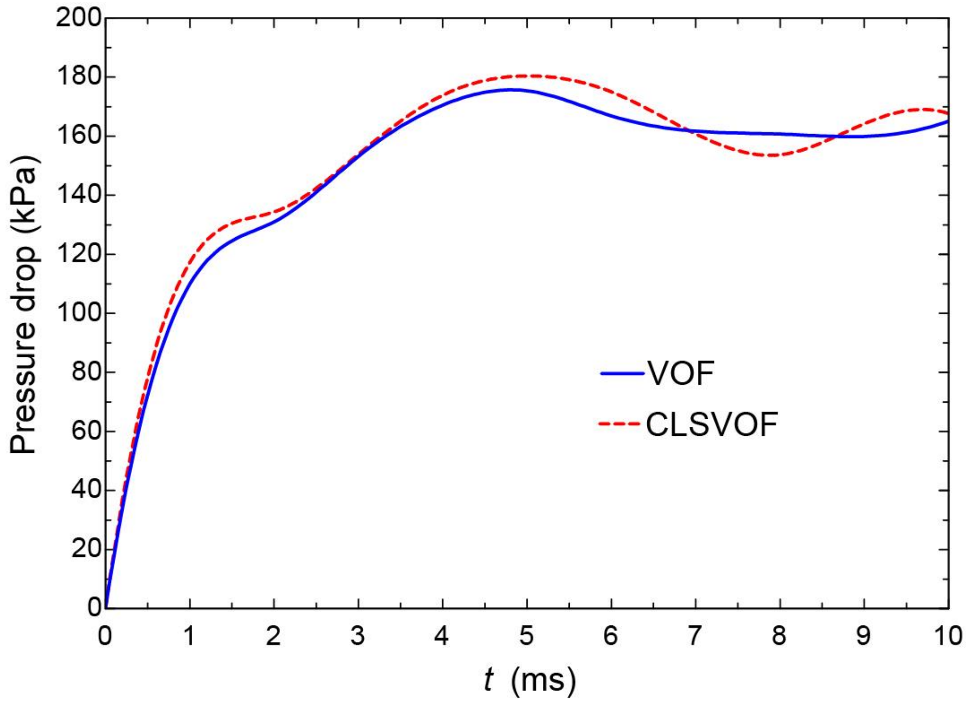

Figure 6.10 – Comparison of the two-phase pressure drop variation as a function of flow time between the VOF and CLSVOF methods.

6.11 Remarks and conclusions

In this chapter, the VOF and CLSVOF methods were been coupled to the mechanistic phase-change model for the analysis of the flow boiling behavior in a portion of the TDV silicon microgap. The main features and capabilities from each technique have been discussed, and the results for a case with fixed operating conditions have led to conclude that the CLSVOF technique offers a significantly better interface reconstruction to simulate the physical behavior of the problem. The main advantage of using the LS function, continuous across the interface, is the capability of predicting smoother interfaces and therefore a more accurate surface tension calculation, which is of critical importance in microscale two-phase flows. The bubble nucleation process for both techniques was discussed and compared to experimental observations from the literature for a similar case, observing the early breakup of bubbles and its distortion for the standard VOF model due to surface tension calculation issues. In contrast, the CLSVOF offered a better interpretation of this process and a reasonable agreement in the qualitative behavior of the experimental reports.

The presented results provide evidence of the capabilities to model flow boiling in a relatively complex domain with a number of pin fins for relevant microscale applications, such as the 3D-stacking of ICs. This type of modeling may lead to a better understanding of this phenomena and its optimization for enhanced thermal control in emerging technologies. The progress from this chapter in the development and refinement of the presented flow boiling model allows the advancement toward the most challenging part of the present thesis work in both fundamental and applied aspects, and the most relevant results and implications will be discussed in the next final chapter.

CHAPTER 7. FLOW BOILING IN SILICON MICROGAPS WITH VARIABLE PIN FIN CLUSTERING AND HOTSPOTS: NUMERICAL AND EXPERIMENTAL DEMONSTRATION

The present chapter brings closure by engaging all of the relevant findings and acquired skills through the development of this dissertation to achieve the ultimate task of assessing, both numerically and experimentally, the two-phase flow cooling characteristics of the TDVs designed for vertical integration and variable pin fin clustering. Emphasis is given to this final chapter as it represents, to the best of the author’s knowledge, the first experimental demonstration of flow boiling thermal management in a silicon microgap with variable pin fin clustering for addressing hotspots in a relevant mode for the vertical integration of ICs. Besides demonstrating such practical features with the comprehensive design of the TDV, the remarkable prediction capabilities of the proposed CFD-HT model will be demonstrated for very complex cases in which the two-phase flow regime, temperature distribution and two-phase pressure drop are in excellent agreement with the experimental measurements of non-trivial temperature profiles under variable heating conditions. As it was indicated at the beginning of this dissertation, the numerical modeling of such phenomena in these cases is a relatively unexplored area due to a number challenges; therefore, the direct validation of this model constitutes a key advance for the detailed thermal design and optimization of complex microgap cooling layers for two-phase cooling systems.

7.1 TDV design and experimental methods

For the present investigation, one of the main conclusions from Chapter 4 is taken into account here in the sense that main attention will be given to the TDV design with local pin fin clustering shown in Figure 3.1 and 3.5a. The increased pressure drop incurred by a spanwise constriction of fins impacts more negatively the overall performance than the slight flow bypass effect in a local clustering design.

Regarding the experimental procedure please refer to Chapter 3, in which a very detailed discussion is given around the development of the flow loop, components and methods for acquiring data. The dielectric refrigerant HFE7200 is used as the coolant, employing the full characterization capabilities of the experimental setup shown in Figures 3.10 and 3.11.

7.2 Numerical model

The interface tracking for the flow boiling modeling was approached with the Coupled Level Set Volume of Fluid (CLSVOF) method and the description for its implementation given in Chapter 6, including the meshing technique.

Findings from the previous two chapters have indicated that the modeling of flow boiling results in a relatively complex challenge due to its transient nature and associated computational requirements, such as mesh size and time step restrictions in explicit formulations. Hence, only a representative section of the microgap is modeled, which has enough extension in the transversal and longitudinal directions to capture the relevant physics of boiling in the TDV (as demonstrated in the results section). Figure 7.1 depicts the computational domain used for the analysis of the two-phase cooling in the TDV, indicating the relevant dimensions such as the active heated length of 10 mm, the inlet and outlet sections with 0.5 mm length (for numerical convergence), and the width of 2.025 mm that includes the hotspot area and surrounding background pin fins. The non-conformal meshing details are also depicted, in which the same settings as those described in Section 6.5 were used.

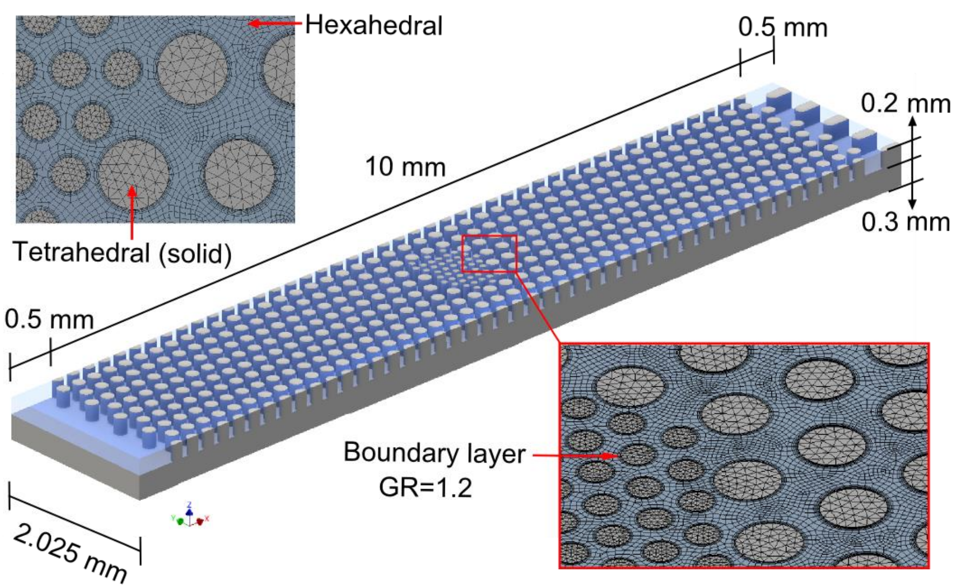

Figure 7.1 – Schematic of the analyzed computational domain and its relevant dimensions and features.

Regarding boundary conditions, heating is modeled as a heat flux surface condition in each of the background and hotspot zones at the bottom of the TDV, as it was indicated in Figure 3.3 showing the bottom layout of the TDV. The side surfaces of the computational domain are modeled as symmetry boundaries, whereas the remaining exterior surfaces are prescribed with adiabatic boundary conditions. The background heating zones 1 to 4 are defined with a heat flux value of q_B'' = 32 W/cm^2 (which comes from the effective value used in the experimental conditions), while the central hotspot was subjected to a range of heat fluxes (q_{HP}'') from 0 to 150 W/cm^2. The flow inlet for the computational domain was prescribed with a mass flow rate of 2.66 × 10^{-4} kg/s, which corresponds to the 60 mL/min of the dielectric refrigerant HFE7200 used in the experimental tests. The inlet fluid temperature is 81°C, which is the saturation temperature of HFE7200 observed in the experimental measurements corresponding to an inlet pressure of 365 kPa. The internal walls that act as the fluid/solid interface were prescribed with non-slip and temperature continuity boundary conditions. The thermophysical properties of silicon and HFE7200 used for the corresponding modeling are listed in Table 7.1.

Table 7.1 – Thermophysical properties of silicon, liquid HFE7200 and its vapor at T_{sat} = 81 °C.

Property	Symbol	Silicon	HFE7200 (liquid)	HFE7200 (vapor)
Density (kg/m^3)	$\rho_{si}, \rho_l, \rho_v$	2330	1325	10.13
Thermal conductivity (W/m-K)	k_{si}, k_l, k_v	Eq. (32)	0.07966	0.01436
Specific heat (J/kg-K)	c, c_{pl}, c_{pv}	712	1333	972.2
Dynamic viscosity (Pa-s)	$-, \mu_l, \mu_v$	--	3.79×10^{-4}	1.035×10^{-5}
Surface tension coeff. (N/m)	σ	--	0.01299	

The numerical procedure corresponds to the description given in Section 6.4, using the same high-performance-computing (HPC) cluster and solver software. The solution was also initialized with the same procedure described in Section 6.6, in which the single-phase, adiabatic flow field is calculated with the fluid at the saturation condition, and once the solution is converged this data its used as the initial conditions before coupling the phase-change model and activating the non-uniform heating conditions.

7.3 Two-phase model validation

Figure 7.2 undoubtedly represents one of the most important plots (in addition to Figures 4.2 and 4.3) in the present dissertation, as it reports the two-phase model validation with the experimental data generated for the flow boiling of the dielectric refrigerant HFE-7200 in the TDV with the local clustering design, whose geometry and non-trivial layout may be recalled in Figure 3.1.

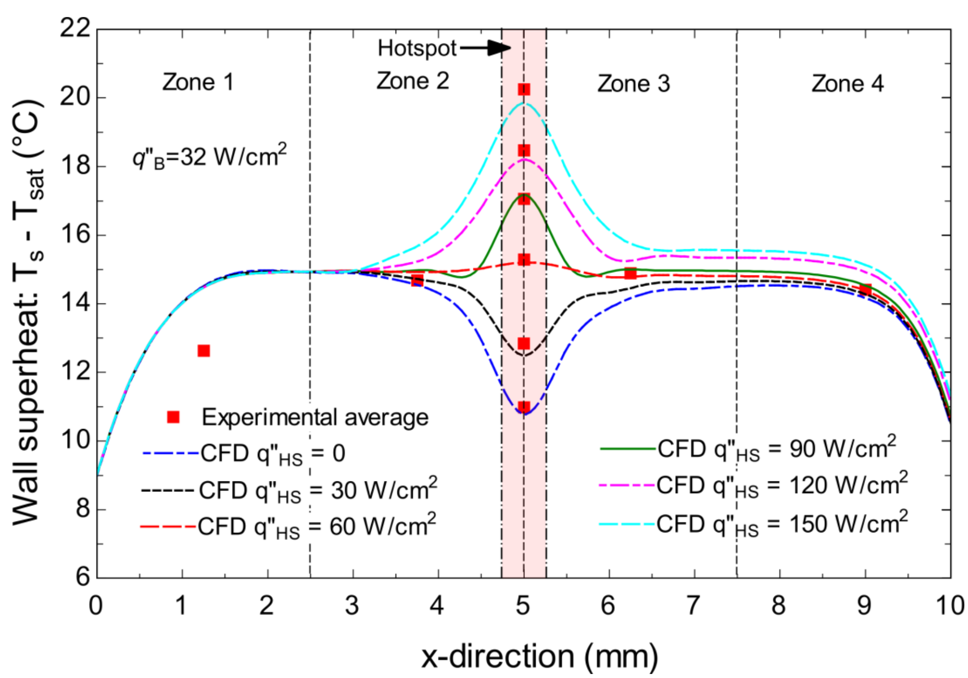

Figure 7.2 – Validation of the two-phase CFD-HT model with experimental data for local clustering TDV with a background heat flux of $q''_B = 32$ W/cm^2, hotspot heat fluxes ranging from $q''_{HP} = 0 – 150$ W/cm^2, and flow rate of 60 mL/min.

The plotted continuous curves in Figure 7.2 represent the model results for the temperature variation along a centerline (y = 5 mm) in the flow direction that crosses the hotspot zone, with the values plotted for the corresponding 10 mm long active heated zone depicted in Figure 3.3. The red dots represent the average experimental temperature returned by each of the platinum RTD heaters in the silicon TDV, recalling that such can only return a finite value and therefore modeling represents a significant advantage for more detailed assessment. The modeling results are in very close agreement with the experimental measurements, with a remarkable capability to predict the temperature jumps at the hotspot area for all of the analyzed cases. Unlike single-phase cooling, where the sensible heat mechanism leads to mean fluid and surface temperatures increase in the downstream direction, for the present cases of two-phase cooling under saturated conditions it can be observed that the average background zone temperature remains nearly constant at a wall superheat of approximately 15 °C, where the spikes in the plotted curves only happen near the inlet and outlet plenums due to heat spreading, and of course at the hotspot section depending on the heat flux input. Among all the measured experimental values and runs, the temperatures recorded by the RTD heater in zone 1 (near to the inlet plenum) were the only values in which the numerical prediction did not show a remarkable match; this could be due to a number of factors such as, RTD calibration, model simplified geometry, etc. However, the main factor is the experimental setting that is very difficult to adjust for the case of flow boiling; it was detected that near to the inlet pin fins some of the zones still presented single-phase characteristics and this could be the reason of the slight temperature discrepancy. Despite this minor detail, the prediction capabilities of the model are still very encouraging.

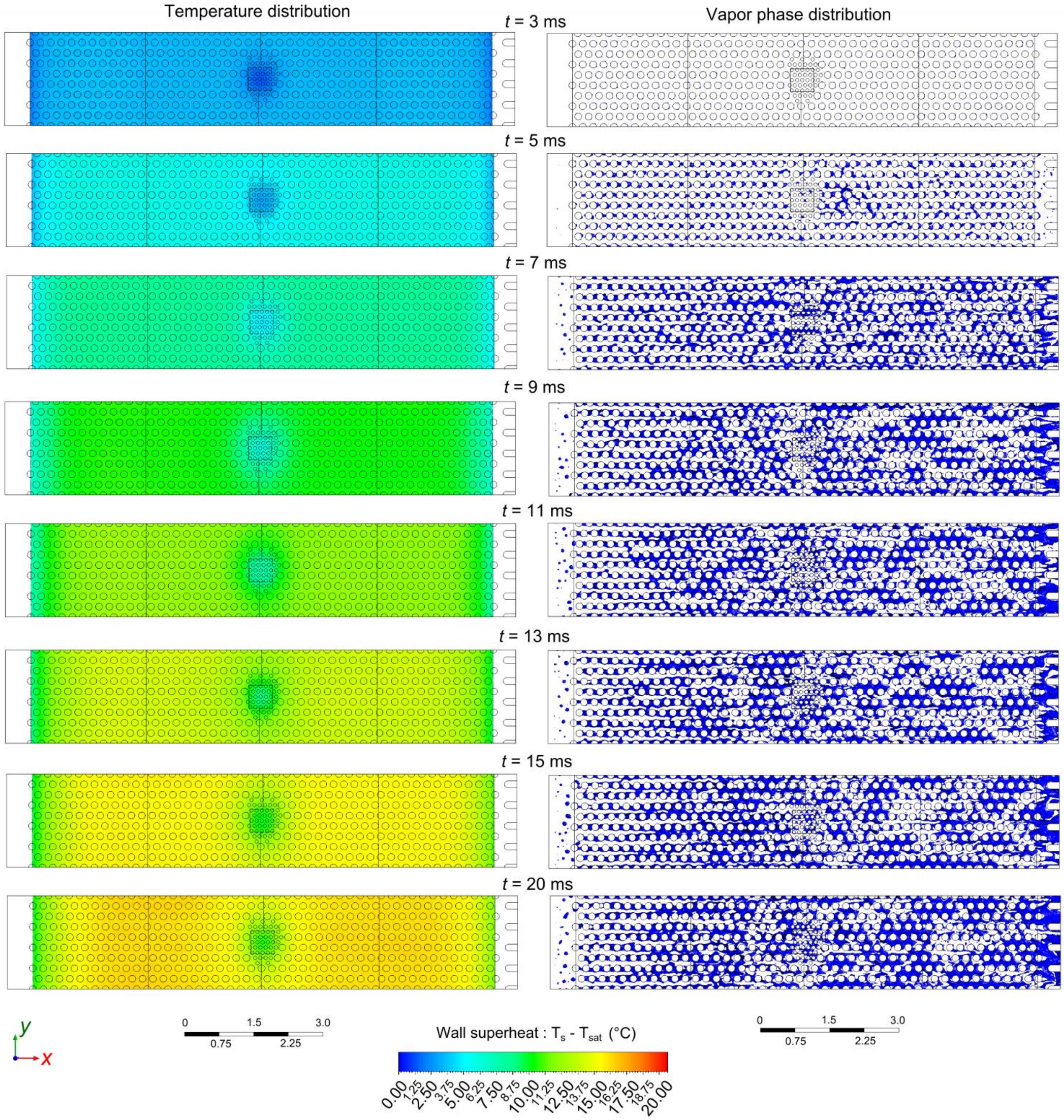

Figure 7.3 – Time evolution of the temperature and vapor phase distributions for the local clustering TDV with a background heat flux of q''_B = 32 W/cm^2, hotspot turned off (q''_{HP} = 0), and flow rate of 60 mL/min.

In order to better describe the interesting transient behavior of the analyzed cases (and taking advantage of the great level of detail the modeling results can provide), Figures 7.3 and 7.4 depict the phase and temperature distribution at different time steps of the numerical solution for selected cases. The time evolution depicted in Figure 7.3 corresponds to the case in which the hotspot is turned off (q''_{HP} = 0) while the background heaters are operating at the uniform value of 32 W/cm^2. Recalling that the simulation is initialized with the adiabatic flow field solution, the solid domain begins to elevate its temperature once the heating boundary conditions are activated and vapor bubbles start to nucleate at the rear part of the pin fins since these constitute the points of lower pressure due to the boundary layer separation, and by also having the lowest saturation temperature these promote the vapor generation; increased zoom-in to the vapor distribution subset corresponding to t = 3 ms shows the initial generation of such structures. At the next selected time step at t = 5 ms, it can be observed how the vapor phase distribution is significantly more noticeable and evolved, in which the vapor structures can be easily noticed at the stagnation points behind the pin fins; temperature on the silicon domain is also slightly higher with a sink at the center due to the prescribed conditions and increase in surface area resulting in a spreading behavior in its periphery. For the subsequent time step at t = 7 ms, the two-phase flow regime is considerably evolved and it can be noted how the vapor structures merge downstream, forming different churn-type regimes before exiting the domain. Regarding its temperature distribution, a similar behavior to the previously described time step persists with the only difference of an offset in wall superheat values. Once these trends have been detected, an important observation is that for subsequent time steps the two-phase flow regime preserves its general form, indicating a balance between vapor generation and removal rates and therefore reaching to its quasi-steady state. Regarding temperatures, it can be noted on the left column how the contours keep increasing their distributed values in wall superheat as a function of time but maintaining noticeable temperature uniformity across the silicon microgap as a result of using the latent heat of vaporization. Maintaining the device at a uniform temperature is undoubtedly one of the sought features for enhanced reliability as it is well known that high temperature gradients can induce stresses in the silicon structure and lead to eventual failure. As the time evolves the temperature changes diminish from time step to another, until reaching the so-called quasi-steady state value in which the flow field variables are stabilized.

Figure 7.4 depicts the corresponding transient behavior for the case in which the hotspot heat flux is nearly 3x times the value of background heating (q''_{HP} = 90 W/cm^2), with the main purpose of demonstrating the capabilities of the TDV and its local clustering design to handle power non-uniformities in two-phase cooling operation with dielectric coolants. At the first selected time step of t = 3 ms, it can be noted on the right hand side subset that the vapor starts being generated more intensely at the hotspot area due to its higher temperature when compared with the background zones. Contrary to the previously described case, for this case of augmented heat flux the temperature spreads outwards as indicated by the periphery around the central hotspot, while still conserving the temperature uniformity in the background zones due to the fixed heat flux and two-phase cooling effect. For the time step at t = 5 ms, more vapor is present inside the microgap as the bubbles start growing and it can also be noticed that right after the hotspot region, a larger amount of vapor is present due to the more intense boiling at such zone. The beneficial effect of having a localized increase in heat transfer area can be noted as the temperature difference between such zone and the surrounding background areas is approximately only 2 °C; such offset is maintained through the entire temperature evolution of the TDV.

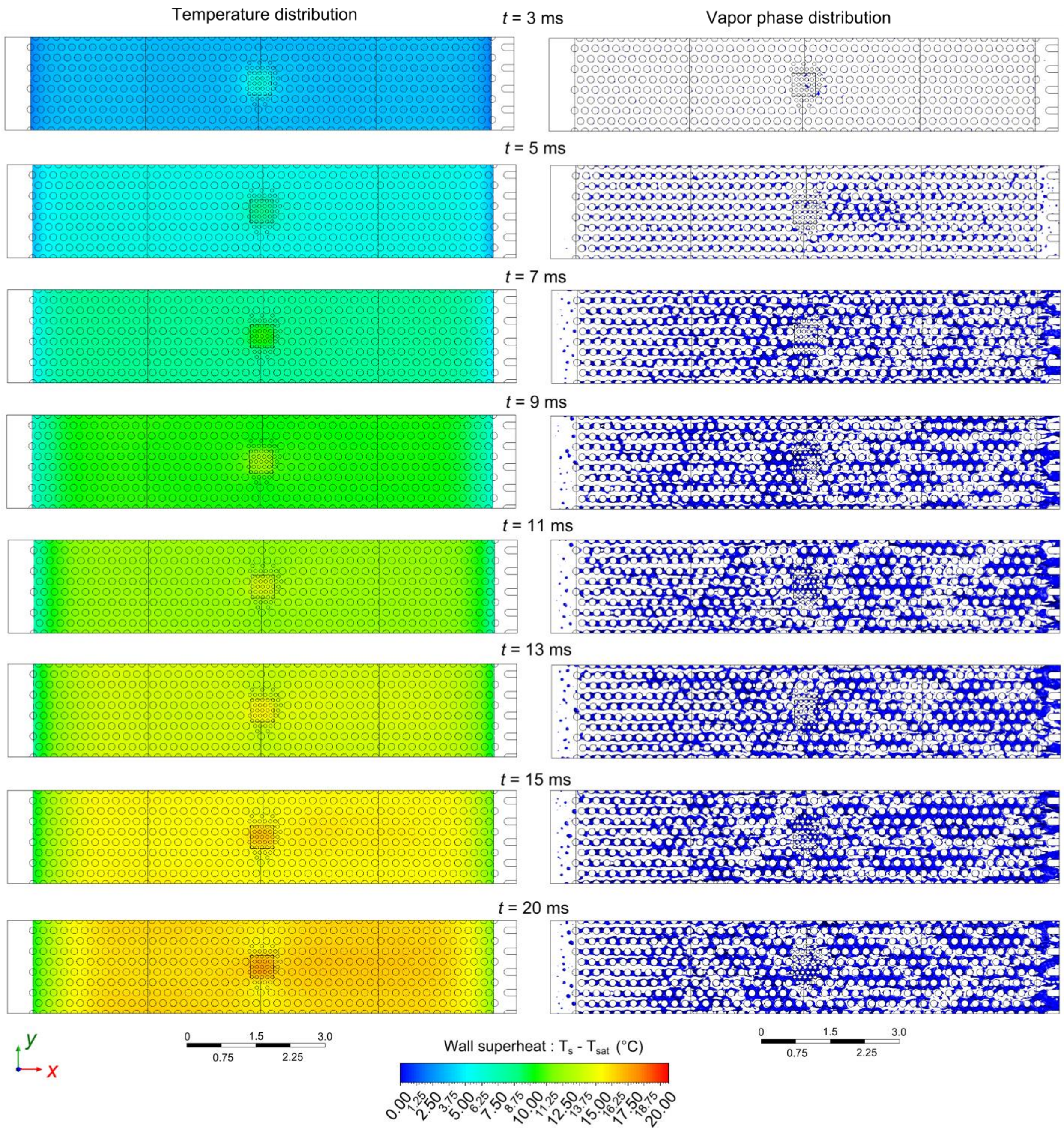

Figure 7.4 – Time evolution of the temperature and vapor phase distributions for the local clustering TDV with a background heat flux of q''_B = 32 W/cm^2, hotspot heat flux of q''_{HP} = 90 W/cm^2, and flow rate of 60 mL/min.

Regarding two-phase flow regime evolution, it is noted that after 7 to 9 ms of two-phase flow, the vapor distribution displays a very similar state to the previously described case as a result of reaching the vapor generation/removal equilibrium; at such point there is not a noticeable effect of the hotspot on the two-phase flow regime and for all of the analyzed cases it looks virtually the same. Another thing to be noted is that the background heating zones display very similar behaviors across the different analyzed cases, in which the central hotspot heating impacts only the periphery as a result of spreading, as well as the small downstream region; this can be qualitatively seen in the temperature contours of Figures 7.3 and 7.4, and it is quantified in the validation plot of Figure 7.2.

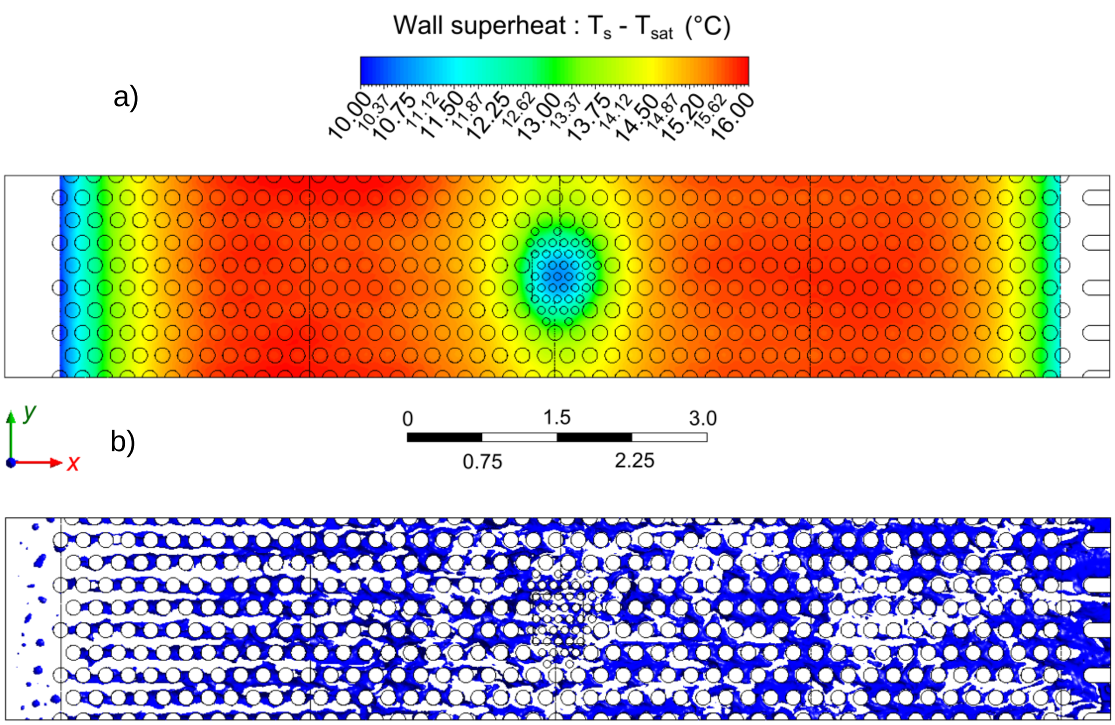

Figure 7.5 – Quasi-steady solution for the local clustering TDV with a background heat flux of q''_B = 32 W/cm^2, hotspot turned off (q''_{HP} = 0), and flow rate of 60 mL/min: a) temperature distribution, b) vapor phase distribution.

Figure 7.5 depicts the quasi-steady solution, predicted by the CFD-HT model for the TDV with the local clustering design, for the case in which the hotspot is turned off and therefore acts as a sink. The upper subset in Figure 7.5a shows the temperature distribution contour with a local scale in order to better visualize the gradients occurring for such combination of heat fluxes at 60 mL/min. Although the spreading is evident at both the central and inlet/outlet zones, it is important to recognize that the maximum temperature gradient for this case is as low as 6 °C, therefore proving the capability for such design and configuration for handling non-uniform power inputs. Figure 7.5b shows the two-phase flow regime distribution for the aforementioned case, where the vapor merging and its evolution are evident in the flow direction.

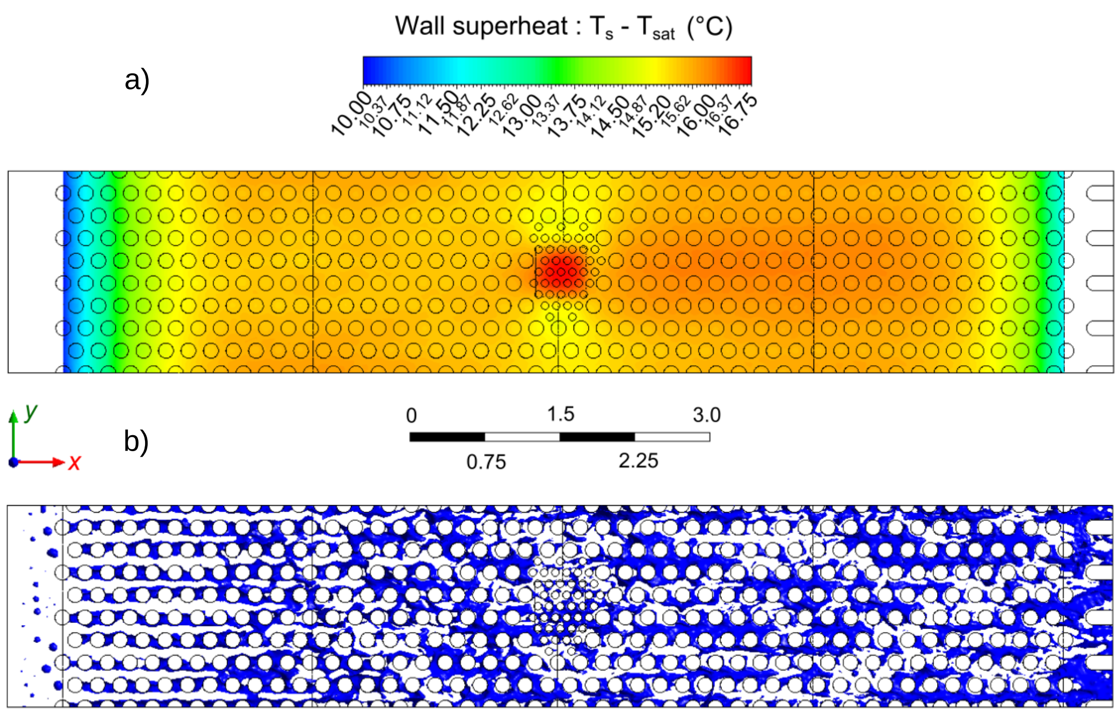

Figure 7.6 – Quasi-steady solution for the local clustering TDV with a background heat flux of q''_B = 32 W/cm^2, hotspot heat flux of q''_{HP} = 90 W/cm^2, and flow rate of 60 mL/min: a) temperature distribution, b) vapor phase distribution.

Figure 7.6 provides the details of the quasi-steady state solution for the case in which the hotspot heat flux is nearly three times higher than the background values (q''_{HP} = 90 W/cm^2); the temperature distribution contour in Figure 7.6a shows the detailed behavior of spreading around the hotspot, which is kept at a wall superheat of ~ 7 °C for this case. It can also be observed that the hotspot has a slight temperature increase effect on the background regions downstream its spanwise extension, which is quantitatively captured by Figure 7.2 and increases as the hotspot heat flux is higher. Figure 7.6b shows the vapor phase distribution in the quasi-steady state for this case, which is virtually the same for all of the analyzed cases as they evolve due to the dominant generated vapor volume in the background areas; the transient details of such process can be consulted in phase distribution subsets included in Figure 7.3 and its respective discussion in paragraphs above.

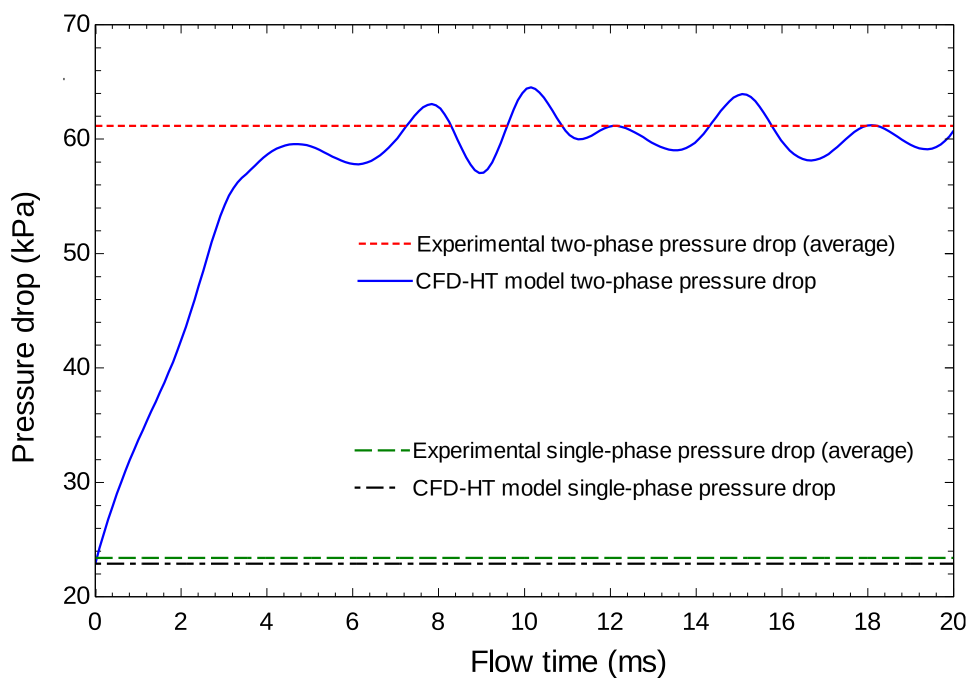

Figure 7.7 – Comparison of the single and two-phase pressure drops measurements in experiments and simulations with HFE7200 at 60 mL/min.

Once that the temperature prediction capabilities of the present CFD-HT model have been discussed in detail for a number of variations in the hotspot heat flux input and displayed a very good agreement with experimental measurements, another flow variable of interest is of course the two-phase pressure drop. For multi-phase operation, the required pressure gradient to move a liquid/vapor mixture of a pure substance from point to point is significantly higher than that required for single operation; this is due to the extra flow resistance added by the vapor phase, and there is vast literature documenting such phenomena (refer to the review in [28]). Despite a number of correlations have been developed for predicting the two-phase pressure drop behavior in different cases, most of these are empirical (or semi-empirical) and are very limited to predict only the cases and operating conditions from the experimental data they were tailored. For the present case of a relatively complex micro-cooling layer design with a variable density of pin fin structures, certainly none of these correlations are suitable and it is to be reminded that the present thesis works strives to provide a more accurate and detailed estimation through the use of the described multiphase models coupled with a phase-change model. For such purpose, Figure 7.7 depicts a very insightful chart comparing the behavior in both the single-phase and two-phase pressure drop measurements in experiments and corresponding predictions by the CFD-HT model. The plot was elaborated from data corresponding to experiments/simulations, using the coolant HFE7200 at a flow rate 60 mL/min, in adiabatic conditions at the saturation temperature of 81 °C for the single phase measurements and for the two-phase cooling measurements with the background heat flux of 32 W/cm^2 and hotspot heat flux in the indicated range from 0 to 150 W/cm^2. The single-phase operation and comparison is included due to the fact that this is the initialization point before the flow boiling occurs within the microgap due to heating, besides providing further validation to our models and techniques. The experimental, steady-state, single-phase pressure drop at saturated liquid conditions was measured with an average value of 23.41 kPa, whereas the CFD model prediction for the corresponding case resulted in a value of 22.88 kPa. The comparison of such initialization conditions is depicted in the two closely-spaced lines at the bottom of the plot; such lines are horizontal to indicate these correspond to steady state conditions. The solid blue line indicates the time evolution of the two-phase pressure drop calculated by the CFD-HT model, which can be noted to start from the single-phase value at time 0 (initialization case file) and steeply increase during the first 5 to 6 ms of flow boiling due to the gradual generation of vapor inside the domain until reaching the described quasi-steady state in which the vapor generation rate is balanced with the vapor removal rate from the domain; this curve is consistent with the description given for Figures 7.3 and 7.4, where it was indicated that the two-phase flow regime quickly evolves and maintains this fluctuating behavior within a close range. The red dotted line in Figure 7.7 indicates the experimental average of the measured two-phase pressure drop values at 61.15 kPa, where it can be noted that it falls very close to the predicted range by the CFD-HT model (which has an average of 60.63 kPa for values after 8 ms in the quasi-steady state). The fluctuation average for both the experiments and simulations was below a 5 kPa range, and the reason of not plotting the experimental fluctuation is because the data acquisition time scale was orders of magnitude larger than the simulation cases. Nevertheless, the presented results demonstrate both numerically and experimentally that both measurements have an excellent agreement and range in the same values.

Table 7.2 – Summary of the two-phase model validation with the corresponding TDV experimental data with HFE7200 at 60 mL/min.

		Average zone temperature				Hotspot temperature	Pressure drop
Background heating, q''_B (W/cm^2)	Result type	ΔT_{wz1} (°C)	ΔT_{wz2} (°C)	ΔT_{wz3} (°C)	ΔT_{wz4} (°C)	ΔT_{HP} (°C)	ΔP (kPa)
13	Exp.	4.15	4.91	5.29	5.98	3.06 – 8.05	55.35
	Model	3.95	4.12	4.95	5.36	2.79 – 7.85	54.64
32	Exp.	12.63	14.68	14.89	14.41	10.98 – 20.23	61.15
	Model	13.82	14.86	14.93	14.72	10.63 – 19.85	60.63

In order to summarize the previously discussed results, Table 7.2 lists a compact form of the comparison between experimental and numerical results for the TDV microgap at different heating combinations. It is to be noted that for all of the hotspot to background heat flux ratios, the overall effect on the average background zone temperature and pressure drop were found to be negligible due to the small area of the hotspot, therefore in Table 7.2 just the representative average value among all measurements is listed. A remarkable agreement is observed in the compared measurements/predictions for the wall superheat values for both background and hotspot zones (ΔT_{wz}, ΔT_{HP}), as well as the two-phase pressure drop (ΔP), therefore meeting one of the most important goals of the present dissertation.

7.4 Description of the two-phase flow regimes

The present section is devoted to discuss the experimental two-phase flow visualization with the high-speed camera (Phantom V11, VISION Research, Inc.) that was focused on the top glass surface of the TDV (see Chapter 3 for acquisition methods and details). Before running the two-phase cooling operation, all of the experimental runs were first stabilized under adiabatic single-phase conditions, and subsequently the pre-heater section was adjusted to elevate the refrigerant temperature near saturation conditions.

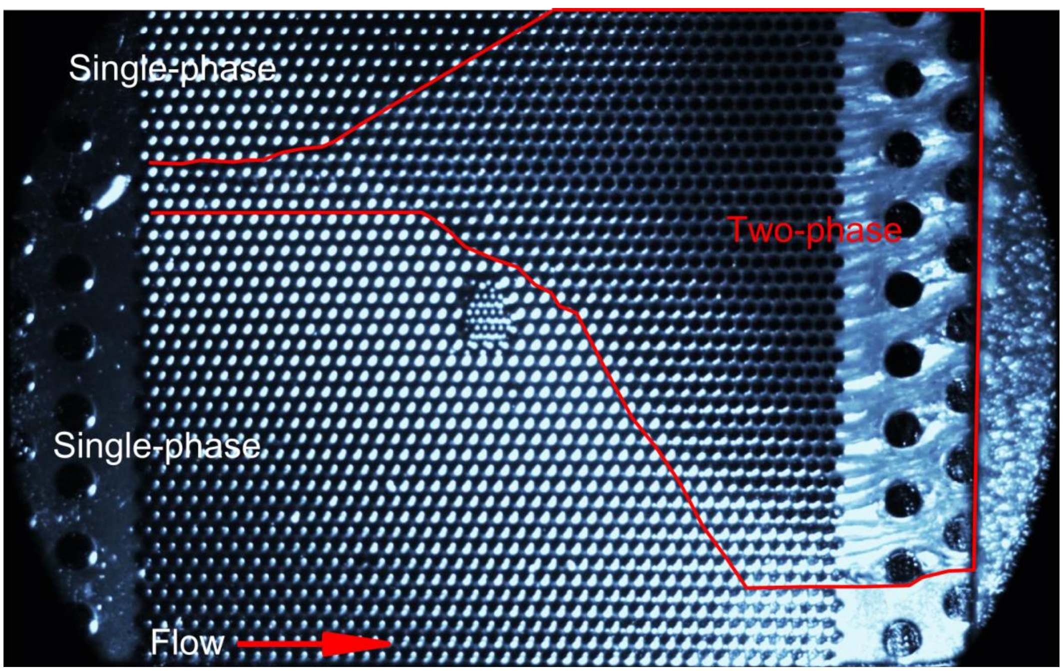

Figure 7.8 – Saturated flow boiling incipience in the TDV microgap for HFE7200 at a flow rate of 60 mL/min and adiabatic conditions.

When tuning the experimental operating conditions to reach the desired saturated conditions, it was observed that boiling conditions appeared in adiabatic cases, indicating that pressure drop across the microgap induced this premature boiling behavior as the saturation temperature of the moving liquid is reduced. Figure 7.8 depicts an example of the described conditions in which boiling originated at one of the inlet structural pin fins, triggering the conditions for an asymmetric two-phase flow distribution as shown by the red line separating it from the zones in which the flow remains in liquid phase. Such case is reported here just as an indication of how the boiling begins inside the microgap, due to the fact that once this condition is observed, it can be assumed that the flow is saturated at the given flow rate and pressure conditions.

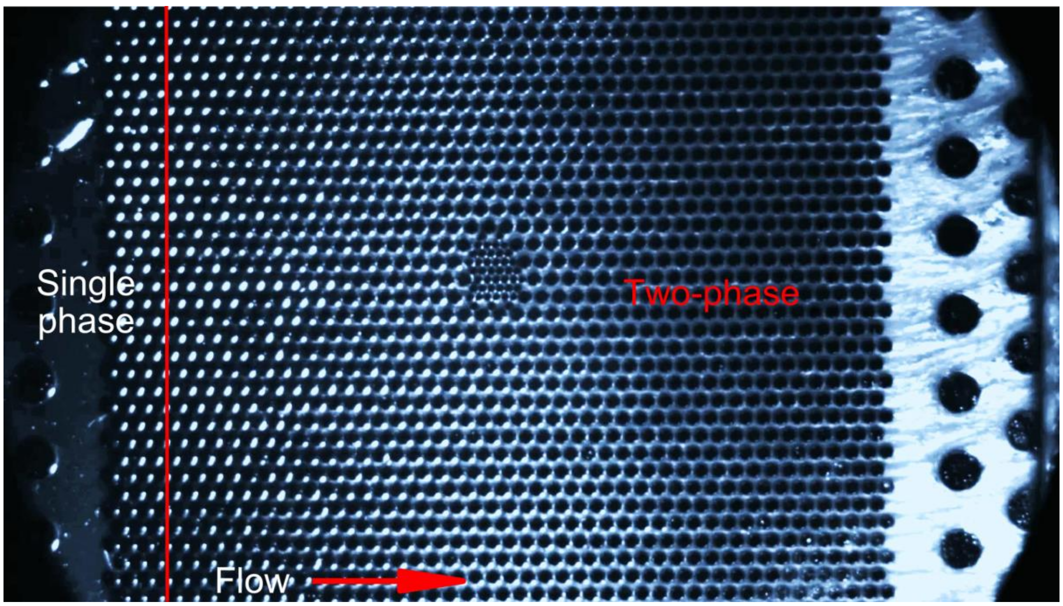

Figure 7.9 – Saturated flow boiling in the TDV microgap for HFE7200 at a flow rate of 60 mL/min, background heat flux of 32 W/cm^2 and hotspot heat flux of 150 W/cm^2.

After the described conditions of boiling incipience are observed, a gradual increase in the heating power is done for the corresponding experimental measurements, resulting in a homogenized two-phase flow regime inside the microgap TDV. Figure 7.9 shows a top view photograph of the silicon device operating under saturated flow boiling conditions, corresponding to the case in which the saturation temperature is 81 °C, and the background and hotspot heat fluxes are 32 and 150 W/cm^2, respectively. Unlike the case shown in Figure 7.8 for the asymmetric incipience conditions, once the heating conditions are stabilized, this power input induces a much more homogeneous behavior as shown in Figure 7.9. The red line indicates the separation between single-phase and two-phase flow conditions, where it can be stated that due to large amount of microscopic features inside the TDV it is difficult to discuss details of the two-phase flow features besides the identification of various vapor churn structures at the exit plenum.

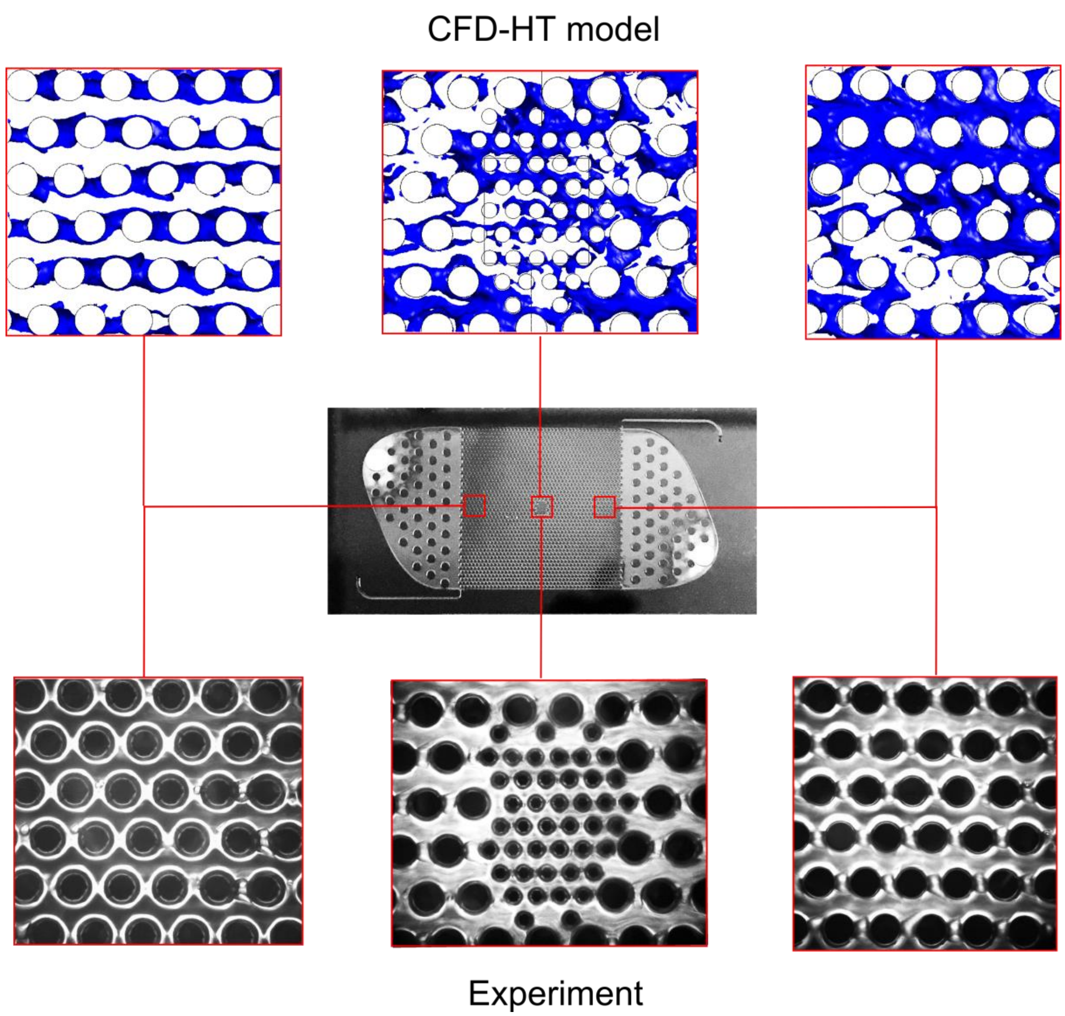

Figure 7.10 – Comparison of the two-phase flow regimes with high-speed-camera visualization and those predicted by the CFD-HT model.

In order to better analyze the two-phase flow regimes taking place inside the TDV, a magnification lens was coupled with the high-speed camera and focused on different sections, obtaining a higher resolution and detail of the vapor structures around multiple pin fins. Figure 7.10 shows a comparison of the different flow boiling behaviors at three selected locations in TDV, namely, at the inlet, hotspot and outlet sections. At the inlet section, it can be noted how the vapor structures are generated at the rear side of pin fins, which is in agreement with the discussion and explanation given in Section 6.8. Both the numerical and experimental results indicate the stagnation of vapor structures in the recirculation zones, which periodically grow until releasing high-speed vapor films, which are advected by the liquid in the adjacent flow lanes. One important fact to be pointed out, is that the two-phase flow visualization is limited by the different factors such as lighting, reflection and height focus, found to affect focusing on the vapor films or churns moving at lower heights in the microgap. As it can be noted in the detail window for the experimental two-phase visualization at the central hotspot, different vapor structures are seen at the recirculation zones following the previous discussion; however, the released vapor and merging at the flow lanes are not that easily identified due to the height differences and its fast advection velocity. In such type of cases, the three-dimensional CFD-HT results can be very valuable to provide insight regarding the vapor interaction and merging in the downstream direction, as the CLSVOF is capable to track such with a good resolution depending on the meshing settings. At the outlet section, more vapor is present due to accumulated effect from upstream regions, identifying that the rear part of the pin fins remains with stagnant vapor structures ending up in the churns flowing toward the outlet.

7.5 Remarks and conclusions

The results in the present chapter have demonstrated the flow boiling characteristics in a silicon microgap with non-uniform heating and a variable density of micro pin fins. The saturated flow boiling operation with the dielectric fluid HFE7200 resulted in nearly uniform temperatures across the microgap for different power conditions at a given flow rate, while the central hotspot zone was successfully increased up to 5 times the heat flux of the background zones. One important remark is that for the different experimental conditions tested, it was observed that the wall superheats fell in close proximity to a straight line for the hotspot to background heat flux ratios equal to a value of 2; such behavior confirms that the heat transfer coefficient remains nearly constant at the hotspot zone since both the heat transfer area and heat flux are doubled.

The refined CFD-HT model for two-phase cooling prediction was finally compared with the non-trivial thermal-hydraulic behavior observed in the experiments, observing a remarkable capability for predicting such with a high level of detail. The temperature jumps at the hotspot area were closely predicted as well as the relatively uniform temperature across the background zones due to the two-phase mode of operation. On the hydraulic side, the model was capable to predict with excellent agreement both the initial saturation conditions for pressure drop (single phase), as well as evolving as a function of time until reaching a quasi-steady state equilibrium in which dynamic two-phase pressure closely matched the average experimental values and range of dynamic variation.

CHAPTER 8. SUMMARY AND CONCLUSIONS

This chapter brings closure to the present dissertation by summarizing the most relevant findings and conclusions, recognizing the practical and fundamental contributions of this research and their relevance to the microelectronics community, and finally providing recommendations for future work.

8.1 Single-phase cooling in microgap layers for vertical IC integration

The research efforts for this part of the dissertation have demonstrated, both experimentally and numerically, the performance advantages of implementing the concept of variable pin fin clustering for the combined thermal management of heterogeneous heating conditions, which is the most common scenario in realistic microelectronic applications. The analyzed Thermal Demonstration Vehicles (TDVs) constitute a feasible approach to multi-tier thermal management due to their single inlet/outlet configuration with variable sizes and layouts of micro pin fins serving structural, thermal and electrical considerations. Relevant conclusions may be summarized as follows:

- A microgap design with pin fins allows the transversal flow interaction, resulting in beneficial effects such as downstream flow straightening even for configurations with asymmetric plenums; such behavior also results in a reasonably symmetric temperature distribution across the device.
- The objective comparison, both experimental and numerical, for the concepts of local and spanwise clustering smaller pin fin structures near the hotspot area has

demonstrated a relatively high flow restriction for the latter design with only a slight improvement in the local heat transfer at the hotspot.

- The effect of flow bypass is negligible on the thermal performance and therefore it is concluded that the local surface area for addressing hotspots should rather just be increased in the vicinity of localized zones with high heat fluxes; such action will also allow reducing the pressure drop across the device, and for a given pump curve in an operational system will therefore increase further the flow rate when compared to the spanwise clustering concept.

8.1.1 Technical contributions

One of the most relevant contributions from the present dissertation is closing the breach between experimental and numerical studies in this field, as it was detected that current literature focused on experimental testing often discards a deeper analysis and interpretation through modeling, whereas most numerical studies often fail to provide a relevant validation of their model and are limited to oversimplified designs. The described modeling framework was successfully demonstrated to provide a full-scale solution for the TDV conjugate heat transfer in single-phase cooling operation. The selected range of experimental data for this study was used to validate a detailed, physics-based CFD-HT model that was capable of predicting and providing fundamental insights into the problem, such as the complete three-dimensional temperature and flow field distributions including the entirety of the microstructure features inside the TDVs. The proposed framework was also found to constitute a valuable and cost-effective modeling technique since it does not require high-performance-computing capabilities. By consulting and following the procedures and guidelines given in Chapter 4, it is possible to analyze and predict the thermal/hydraulic response for virtually any type of heat flux distribution or power map, IC architecture, and operating conditions for a realistic and accurate design.

In addition, the corresponding studies for single phase cooling in this dissertation also provide a suggested benchmark simulation case consisting of a reduced computational domain featuring the variable density of pin fins above a hotspot; such effort is to provide a more accessible case for validation which can be easily reproduced by other researchers involved in the design of micro cooling layers for systems with highly variable power gradients.

8.2 Two-phase cooling in microgap layers for vertical IC integration

As it can be readily noted, the majority of research efforts and challenges of the present dissertation were targeted toward a better understanding of the two-phase cooling characteristics in the described TDVs for vertical integration of microelectronics. One of the big walls encountered in such development were the fundamental differences going from a relatively dominated steady-state single phase problem to a transient, two-phase operation. Jumping from the presented full-scale simulations to the flow boiling case was found to be a major challenge, due to the lack of applicable models for such conditions and the intensive computational requirements of multi-phase, transient problems at the microscale. Therefore, a gradual approach was taken in order to achieve the ultimate goal of being the first investigation of its type to demonstrate both numerically and experimentally the two-phase cooling characteristics in silicon microgaps with a variable fin density and hotspots. Relevant conclusions and findings from the dedicated chapters for the development of a two-phase cooling modeling framework may be summarized as follows:

- Coupling of the Volume of Fluid (VOF) for interfacial tracking with a mechanistic phase-change model based on the kinetic theory of gases may provide a plausible approximation for the assessment of boiling phenomena at the microscale.
- For the initially analyzed case of a single microchannel, it was found that such modeling approach was capable of predicting the trends from flow boiling correlations, by also providing the capability of two-phase flow regime evolution and its tracking.
- For the case of more complex geometries, such as the case of pin fins, the VOF model presents the disadvantage of interfacial resolution limitation, causing the early separation of vapor structures and its distortion due to associated surface tension calculation issues.
- The prediction of two-phase flow regimes in microgaps with pin fins can be significantly improved by using the Coupled Level-Set Volume of Fluid (CLSVOF) technique, which has a continuous formulation across the interface and allows the representation of sharper liquid/vapor interfaces and therefore a more accurate surface tension calculation. Flow boiling simulations in a portion of the TDV using this approach indicated a good agreement with experimental visualizations of bubble nucleation and departure.

Upon completion of the aforementioned studies with their corresponding conclusions and acquired experience, the ultimate task of assessing both numerically and experimentally the two-phase flow cooling characteristics of the described TDVs was finally achieved. The saturated flow boiling operation with the dielectric fluid HFE7200 was assessed for different power conditions, with the following main findings:

- The two-phase cooling operation results in nearly-uniform wall superheats across the entire microgap TDV for a range of power conditions at a specified flow rate, therefore indicating the advantage of the latent heat of vaporization as the energy removal mechanism.
- The central hotspot heat flux can be significantly increased for conditions in which the local surface area has been enhanced; for the present cases it was augmented up to 5 times with respect the background heat flux conditions, with a temperature gradient of no larger than 10 °C when compared to other TDV zones.
- Similar to the conclusion for the TDV operation in single-phase conditions, it was found that for the two-phase cooling case the effect of flow bypass is also negligible and therefore does not justify further flow restrictions.
- The wall superheats fall in close proximity to a straight line for the hotspot to background heat flux ratios equal to a value of 2; such behavior confirms that the heat transfer coefficient remains nearly constant at the hotspot zone since both the heat transfer area and heat flux are doubled.

8.2.1 Technical contributions

One of the main contributions from the present dissertation is the experimental and numerical demonstration of flow boiling thermal management in a silicon microgap with variable pin fin clustering for addressing hotspots in a relevant mode for the vertical integration of ICs. Besides demonstrating such practical features with the comprehensive design of the TDV, the refined CFD-HT model for two-phase cooling analysis was finally compared with the non-trivial thermal-hydraulic behavior observed in the experiments, observing a remarkable capability for predicting such with a high level of detail. The temperature jumps at the hotspot area were closely predicted as well as the relatively uniform temperature across the background zones due to the two-phase mode of operation. On the hydraulic side, the model was capable to predict with excellent agreement both the initial saturation conditions for pressure drop (single phase), as well as evolving as a function of time until reaching a quasi-steady state equilibrium in which dynamic two-phase pressure closely matched the average experimental values and range of dynamic variation. The numerical modeling of such phenomena in these cases had remained relatively unexplored area due to a number challenges; therefore, the direct validation of this model constitutes a key advance for the detailed thermal design and optimization of complex microgap cooling layers for two-phase cooling systems.

8.3 Recommendations for future work

The findings and contributions from the present dissertation leave a number of possibilities for applying the proposed concepts and methodologies for different cases encountered in relevant applications of microelectronics thermal management. The following ideas are recommended:

- The described CFD-HT models in this dissertation can be used for further analysis under transient power inputs; heating pulses can be implemented either at the hotspot or background zones to provide insightful data regarding the dynamic response of the thermal and flow fields under such transitions. The capabilities and results from these models can significantly overcome experimental limitations to quantify such phenomena occurring in the time scale of micro-seconds. The two-phase flow regime prediction capabilities from the CLSVOF model can provide interesting behaviors in the flow boiling response to such conditions.

- The pin fin clustering analysis can be extended by using the proposed CFD-HT model and analyze a number of interesting variations, such as describing the limits at which the concept of locally increasing the pin fin density is overshadowed by the effect of flow bypass. For such interesting study, it is also recommended to take into account structural considerations for the pin fin diameter lower limits and also consider electrical aspects such as the required number of Through-Silicon-Vias (TSVs) and their diameter inside the pin fin; such practical aspects will set a constrain into the lower geometry limits and will help to better decide the geometric features for an optimized design.

APPENDIX A. SAMPLE CODE OF THE PHASE-CHANGE MODEL FUNCTIONS

```
#include "udf.h"
#include "sg_mphase.h"
#define T_SAT %Saturation temperature
#define LAT_HT %Latent heat of vaporization
#define SIGMA_E %Accommodation coefficient
#define M_w %Molecular weight
#define R_u %Universal gas constant
#define d %Interfacial parameter
#define RHO_v %Vapor density
#define RHO_l %Liquid density
#define PI 3.1416

DEFINE_SOURCE(liq_src, cell, pri_th, dS, eqn)
{

  Thread *mix_th, *sec_th;
  real m_dot_l;
  RF= (6/d)*((2*SIGMA_E)/(2-
SIGMA_E))*(M/(2*PI*R_u*T_SAT))^0.5*LAT_HT*(RHO_v/(RHO_l-
RHO_v));

  mix_th = THREAD_SUPER_THREAD(pri_th);
  sec_th = THREAD_SUB_THREAD(mix_th, 1);

  if(C_T(cell, mix_th)>=T_SAT){
    m_dot_l = -RF*C_VOF(cell, pri_th)*C_R(cell, pri_th)*
                fabs(C_T(cell, pri_th) - T_SAT)/T_SAT;
    dS[eqn] = -RF*C_R(cell, pri_th)*
      fabs(C_T(cell, pri_th) - T_SAT)/T_SAT;
                             }
  else {
    m_dot_l = RF*C_VOF(cell, sec_th)*C_R(cell, sec_th)*
                fabs(T_SAT-C_T(cell,mix_th))/T_SAT;

    dS[eqn] = RF*C_VOF(cell, sec_th)*
                fabs(T_SAT-C_T(cell,mix_th))/T_SAT;

       }

  return m_dot_l;
```

```
}

DEFINE_SOURCE(vap_src, cell, sec_th, dS, eqn)

{

  Thread * mix_th, *pri_th;
  real m_dot_v;
  RF=                                  (6/d)*((2*SIGMA_E)/(2-
SIGMA_E))*(M/(2*PI*R_u*T_SAT))^0.5*LAT_HT*(RHO_L/(RHO_l-
RHO_v));
  mix_th = THREAD_SUPER_THREAD(sec_th);
  pri_th = THREAD_SUB_THREAD(mix_th, 0);

  if(C_T(cell, mix_th)>=T_SAT){
    m_dot_v = RF*C_VOF(cell, pri_th)*C_R(cell, pri_th)*
                fabs(C_T(cell, mix_th) - T_SAT)/T_SAT;

    dS[eqn] = RF*C_VOF(cell, pri_th)*
                fabs(C_T(cell, mix_th) - T_SAT)/T_SAT;
                               }
  else {
    m_dot_v = -RF*C_VOF(cell, sec_th)*C_R(cell, sec_th)*
                fabs(T_SAT-C_T(cell,mix_th))/T_SAT;

    dS[eqn] = -RF*C_R(cell, sec_th)*
      fabs(C_T(cell, sec_th) - T_SAT)/T_SAT;

       }

  return m_dot_v;

}

DEFINE_SOURCE(enrg_src, cell, mix_th, dS, eqn)
{
  Thread *pri_th, *sec_th;
  real m_dot;
RF=                                    (6/d)*((2*SIGMA_E)/(2-
SIGMA_E))*(M/(2*PI*R_u*T_SAT))^0.5*LAT_HT*(RHO_L/(RHO_l-
RHO_v));
  pri_th = THREAD_SUB_THREAD(mix_th, 0);
  sec_th = THREAD_SUB_THREAD(mix_th, 1);

  if(C_T(cell, mix_th)>=T_SAT){
    m_dot = -RF*C_VOF(cell, pri_th)*C_R(cell, pri_th)*
                fabs(C_T(cell, pri_th) - T_SAT)/T_SAT;
```

```
    dS[eqn]    =         -RF*C_VOF(cell,    pri_th)*C_R(cell,
pri_th)/T_SAT;
                               }

  return LAT_HT*m_dot;
}
```

APPENDIX B. ACTIVATION OF VAPOR NUCLEATION

As it was discussed in multiple points of this work, the bubble nucleation for such modeling approach occurs at computational cells on the heated wall when the temperature criterion for vaporization given in Table 5.1 is satisfied.

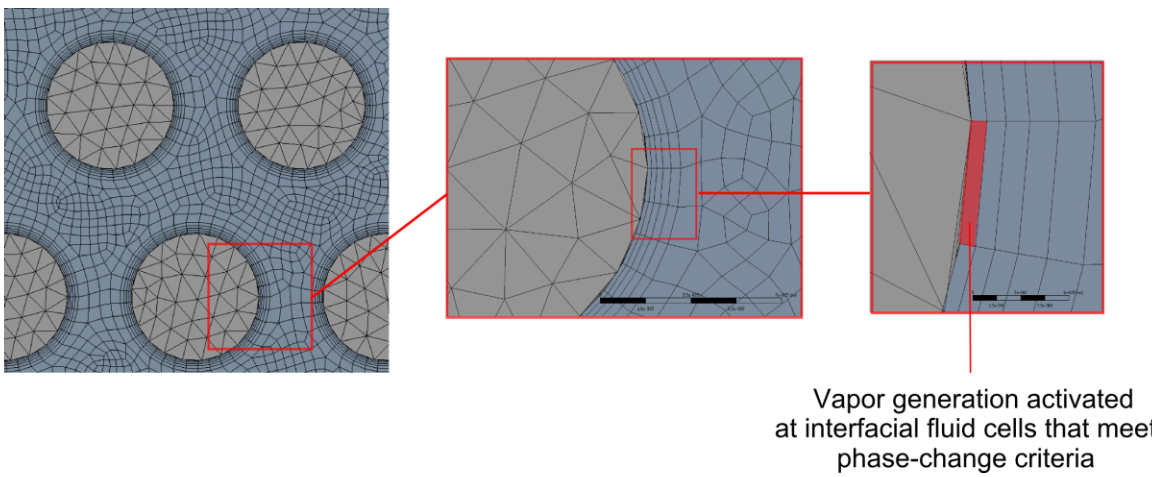

Figure B.1. Vapor nucleation starts at the interfacial fluid cells that meet the phase change criteria given in Table 5.1.

Although the real process involves bubble nucleation at wall crevices with entrapped vapor, it’s important to realize that such effects cannot be captured through a CFD based-model considering the large number of features in the computational domain and multiple scales involved. However, it has been observed that such approach is reasonable and comparable to the experimental bubble nucleation processes reported in the literature for similar configurations and refrigerants, as proven by the different validation evidence provided when comparing with corresponding experimental data.

REFERENCES

[1] G.E. Moore, Cramming more components onto integrated circuits, *Electronics*, 38 (8), 1965, p. 114.

[2] D. James, Shrinking chips is hard - Intel forced to delay their 10nm Cannon Lake CPUs again, PCGamesN. Retrieved on Sep 2017 from: https://www.pcgamesn.com/intel-cannon-lake-release-date

[3] A. Eassa, Intel Corp. delays 10 nm chip production, The Motley Fool, LLC. Retrieved on May 2018 from: https://www.fool.com/investing/2018/04/29/intel-corp-delays-10nm-chip-production.aspx

[4] Z. Or-Bach, 28 nm was last node of Moore's law, *MonolithIC 3D*. Retrieved on May 2018 from: http://www.monolithic3d.com/blog/28nm-was-last-node-of-moores-law

[5] D.A. Muller, T. Sorsch, S. Moccio, F.H. Baumann, K. Evans-Lutterodt, G. Timp, The electronic structure at the atomic scale of ultrathin gate oxides, *Nature*, 399 (1999), p. 758-761.

[6] J.D. Meindl, Beyond Moore's law: the interconnect era, *Computing in Science and Engineering*, 5 (1), 2003, p. 20-24.

[7] F. Villa, Advanced direct contact heat pipes and liquid cooling systems for CPUs, *Cooling Tree Systems*. Retrieved on May 2018 from: https://www.coolingtreesystems.com/

[8] A. Bar-Cohen, J.J. Maurer, J.G. Felbinger, DARPA's Intra/Interchip Enhanced Cooling (ICECool) Program, in: *Proceedings of the CS MANTECH Conference*, New Orleans, Louisiana, USA, 2013, p. 171-174.

[9] D.B. Tuckerman, R. Pease, High-performance heat sinking for VLSI, *IEEE Electron Device Letters*, 2 (5), 1981, p. 126-129.

[10] Y. Peles, A. Kosar, C. Mishra, C.J. Kuo, B. Schneider, Forced convective heat transfer across a pin fin micro heat sink, *International Journal of Heat and Mass Transfer*, 48 (17), 2005, p. 3615-3627.

[11] A. Kosar, C. Mishra, Y. Peles, Laminar flow across a bank of low aspect ratio micro pin fins, *Journal of Fluids Engineering, Transactions of the ASME*, 127 (3), 2005, p. 419-430.

[12] A. Kosar, Y. Peles, Thermal-hydraulic performance of MEMS-based pin fin heat sink, *ASME Journal of Heat Transfer*, 128 (2), 2006, p. 121-131.

[13] A. Kosar, Y. Peles, Micro scale pin fin heat sinks – parametric performance evaluation study, *IEEE Transaction on Components and Packing Technologies*, 30 (4), 2007, p. 855-865.

[14] E.G. Colgan, B. Furman, M. Gaynes, N. LaBianca, J. H. Magerlein, R. Polastre, et al., High performance and sub-ambient silicon microchannel cooling, *ASME Journal of Heat Transfer*, 129 (8), 2006, p. 1046–1051.

[15] E.G. Colgan, B. Furman, M. Gaynes, W.S. Graham, N. LaBianca, J.H. Magerlein, et al., A practical implementation of silicon microchannel coolers for high power chips, *IEEE Transactions on Components and Packaging Technologies*, 30 (2), 2007, p. 218–225.

[16] Y. Zhang, A. Dembla, Y. Joshi, M.S. Bakir, 3D Stacked microfluidic cooling for high-performance 3D ICs, in: *Proceedings of the 62nd IEEE ECTC Conference*, May 29-June 1, San Diego CA, 2012, p. 1644-1650.

[17] Y. Zhang, M.S. Bakir, Independent interlayer microfluidic cooling for heterogeneous 3D IC applications, *Electronics Letters*, 49 (6), 2013, p. 404-406.

[18] F. Alfieri, M.K. Tiwari, I. Zinovik, D. Poulikakos, T. Brunschwiler, B. Michel, 3D Integrated Water Cooling of a Composite Multilayer Stack of Chips, *ASME Journal of Heat Transfer*, 132(12), 2010, p. 121402.

[19] Z. Wan, Y. Joshi, Pressure drop and heat transfer characteristics of pin fin enhanced microgaps in single phase microfluidic cooling, *International Journal of Heat and Mass Transfer*, 115 (A), 2017, p. 115-126.

[20] C.A. Rubio-Jimenez, S.G. Kandlikar, A. Hernandez-Guerrero, Numerical analysis of novel micro pin fin heat sink with variable fin density, *IEEE Transactions on Components, Packaging and Manufacturing Technology*, 2 (5), 2012, p. 825-833.

[21] D. Lorenzini-Gutierrez, S.G. Kandlikar, Variable fin density flow channels for effective cooling and mitigation of temperature non-uniformity in three-dimensional integrated circuits, *ASME Journal of Electronic Packaging*, 136 (2), 2014, p. 021007.

[22] C. Green, A.G. Fedorov, Y.K. Joshi, Fluid-to-fluid spot-to-spreader (F2/S2) hybrid heat sink for integrated chip-level and hot spot-level thermal management, *ASME Journal of Electronic Packaging*, 131, 2009, p. 025002.

[23] C.S. Sharma, M.K. Tiwari, S. Zimmermann, T. Brunschwiler, G. Schlottig, B. Michel, D. Poulikakos, Energy efficient hotspot-targeted embedded liquid cooling of electronics, *Applied Energy*, 138, 2015, p. 414-422.

[24] Z. Wan, H. Xiao, Y.K. Joshi, S. Yalamanchilli, Co-design of multicore architectures and microfluidic cooling for 3D stacked ICs", *Microelectronics Journal*, 45, 2014, p. 1814-1821.

[25] S.V. Garimella, C.B. Sobhan , Transport in microchannels - a critical review, *Annual Reviews in Heat Transfer*, 13, 2003, p. 1-50.

[26] J.R. Thome, Boiling in Microchannels, *International Journal of Heat and Fluid Flow*, 255, 2004, p. 128-39.

[27] S.S. Bertsch, E.A. Groll, S.V. Garimella, Review and comparative analysis of studies on saturated flow boiling in small channels, *Nanoscale and Microscale Thermophysical Engineering*, 12, 2008, p. 187-227.

[28] S.M. Ghiaasiaan, Two-phase flow, boiling and condensation: in conventional and miniature systems, 2008, Cambridge University Press, New York.

[29] S.G. Kandlikar, Scale effects on flow boiling heat transfer in microchannels: a fundamental perspective, *International Journal of Thermal Sciences*, 49, 2010, p. 1073-1085.

[30] S. Khrishnamurthy, Y. Peles, Flow boiling of water in a circular staggered micro-pin fin heat sink, *International Journal of Heat and Mass Transfer*, 51, 2008, p. 1349-1364.

[31] J.-M. Koo, S. Im, L. Jiang, K. E. Goodson , Integrated microchannel cooling for three-dimensional electronic circuit architectures, *ASME Journal of Heat Transfer*, 127, 2005, p. 49–58.

[32] J.-M Kim, Y.K. Joshi, A.G. Fedorov, Y.-J. Lee, S.-K. Lim, Thermal characterization of interlayer microfluidic cooling of three-dimensional integrated circuits with non-uniform heat flux, *ASME Journal of Heat Transfer*, 132, 2010, p. 041009.

[33] X. Han, A. Fedorov, Y. Joshi, Flow boiling in microgaps for thermal management of high heat flux microsystems, *ASME Journal of Electronic Packaging*, 138 (4), 2016, p. 040801.

[34] P. Asrar, X. Zhang, C.E. Green, M. Bakir, Y. Joshi, Flow boiling of R245fa in a microgap with integrated staggered circular cylindrical pin fins, *International Journal of Heat and Mass Transfer*, 121, 2018, p. 329-342.

[35] H.L. Wu, X.F. Peng, P. Ye, Y.E. Gong, Simulation of refrigerant flow boiling in serpentine tubes, *International Journal of Heat and Mass Transfer*, 50, 2007, p. 1186-1195.

[36] Z. Yang, X.F. Peng, P. Ye, Numerical and experimental investigations of two-phase flow during boiling in a coiled tube, *International Journal of Heat and Mass Transfer*, 51, 2008, p. 1003-16.

[37] W.H. Lee, A pressure iteration scheme for two-phase flow modelling, in: *Multiphase Transport Fundamentals, Reactor Safety Applications*, T.M. Verizoglu, 1980, Hemisphere Publishing, Washington, DC.

[38] S.C.K. De Schepper, G.J. Heyderickx, G.B. Marin, Modeling of the evaporation of a hydrocarbon feedstock in the convection section of a steam cracker, *Computers and Chemical Engineering*, 33, 2009, p. 122-132.

[39] C. Fang, D. Milnes, A. Rogacs, K.Goodson, Volume of fluid simulation of boiling two-phase flow in a vapor-venting microchannel, *Frontiers in Heat and Mass Transfer*, 1, 2010, p. 013002.

[40] R. Zhuan, W. Wang, Simulation of subcooled flow boiling in a micro-channel, *International Journal of Refrigeration*, 34, 2011, p. 781-795.

[41] M.S. Plesset, S.A. Zwick, The growth of vapour bubble in superheated liquid, *Journal of Applied Physics*, 25, 1954, p. 493-500.

[42] M. Magnini, J.R. Thome, Computational study of saturated flow boiling within a microchannel in the slug flow regime, *ASME Journal of Heat Transfer*, 138 (2), 2015, p. 021502.

[43] C. Green, P. Kottke, X. Han, et al., A review of two-phase forced cooling in three-dimensional stacked electronics: technology integration, *ASME Journal of Electronic Packaging*, 137, 2015, p. 040802.

[44] D. C. Woodrum, X. Zhang, P.A. Kottke, Y.K. Joshi, A.G. Fedorov, M.S. Bakir, S.K. Sitaraman, Reliability assessment of hydrofoil-shaped micro-pin fins, *Proceedings of the Intersociety Conference on Thermal and Thermomechanical Phenomena in Electronic Systems (ITHERM)*, May-June 2016, Las Vegas, NV, USA.

[45] S.J. Kline, F.A. McClintock, Describing uncertainties in single-sample experiments, *Mechanical Engineering*, 75 (1), 1953, p. 3-9.

[46] T. Al-Shemmeri, Engineering Fluid Mechanics, 2012, Ventus Publising ApS, London, United Kingdom.

[47] Engineering Equation Solver (EES®), Academic Professional Version 9.911.

[48] C.W. Hirt, B.D. Nichols, Volume of fluid (VOF) method for the dynamics of free boundaries, *Journal of Computational Physics*, 39, 1981, p. 201-225.

[49] J.U. Brackbill, D.B. Kothe, C. Zemach, A continuum method for modeling surface tension, *Journal of Computational Physics*, 100, 1992, p. 335-354.

[50] D.L. Youngs, Time-dependent multi-material flow with large fluid distortion. In: *Numerical Methods for Fluid Dynamics*. K.W. Morton and M.J. Baines editors, Academic Press, 1982, p. 273–85.

[51] O. Ubbink, Numerical prediction of two fluid systems with sharp interfaces, PhD Thesis, Imperial College of Science, Technology and Medicine, London, England, 1997.

[52] J.R. Maa, Evaporation coefficient of liquids, *Industrial & Engineering Chemistry Fundamentals*, 6, 1967, p. 504–18.

[53] H.K. Cammenga, F.W. Schulze, W. Theuerl, Vapor pressure and evaporation coefficient of water, *Journal of Chemical Engineering Data*, 22, 1977, p. 131–34.

[54] M. Healy, S.K. Lim, A study of stacking limit and scaling in 3D ICs: An Interconnect Perspective, *Proceedings of the IEEE Electronic Components and Technology Conference*, 2009, p. 1213–1220.

[55] C.J. Glassbrenner, G.A. Slack, Thermal conductivity of silicon and germanium from 3 K to the melting point, *Physical Review*, 134 (4A), 1964, p. A1058-1059.

[56] J.C. Chen, Correlation for boiling heat transfer to saturated fluids in convective flow, *Industrial & Engineering Chemistry Research*, 5, 1966, p. 322–329.

[57] H. Muller-Steinhagen, K. Heck, 1986, A simple friction pressure drop correlation for two-phase flow in pipes, *Chemical Engineering Progress*, 20, 1986, p. 297-308.

[58] C. Choi, J.S. Shin, D.I. Yu, M.H. Kim, Flow boiling behaviors in hydrophilic and hydrophobic microchannels, *Experimental Thermal and Fluid Science*, 35, 2011, p. 816–24.

[59] W. Aniszewski, T. Menard, M. Marek, Volume of fluid (VOF) type advection methods in two-phase flow: a comparative study, *Computers & Fluids*, 97, 2014, p. 52-73.

[60] H. Hua, J. Shin, J. Kim, Level-set, Phase-field, and immersed boundary methods for two-phase fluid flows, *Journal of Fluids Engineering*, 136, 2014, p. 0210301.

[61] M. Sussman, and E.G. Puckett, A coupled level let and volume-of-fluid method for computing 3D and axisymmetric incompressible two-phase flows, *Journal of Computational Physics*, 162 (2), 2000, p. 301-337.

[62] ANSYS® FLUENT® Theory Guide. Release 14.0. November 2011.

[63] S.A. Isaacs, Two-Phase Flow and Heat Transfer in Pin-Fin Enhanced Microgaps, MS Thesis, Georgia Institute of Technology, 2013.